technische universität
dortmund

Dissertation

Magneto-Optical Intensity Effects in Hybrid Plasmonic Structures

submitted in partial fulfillment of the
requirements for the degree of

Dr. rer. nat.

to the Faculty of Physics at the
TU Dortmund University, Germany

by

Felix Spitzer

Dortmund, February 2019

Accepted by the Faculty of Physics of the TU Dortmund University, Germany.

Day of the oral examination: 1st February 2019

Examination board:
PD. Dr. Ilya A. Akimov
Prof. Dr. Manfred Bayer
Dr. Alexander N. Poddubny
Prof. Dr. Heinrich Päs
Dr. Bärbel Siegmann

Contents

I Introduction **1**

1 Motivation and Outline **2**

II Literature Review **6**

2 Electrodynamics **7**
2.1 Maxwell's Equations 7
2.2 Free Electron Model 9
2.3 Drude-Lorentz Model 10
2.4 Comparison with Empirical Values for Gold 11

3 Surface Plasmon Polaritons **14**
3.1 Fresnel Equations 15
3.2 Polarization of Surface Bound Waves 15
3.3 Excitation of Surface Plasmon Polaritons 21
3.4 Wood's Anomaly 23

4 Magneto-Optical Effects **25**
4.1 Giant Excitonic Zeeman Effect in (Cd,Mn)Te 25
4.1.1 Faraday Geometry 26
4.1.2 Voigt Geometry 29
4.2 Magneto-Optical Kerr effect 31
4.3 Gyrotropic Permittivity 32
4.4 Enhanced Magneto-Optical Effects in Plasmonic Crystals 34

5 Transverse Spin Angular Momentum of Evanescent Surface Waves **37**
5.1 Spin-Momentum Locking at the Metal-Dielectric Interface 37
5.2 Transverse Spin of Surface Plasmon Polaritons 41
5.3 Establishing the Dipole Emission 42
5.4 Scattering Matrix Method 43

III Experimental Methods **44**

6 Material Properties of the (Cd,Mn)Te / (Cd,Mg)Te Samples **45**

7 Experimental Setups **50**
7.1 Magneto-Photoluminescence Setup for the Determination of the Mn^{2+} Concentration 50
7.2 Fixed Angle and High Magnetic Field Setup 51
7.3 Angular Resolved Optical Spectroscopy Setup 54

IV Results **62**

8 Transverse Magnetic Routing of Light Emission **63**
8.1 Value of Magnetization – Giant Zeeman Effect 63
8.2 Near-Field Effect 66
8.2.1 Sign of TMRLE for Photonic and Plasmonic Spin Fluxes . . 67
8.2.2 Directionality of Emission 69
8.2.3 Polarization Dependence 70
8.2.4 Angle Resolved TMRLE 72
8.2.5 Optimization of the Grating Period 74
8.3 Far-Field Effects 78
8.3.1 Analytical Solution of the Far-Field Routing of Light in a Structure with Finite Buffer Thickness 78
8.3.2 Interference Effect on Unstructured Sample 80
8.3.3 Diffraction Effect on Patterned Sample 81
8.4 Dependence on Magnetic Field Strength 84
8.5 Excitation-Laser Intensity Dependence 86
8.6 Temperature Dependence 87
8.7 Emission from the Non-Magnetic Layers 88
8.8 Summary of the Three Different Effects for Routing Emission 88

9 Transverse Magneto-Optical Kerr Effect at Narrow Optical Resonances **90**
9.1 TMOKE Spectrum of a Single Resonance 90
9.1.1 Weak Coupling Regime 93
9.1.2 Strong Coupling Regime 94
9.1.3 Comparison of Weak and Strong Coupling Regime 95
9.2 Angular Resolved TMOKE Spectra at the Excitonic Resonances . . 96
9.2.1 Weak Coupling Regime 96
9.2.2 Influence of the Cap Layer Thickness 100
9.2.3 TMOKE and Evanescent Optical Fields 101

9.2.4 Strong Coupling Regime 102
9.3 Summary of TMOKE in Weak and Strong Coupling Regime 104

10 Conclusions **106**

V Appendix **110**

Acknowledgements **111**

List of Publications **113**

Conference Contributions **114**

Acronyms **116**

Bibliography **118**

Part I

Introduction

Chapter 1

Motivation and Outline

Ever since in 1845 "magnetic force and light were proved to have relation to each other" [Far99, p. 123] by Michael Faraday, the research on *magneto-optical effects* continues to evolve. Faraday came to his conclusion as he noticed a rotation of the polarization of light, when it was transmitted through magnetized glass [Far46]. This is nowadays known as the Faraday effect. Several decades later Kerr [Ker77] was able to observe the rotation of the polarization of light also in reflection, known as the polar magneto-optical Kerr effect (PMOKE). However, not all of the magneto-optical effects influence the polarization of light. Instead there is also the class of intensity effects that solely changes the intensity of the light. When light is reflected from a medium that is magnetized perpendicular to the plane of light incidence, the intensity of the reflected light changes. This effect is known as the transverse magneto-optical Kerr effect (TMOKE) and it was Zeeman [Zee96] who discovered the TMOKE in 1896, half a century after the first findings of Faraday. We will further discuss these magneto-optical effects in Chapter 4.

At about the same time also the optical spectroscopy evolved due to a major breakthrough in this field. Instead of prisms now metallic gratings allowed for a more precise spectral dispersion of light. In the early 20th century Wood [Woo02] noticed narrow bright and dark lines in the intensity spectrum of a continuous light source diffracted by a metallic grating. These lines named Wood's anomaly have fascinated the science community for many decades. In a first explanation, Rayleigh [Ray07] considered these anomalies as the result of diffraction into the grating surface plane. While this interpretation was not questioned for a couple of decades [May12, p. 5], measurements in 1936 by Strong [Str36] showed a dependence of the spectral position of these lines on the type of metal used. As the grating period remained unchanged, these experiments led to a reappraisal of this first interpretation. Fano [Fan41] could partly resolve this discrepancy as he was able to distinguish two types of resonance lines. He observed a sharp line that was well described by grating diffraction. Apart from that he noticed a second diffuse resonance at lower energy, consisting of a minimum and a maximum in intensity, and correctly attributed this resonance to

waves propagating along the grating surface. The surface waves observed here are nowadays called surface plasmon polariton (SPP) and are accompanied by charge density oscillations in the metal. The observation of the Wood's anomaly and in particular the Fano resonance can thus be considered the starting point of the research field of *plasmonics*. An extensive introduction to the field of plasmonics and the related optical properties of metals will be given in Chapter 2 and 3.

While common electromagnetic waves are subject to the Abbe diffraction limit, in plasmonics a sub-wavelength concentration of the electromagnetic field may be easily achieved [Gra10]. This is a result of their evanescent, surface bound nature that also leads to an increased sensitivity to changes of the optical properties in this region. In gold nano-particles (NPs) for example strongly enhanced field intensities at their interface are observed [Ame17]. This local enhancement of the field intensity is attractive for non-linear optical processes like second harmonic generation (SHG) [Kau12; Hen16] and surface-enhanced Raman scattering (SERS) allowing the detection down to the level of single molecules [Jah16; Sch14]. Unknowingly of the physical background the localized surface plasmons (LSPs) present in gold NPs were already utilized in ancient times (around the 4th century) as their spectral position affects the colour of stained glass [Wag00]. The plasmonic resonances are sensitive not only to the intrinsic properties of the gold film or NP, but also to their environment and thus are frequently used for sensing in biomedical and chemical applications [Ank08; Sah12; Fab16]. More sophisticated chiral plasmonic systems, like a micrometer sized metal helix (basically a tiny corkscrew) can act as a circular polarizer [Gan09] and might even allow to detect the chirality of chemical analytes [Hen17]. These are just some examples that illustrate the rich field of applications for plasmonic nanostructures.

Another intriguing direction in the field of plasmonics is related to the rapidly increasing demand for digital information transport and processing. While the transition from wired to photonic information transport based on optical fibres currently takes place, this evolution from electronics to photonics has not yet fully reached the microchip industry. As a consequence of the downscaling of electronic circuits with transistor densities of about $100/\mu m^2$ [Cou17] the problem of transporting the increasing amount of information arises [Ozb06]. Due to the fundamental diffraction limit of light, this challenge cannot simply be overcome by optical interconnects such as fibres that could carry a considerably larger amount of digital information. With plasmonic circuits on the other hand electric currents and optical signals could potentially be combined on the same chip [Ozb06; Sch10], although one should note that due to the inevitable loss in plasmonic structures [Khu15] the propagation length of the SPP wave is limited [Bar03]. In contrast to an electromagnetic wave propagating in a continuous medium, the evanescent character of these SPP waves endows them with a longitudinal component of the electric field [Aie15]. Within the propagation plane (i.e. with the normal of this plane being perpendicular to

the propagation direction) the wave thus possesses a circular polarization that is locked to the propagation direction, as identified by Bliokh and Nori [Bli12]. This circular polarization can be described as a transverse spin angular momentum (SAM), which is present in evanescent waves (plasmonic systems [Bli12], waveguides [Pet14] and whispering-gallery-mode resonators [Jun13]) and highly focused beams [Ban13]. Notably, the transverse SAM is locked to the propagation direction of an SPP wave which is called spin-momentum locking. The transverse SAM is promising for optical circuitry as it allows spin-sensitive addressing and reading of guided modes and quantum states [Aie15]. A more detailed introduction to the field of transverse SAM is presented in Chapter 5.

In many domains of modern optics the control of light reflection, emission and its propagation direction is required, ranging from macroscopic searchlights to nanoscopic antennas [Ben11; Lod17]. Control over the propagation direction established by the use of magnetic forces is highly appealing for applications in magneto-optical storage, nanophotonic circuits and precision metrology [Tem10; Aki12; Arm13; Bos16]. Magneto-optical phenomena such as the Faraday and Kerr effect allow to control the polarization of transmitted and reflected light rays respectively [Zve97; Ino13]. The necessary enhancement of these magneto-optical effects began already in the late 1980s with studies on smooth ferromagnetic films [Bur86; Hic87], establishing the research field of *magneto-plasmonics*. The emerging nanostructuring methods allowed for a patterning of the metal films and gradually led to more complex magneto-plasmonic systems. In these so-called plasmonic crystals (PCs) plasmonic and magneto-optical effects are combined in a single structure, consisting of a magnetic layer with a periodically perforated gold film. The combination of magneto-optical effects with the field of plasmonics is highly attractive as the localized fields result in an enhanced sensitivity to changes of the optical properties, potentially allowing novel devices in miniaturized photonic circuits [Bel13]. In this respect a TMOKE enhancement of at least one order of magnitude was demonstrated near the SPP resonance in a bismuth iron garnet (BIG) PC in transmission [Bel11]. In a structure with increased bismuth substitution level the TMOKE strength was enhanced by nearly another order of magnitude [Poh13]. Also the Faraday rotation is enhanced in thin-film PCs by one order of magnitude, due to the interplay of SPPs and photonic waveguide modes in such a system [Chi13; Flo17]. Similarly the enhancement of TMOKE was observed experimentally by Kreilkamp et al. [Kre13] in gold nanowires placed on top of a photonic waveguide. In order to achieve magnetic field control over the directionality in emission a dedicated tailoring of the structures is required. So far this has only been demonstrated in Faraday geometry for the emission of chiral objects, where directionality is established along the axis parallel to the magnetic field [Rik97]. In the transverse geometry where directionality is established perpendicular to the magnetic field, no intensity effects have been reported yet.

This thesis contributes to the field of magneto-optical effects in two ways. First, in Chapter 8 of this thesis we will address the following question:

If an emitter is polarized by a magnetic field such that it possesses a transverse SAM, will its emission become directional as a consequence of the spin-momentum locking at the interface?

This effect is studied in a structure comprising a (Cd,Mn)Te diluted magnetic semiconductor (DMS) quantum well (QW) buried below (Cd,Mg)Te as the surrounding material. On top of the structure a plasmonic grating coupler is applied, which allows for the detection of surface modes in the far field. We study the exciton emission from the magnetic QW, which shows a giant Zeeman splitting within magnetic field. In a transverse magnetic field the emission thus possesses non-zero transverse SAM. When the emitter is close to the interface the emission might decay into the evanescent surface waves, for which spin and momentum are locked and we thus might observe directional emission. While highly desirable for the control of emission on the nanoscale, a similar effect in transverse magnetic field was not yet reported irrespective of the system presented in this thesis.

The giant Zeeman splitting in combination with the narrow exciton linewidth as compared to other resonances like the SPP immediately suggests a second question:

How does the TMOKE spectrum change, when the Zeeman splitting overcomes the resonance linewidth?

We will discuss this question in Chapter 9 for the TMOKE observed at the QW exciton resonance in (Cd,Mn)Te / (Cd,Mg)Te DMS structures. So far in the literature only TMOKE studies were reported where the splitting was smaller than the resonance linewidth. Measurements in the contrary case would thus establish a whole new TMOKE regime.

Part II

Literature Review

Chapter 2

Electrodynamics

In this section we will discuss the characteristic optical properties of metals, which are of major importance for the excitation of surface bound waves, discussed in Chapter 3. Therefore we will begin with a short review of Maxwell's equations describing the properties of electromagnetic waves in matter. Next we will describe the electron dynamics of an idealized metal in the free electron and Drude-Lorentz model over a wide frequency range in order to obtain the electromagnetic response of the metal. We will close this chapter with a comparison of these results with the real properties of gold. This chapter is based on the well-structured introduction to the physics of surface plasmon polaritons presented in Reference [Mai07, Ch. 1].

2.1 Maxwell's Equations

Maxwell's equations describe how electromagnetic fields interact and depend on each other in classical theory, both inside the volume of a material and at its interfaces. Interestingly even metallic nanostructures may be described by these equations due to the high free carrier density. The description is thus still valid even without quantum mechanical considerations, as long as the quantum confinement remains negligible. In particular this is the case due to the smaller electron energy level spacing as compared to the energy of thermal excitations $k_{\mathrm{B}}T$, especially at elevated temperatures (i.e. at room temperature). The four Maxwell's equations

$$\nabla \times \boldsymbol{E} = -\frac{\partial \boldsymbol{B}}{\partial t}, \tag{2.1a}$$

$$\nabla \times \boldsymbol{H} = \boldsymbol{j}_{\mathrm{ext}} + \frac{\partial \boldsymbol{D}}{\partial t}, \tag{2.1b}$$

$$\nabla \cdot \boldsymbol{D} = \rho_{\mathrm{ext}} \quad \text{and} \tag{2.1c}$$

$$\nabla \cdot \boldsymbol{B} = 0 \tag{2.1d}$$

will be the starting point of the following discussion. [Mai07, pp. 5-6]

Eq. (2.1a) is also known as Faraday's law and Eq. (2.1c) as Gauss's law. The macroscopic fields $\boldsymbol{E}, \boldsymbol{H}, \boldsymbol{D}$ and $\boldsymbol{B}$ are known as electric field, magnetic field strength, dielectric displacement and magnetic flux density respectively. Additionally the external charge density ρ_{ext} and external current density $\boldsymbol{j}_{\text{ext}}$ are introduced. In general the term *magnetic field* is synonymously used for the magnetic flux density $\boldsymbol{B}$ and will be used in this manner if not stated otherwise.

The distinction of the total densities between internal $\rho = \rho_{\text{tot}} - \rho_{\text{ext}}$, $\boldsymbol{j} = \boldsymbol{j}_{\text{tot}} - \boldsymbol{j}_{\text{ext}}$ and external ones is advisable as only the latter set controls the system, while the prior set is only responding to these external stimuli. The polarization density $\boldsymbol{P}$ and magnetization $\boldsymbol{M}$ reveal another relation

$$\boldsymbol{D} = \varepsilon_0 \boldsymbol{E} + \boldsymbol{P} = \varepsilon_0 \boldsymbol{\varepsilon} \boldsymbol{E} \quad \text{and} \tag{2.2a}$$

$$\boldsymbol{H} = \frac{1}{\mu_0} \boldsymbol{B} - \boldsymbol{M} = \frac{\boldsymbol{\mu}^{-1}}{\mu_0} \boldsymbol{B} \tag{2.2b}$$

of the four macroscopic fields introduced before. [Mar10, pp. 613-614]

Here $\mu_0 = 4 \times 10^{-7}\,\mathrm{N/A^2}$ is defined as the vacuum permeability and $\varepsilon_0 = 1/\mu_0 c^2$ is the deduced vacuum permittivity [Gri14, p. 596]. While $\boldsymbol{P}$ is a macroscopic quantity, describing the electric dipole moment per unit volume, it appears due to the microscopic dipoles inside the material aligning with the electric field $\boldsymbol{E}$ [Mai07, p. 7]. In the case of linear media ($\boldsymbol{P} \propto \boldsymbol{E}$) a relative permittivity ε and permeability μ may be introduced describing the influence of the polarization density and magnetization in this set of equations. In this most universal case the relative permittivity and permeability are complex-valued 2nd-order tensors of the form

$$\boldsymbol{\varepsilon} = \begin{pmatrix} \varepsilon_{xx} & \varepsilon_{xy} & \varepsilon_{xz} \\ \varepsilon_{yx} & \varepsilon_{yy} & \varepsilon_{yz} \\ \varepsilon_{zx} & \varepsilon_{zy} & \varepsilon_{zz} \end{pmatrix} \qquad \text{and} \qquad \boldsymbol{\mu} = \begin{pmatrix} \mu_{xx} & \mu_{xy} & \mu_{xz} \\ \mu_{yx} & \mu_{yy} & \mu_{yz} \\ \mu_{zx} & \mu_{zy} & \mu_{zz} \end{pmatrix}.$$

For now we will limit ourselves to non-magnetic matter where $\boldsymbol{\mu} = \mathbb{1}, \boldsymbol{M} = \mathbb{0}$ and focus on the dielectric permittivity tensor $\boldsymbol{\varepsilon}$ only. Studies involving the magnetization will be discussed later on in Chapter 4. Furthermore we will consider only homogeneous ($\boldsymbol{\varepsilon}(\boldsymbol{r}) = \boldsymbol{\varepsilon}$) and isotropic ($\boldsymbol{\varepsilon} = \mathbb{1}\varepsilon$) matter for the time being, which simplifies the equations presented in (2.2).

Another notation of the complex-valued relative permittivity is given by $\varepsilon = \varepsilon_1 + \mathrm{i}\varepsilon_2$. Here the real and imaginary parts are separated, as they represent different optical properties. The following equations show the close connection of the relative

permittivity and other optical properties, namely the refractive index n and absorption κ, valid for non-magnetic media:

$$\begin{aligned} &\sqrt{\varepsilon} \equiv n + \mathrm{i}\kappa \\ \Leftrightarrow\ & n^2 = \frac{1}{2}\left(\sqrt{\varepsilon_1^2 + \varepsilon_2^2} + \varepsilon_1\right), \quad \kappa^2 = \frac{1}{2}\left(\sqrt{\varepsilon_1^2 + \varepsilon_2^2} - \varepsilon_1\right). \end{aligned} \tag{2.3}$$

Although not explicitly stated so far, the relative permittivity $\varepsilon(\omega)$ may strongly change depending on the angular frequency ω of the electromagnetic wave passing the medium. This is caused by optical resonances of various kinds such as the exciton resonance that will be discussed later on. Close to the allowed optical transitions in the studied material the relative permittivity is altered, resulting in a change of the refractive index $n(\omega)$ and the absorption $\kappa(\omega)$ One possibility to determine the dependence of the relative permittivity on the angular frequency in the range of optical frequencies are reflectivity studies, for example ellipsometry.

2.2 Free Electron Model

The discovery of the electron in 1897 had a major impact on the understanding of the structure of matter and soon led to the question of the underlying mechanism of conduction in metals. Only three years later in 1900 the Drude theory was the first one describing electric and heat conduction in metals. This model is in principle the application of the kinetic gas theory on metals, in which the electrons are considered as an electron gas. Even though the model already allowed the explanation of some effects like the ordinary Hall effect, it failed in other aspects. [Ash13, pp. 2-3]

In 1927 Sommerfeld introduced quantum mechanical aspects and combined them with the classical Drude model, which then covers a greatly extended number of experimental phenomena of which many are related to the thermal conductivity. The model Sommerfeld developed is mainly referred to as the free electron model (FEM) and is based on the following four approximations: The first two are about the interaction of electrons with other particles. The electron-electron interactions are neglected (Independent electron approximation) and electrons also do not interact with the ions, except for boundary conditions in some special cases not considered here (Free electron approximation). Thus the electrons are considered to move in a straight line in the absence of electromagnetic fields. Third, the motion of electrons is interrupted when scattered in instantaneous collisions with the average time in between called relaxation time τ, which is independent of velocity and space (Relaxation time approximation). And lastly the electronic system is described by the Fermi-Dirac statistics (Pauli exclusion principle). [Ash13, pp. 6-7, 38]

Taking into account these considerations one can deduce the simple equation of motion

$$m^*\ddot{\boldsymbol{x}} + m^*\gamma\dot{\boldsymbol{x}} = -e(\boldsymbol{E} + \dot{\boldsymbol{x}} \times \boldsymbol{B}), \tag{2.4}$$

with the collision frequency $\gamma = 1/\tau$ in the most general case of both external electric field $\boldsymbol{E}$ and magnetic field $\boldsymbol{B}$. As we consider the electrons like free electrons with an effective mass m^* and electric charge e, the equation of motion contains no restoring force. [Gru06, p. 197]

Assuming a harmonic time dependence of both the electric field and the electron oscillation with an ansatz $\propto e^{-\mathrm{i}\omega t}$ and by neglecting the external magnetic field contribution ($B = 0$) one receives a phase shift between the driving field and electron oscillation. Taking into account the influence of the electron displacement on the macroscopic polarization leads to the relation

$$\boldsymbol{P} = -en_e\boldsymbol{x} = -\frac{n_\mathrm{e}e^2}{m^*(\omega^2 + \mathrm{i}\gamma\omega)}\boldsymbol{E},$$

which in combination with Eq. (2.2a) yields the well known dielectric function of the free electron model

$$\varepsilon(\omega) = 1 - \frac{\omega_\mathrm{p}^2}{\omega^2 + \mathrm{i}\gamma\omega}. \tag{2.5}$$

Here $\omega_\mathrm{p} = \sqrt{n_\mathrm{e}e^2/(\varepsilon_0 m^*)}$ is the so called plasma frequency characterizing the bulk charge density waves with the free electron density n_e. [Mai07, pp. 11-12]

2.3 Drude-Lorentz Model

The free electron model is only applicable as a description of metals within narrow constraints, as for higher photon energies $E \gg \hbar\omega_\mathrm{p}$ the relative permittivity is approaching unity $\varepsilon \to 1$. In real metals this is not the case, as here the free *s*-electrons are dominating and form a highly polarized environment with the filled *d*-band located close to the Fermi surface. The entirety of all high-energy interband transitions can be incorporated in (2.5) by a constant positive background $\varepsilon_\mathrm{b} - 1$ in this energy range (usually $\varepsilon_\mathrm{b} \leq 10$) resulting in

$$\varepsilon(\omega) = \varepsilon_\mathrm{b} - \frac{\omega_\mathrm{p}^2}{\omega^2 + \mathrm{i}\gamma\omega}. \tag{2.6}$$

As shown in the next section this rather simple description already yields a good agreement at lower photon energies. [Mai07, pp. 13-14]

When approaching the visible spectral range, in the case of gold at an energy of about $E = \hbar\omega = 1.75\,\mathrm{eV}$ corresponding to a wavelength of about 700 nm, the free electron model begins to fail. At the boundary between visible and near-infrared the interband transitions of bound electrons begin to occur, thus leading to a rapid increase of the imaginary part ε_2 of the dielectric function. The dominant interband transition (2.4 eV for gold [Sun94]) can be described by the same approach used for direct transitions in semiconductors [Mar10, p. 698]. Photons above the band edge threshold are effectively inducing these interband transitions, where electrons from lower-lying d-bands are excited into the conduction band, resulting in increased damping and a competition with the excitation of surface plasmon polaritons introduced in Chapter 3. In first approximation the interband transitions can be described in the classical picture of a Lorentz oscillator, where in contrast to Eq. (2.4) the electron is bound with a resonance frequency ω_j resulting in the following slightly modified equation of motion

$$m_j^* \ddot{\boldsymbol{x}} + m_j^* \gamma_j \dot{\boldsymbol{x}} + m_j^* \omega_j^2 \boldsymbol{x} = -e\boldsymbol{E}. \tag{2.7}$$

Again, this equation is solved by a harmonic time dependence and in like manner one can calculate its influence on the relative permittivity, resulting in the following combined description in the Drude-Lorentz model with N oscillators

$$\varepsilon(\omega) = \varepsilon_\mathrm{b} - \frac{\omega_\mathrm{p}^2}{\omega^2 + \mathrm{i}\gamma\omega} - \sum_{j=0}^{N-1} \frac{\omega_{\mathrm{p},j}^2}{(\omega^2 - \omega_j^2) + \mathrm{i}\gamma_j\omega}. \tag{2.8}$$

While for $N = 0$ this equation is identical to the FEM, already a single additional oscillator of the Drude-Lorentz model (i.e. $N = 1$) considerably extends the model's scope up to the boundary of visible and ultra-violet light at around $E = 2.75\,\mathrm{eV}$. An accurate description of the full spectral range requires a larger number of Lorentz oscillators, which would lead to additional terms in the relative permittivity. [Mai07, pp. 17-18]

The oscillator amplitude $\omega_{\mathrm{p},0} = \sqrt{n_{e,0} e^2/(m_0^* \varepsilon_0)}$ of the first Lorentz oscillator appears in analogy to the plasma frequency of the free electron model ω_p. Although in this case $n_{e,0}$ is the density of bound electrons and m_0^* is their effective mass, with both of them generally being different from their free counterparts in a periodic potential. The damping constant γ_0 is mainly related to radiative damping in case of bound electrons. [Nov12, pp. 375-376]

2.4 Comparison with Empirical Values for Gold

Now that the theoretical dependence of the relative permittivity is known from Eq. (2.8) for an arbitrary number of oscillators, we want to compare the first two

approximations with the actual measured values for gold by Johnson and Christy [Joh72]. Figure 2.1 illustrates the real (ε_1) and imaginary part (ε_2) of the relative permittivity of gold, with the experimental data shown as black dots. The blue solid line represents the FEM description based on (2.8) with $N = 0$, which is fitted to the data resulting in the fit parameters presented in Table 2.1. This simple model already yields a satisfactory description of the data in the lower energetic Drude regime.

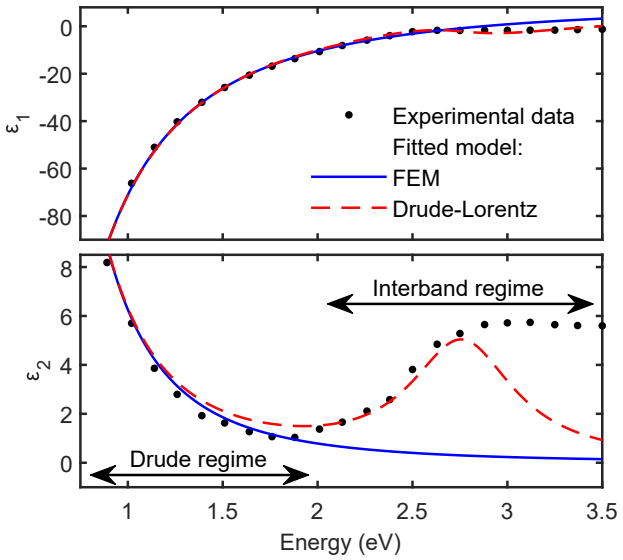

Figure 2.1: Real (ε_1) and imaginary part (ε_2) of the dielectric function of gold. The black dots show the experimental data by Johnson and Christy [Joh72], the blue solid line shows a fit based on the free electron model and the red dashed line the Drude-Lorentz model. Both models are described by (2.8) with $N = 0$ or 1, respectively. The resulting fit parameters are presented in Table 2.1, where the fit range was limited to energies $\leq 2.75\,\mathrm{eV}$ in both cases.

N	0	1	
ε_b	9.9	8.2	
$\hbar\omega_\mathrm{p}$	9.0	9.0	eV
$\hbar\gamma$	77	77	meV
$\hbar\omega_0$		2.8	eV
$\hbar\omega_{\mathrm{p},0}$		3.0	eV
$\hbar\gamma_0$		660	meV

Table 2.1: Fit parameters of the FEM and Drude-Lorentz model presented in Figure 2.1. The fit function is represented by (2.8) with $N = 0$ or 1, respectively.

As one can see, by adding the contributions of FEM and interband absorption ($N = 1$, red dashed line) the higher energy interband regime is described as well up to about $E = 2.75\,\mathrm{eV}$. According to expectations, as in this extended model a first interband transition is included, the positive background representing all interband transitions ε_b decreased. The further values for plasma frequency ω_p and damping γ are determined by the Drude regime and do not change due to the interband contribution, showing good agreement with the values presented by Berciaud et al. [Ber05].

Notably, the real part of the metals relative permittivity is negative throughout the full

observed spectral range while its imaginary part is non-vanishing. As we will discuss in Chapter 3 and Subsection 5.1 this not only leads to strong absorption $n = \sqrt{\varepsilon}$ but also is a requirement for observing surface bound modes whose propagation direction is locked to their respective spin.

Chapter 3

Surface Plasmon Polaritons

Now that we know the relevant optical properties of metals for the description of surface bound modes, in this chapter the surface plasmon polariton (SPP) – the paragon of a surface bound wave – is introduced. These surface plasmon polaritons describe the coupled oscillation of conduction electrons at the surface of the metal (surface plasmon) in line with the evanescent electromagnetic wave that is propagating at the interface of metal and dielectric (polariton). The evanescent confinement enables the concentration of the electromagnetic field into a volume smaller than the wavelength of the light, which is one of the interesting features in plasmonic structures. To that end we solve the Maxwell's equations at the interface of metal and dielectric. As a result we will obtain the dispersion relation of SPPs connecting the energy of the wave with its momentum, which allows to calculate the electric field distribution of these waves as well. Under normal conditions it is not possible to fulfil both energy and momentum conservation at the same time on a perfectly flat gold film. We will describe how the excitation of surface plasmon polaritons is still achieved by a sophisticated patterning of the gold film. Finally, we will discuss a related electromagnetic wave named Wood's anomaly, which is not describing a surface bound wave but a wave diffracted by a grating into the plane parallel to the interface of metal and dielectric. This chapter is based on References [Mai07; Nov12], both giving a very good introduction into the physics of surface plasmon polaritons.

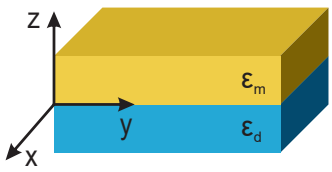

Figure 3.1: Sketch of the geometry used for the description of surface plasmon polaritons propagating at the interface of metal ε_{m} and dielectric ε_{d}. Note that the interface is located in the xy-plane while the SPP is propagating solely in y-direction in the following calculations.

3.1 Fresnel Equations

For the introduction of these surface bound modes some knowledge about the boundary conditions and the corresponding Fresnel coefficients is helpful. Clearly the Maxwell's equations also hold for the boundaries of two adjacent materials, though it is advisable to use their respective integral form in this case. We will consider the interface of metal (j =m) and dielectric (j =d), with their refractive index n_j and the electric field $\boldsymbol{E}_j$ correspondingly. As shown in Figure 3.1 we furthermore define the z-direction as perpendicular to the interface. One can conclude from Faraday's law (2.1a) in integral form that the electric field components parallel to the interface $E_{\mathrm{x},j}, E_{\mathrm{y},j}$ remain unchanged in both materials. According to the third Maxwell equation (2.1c) on the other hand the dielectric displacement field is source free in absence of external stimuli and thus the normal to the interface $D_{\mathrm{z},j}$ is retained as well. These two considerations lead to the following boundary conditions at the interface of two media

$$E_{\mathrm{x,m}} = E_{\mathrm{x,d}}, \tag{3.1a}$$

$$E_{\mathrm{y,m}} = E_{\mathrm{y,d}}, \tag{3.1b}$$

$$\varepsilon_{\mathrm{m}} E_{\mathrm{z,m}} = \varepsilon_{\mathrm{d}} E_{\mathrm{z,d}}. \tag{3.1c}$$

The Fresnel coefficients describing the reflected and transmitted intensities at such an interface can be deduced by applying these boundary conditions to an incident plane wave resulting in

$$r_{\mathrm{TM}}^{0\to1} = \frac{\varepsilon_0/k_{\mathrm{z},0} - \varepsilon_1/k_{\mathrm{z},1}}{\varepsilon_0/k_{\mathrm{z},0} + \varepsilon_1/k_{\mathrm{z},1}} \quad \text{and} \quad t_{\mathrm{TM}}^{0\to1} = \left(\frac{\varepsilon_0}{\varepsilon_1}\right)^2 \left(1 + r_{\mathrm{TM}}^{0\to1}\right). \tag{3.2}$$

Here $r_{\mathrm{TM}}^{0\to1}$ is the reflection and $t_{\mathrm{TM}}^{0\to1}$ the transmission coefficient describing the change in intensity and phase of a wave propagating inside of medium 0. These quantities further simplify if both media have positive and purely real relative permittivity. Within this approximation the values for the light's incidence angle on the interface θ_0 in medium 0 and θ_1 in medium 1 are related by Snell's law

$$n_0 \sin(\theta_0) = n_1 \sin(\theta_1). \tag{3.3}$$

A more detailed description can be found in the textbook by Novotny and Hecht [Nov12, pp. 19-22].

3.2 Polarization of Surface Bound Waves

For the derivation of surface plasmon polaritons, we will limit our considerations in the following to an electromagnetic plane wave propagating in y-direction as

depicted in Figure 3.1 (i.e. $k_\mathrm{x} = 0$). Furthermore we consider only the transverse magnetic (TM) mode, as it can be shown easily that no surface modes exist in transverse electric (TE) polarization [Mai07, pp. 26-27]. For the transverse magnetic mode $\boldsymbol{k} \cdot \boldsymbol{H} = k_\mathrm{y} H_\mathrm{y} + k_\mathrm{z} H_\mathrm{z} = 0$ holds. Only when additionally assuming $H_\mathrm{y} = H_\mathrm{z} = E_\mathrm{x} = 0$ this leads to a non-vanishing solution of Maxwell's equations in both half-spaces simultaneously. The electric field of this wave consequently reads

$$\boldsymbol{E}_j(y,z) = \boldsymbol{E}_0 \mathrm{e}^{\mathrm{i}k_{\mathrm{z},j}z} \mathrm{e}^{\mathrm{i}(k_\mathrm{y} y - \omega t)} \quad \text{where} \quad j = \mathrm{m}, \mathrm{d}. \tag{3.4}$$

Please note that here (3.1b) was taken into account, stating that the y-component of the electric field parallel to the interface is conserved (i.e. also at $t = 0, z = 0$) and thus $k_{\mathrm{y,m}} = k_{\mathrm{y,d}} = k_\mathrm{y}$ or in other words

$$k_\mathrm{y}^2 = \varepsilon_j \left(\frac{\omega}{\mathrm{c}}\right)^2 - k_{\mathrm{z},j}^2 \quad \text{where} \quad j = \mathrm{m}, \mathrm{d}. \tag{3.5}$$

Inserting this ansatz into Eq. (2.1c) yields two additional equations for metal and dielectric separately

$$k_y E_{\mathrm{y},j} + k_{\mathrm{z},j} E_{\mathrm{z},j} = 0 \quad \text{where} \quad j = \mathrm{m}, \mathrm{d}. \tag{3.6}$$

In combination (3.1) and (3.6) form the following system of equations

$$\begin{pmatrix} 1 & 0 & -1 & 0 \\ k_\mathrm{y} & k_{\mathrm{z,m}} & 0 & 0 \\ 0 & 0 & k_\mathrm{y} & k_{\mathrm{z,d}} \\ 0 & \varepsilon_\mathrm{m} & 0 & \varepsilon_\mathrm{d} \end{pmatrix} \cdot \begin{pmatrix} E_{\mathrm{y,m}} \\ E_{\mathrm{z,m}} \\ E_{\mathrm{y,d}} \\ E_{\mathrm{z,d}} \end{pmatrix} = \mathbf{0}, \tag{3.7}$$

which has non-trivial solutions only if the matrix determinant is vanishing. This is accurate in two possible cases, either for $k_\mathrm{y} = 0$ thus describing a wave not propagating along the interface, or for

$$\frac{k_{\mathrm{z,m}}}{\varepsilon_\mathrm{m}} = \frac{k_{\mathrm{z,d}}}{\varepsilon_\mathrm{d}}, \tag{3.8}$$

which indeed is describing a propagating solution along the interface. Going back to (3.5) and inserting what was just deduced finally allows to receive the dispersion relation of the surface plasmon polariton waves

$$k_\mathrm{x}^2 = 0, \tag{3.9a}$$

$$k_\mathrm{y}^2 = \frac{\varepsilon_\mathrm{m}\varepsilon_\mathrm{d}}{\varepsilon_\mathrm{m} + \varepsilon_\mathrm{d}} \frac{\omega^2}{\mathrm{c}^2} \quad \text{and} \tag{3.9b}$$

$$k_{\mathrm{z},j}^2 = \frac{\varepsilon_j^2}{\varepsilon_\mathrm{m} + \varepsilon_\mathrm{d}} \frac{\omega^2}{\mathrm{c}^2} \quad \text{where} \quad j = \mathrm{m}, \mathrm{d}. \tag{3.9c}$$

Given the importance of this relation, we will discuss the conditions for a surface mode to exist in more detail. The following discussion will be slightly simplified by neglecting the small imaginary part of the metals relative permittivity, allowing a more intuitive description. For an undamped propagating mode the wave vector of the SPP in y-direction needs to be purely real. In other words both the numerator $\varepsilon_\mathrm{m}\varepsilon_\mathrm{d}$ and denominator $\varepsilon_\mathrm{m}+\varepsilon_\mathrm{d}$ in the fraction of k_y should have the same sign, both being either positive or negative. Additionally we require the wave to be bound to the interface and thus the wave vector in z-direction is required to be imaginary, i.e. with the fraction in $k_{\mathrm{z},j}$ (3.9c) having an overall negative sign. As the numerator ε_j^2 is positive, the two conditions

$$\varepsilon_\mathrm{m}+\varepsilon_\mathrm{d}<0 \quad \text{and} \quad \varepsilon_\mathrm{m}\varepsilon_\mathrm{d}<0 \tag{3.10}$$

can be formulated for enabling the SPPs. Consequently one of the dielectric functions must be negative, which is the case for metals as shown exemplary for gold in Section 2.4. [Nov12, p. 379]

Figure 3.2 depicts the dispersion relation of surface plasmon polaritons at three distinct interfaces. On the left in Figure 3.2a the first two interfaces are shown over a broad energy range of up to 3.5 eV. Here, the SPP propagating at the interface of gold / air with $\varepsilon_1 = 1$ is represented by the solid line, while for the second gold / dielectric interface $\varepsilon_2 = 4$ holds, resulting in the dash-dotted line.

Two branches of the dispersion can be distinguished, one in the higher and one in the lower energy range. For lower energies the dispersion closely follows the $\theta = 90°$ light line generally described by $\hbar\omega = \hbar c\Re(k_\mathrm{y})\varepsilon_j^{-1/2}\sin(\theta)$ as marked by the coloured area ($j = 1$ in yellow and $j = 2$ in red). Consequently, within the light cone normal incidence $\theta = 0°$ is corresponding to the left border and grazing incidence $\theta = 90°$ is situated at the right border. With increasing energy the distance with respect to the light cone increases first. At intermediate energies of about 2 eV to 2.5 eV the dispersion bends back and subsequently crosses the light line. This back-bending induces an upper limit for the maximum SPP wave vector.

At higher energies the dash-dotted line is located inside the red marked area and the so called Brewster mode is observed, which thus may be excited by incident light. However this mode does not represent a real surface bound wave and rather describes the wave propagation into the metal – i.e. in z-direction – and thus is not of interest here. In the other case of air as dielectric this mode is not directly observed in the dispersion diagram due to the lower ε_1 and the imaginary part of the gold's dielectric function.[1]

[1] More precisely, the Brewster mode may be observed only in dielectrics where $-\varepsilon_\mathrm{d} < \Re(\varepsilon_\mathrm{m}) < -\frac{3}{4}\varepsilon_\mathrm{d}$ is fulfilled.

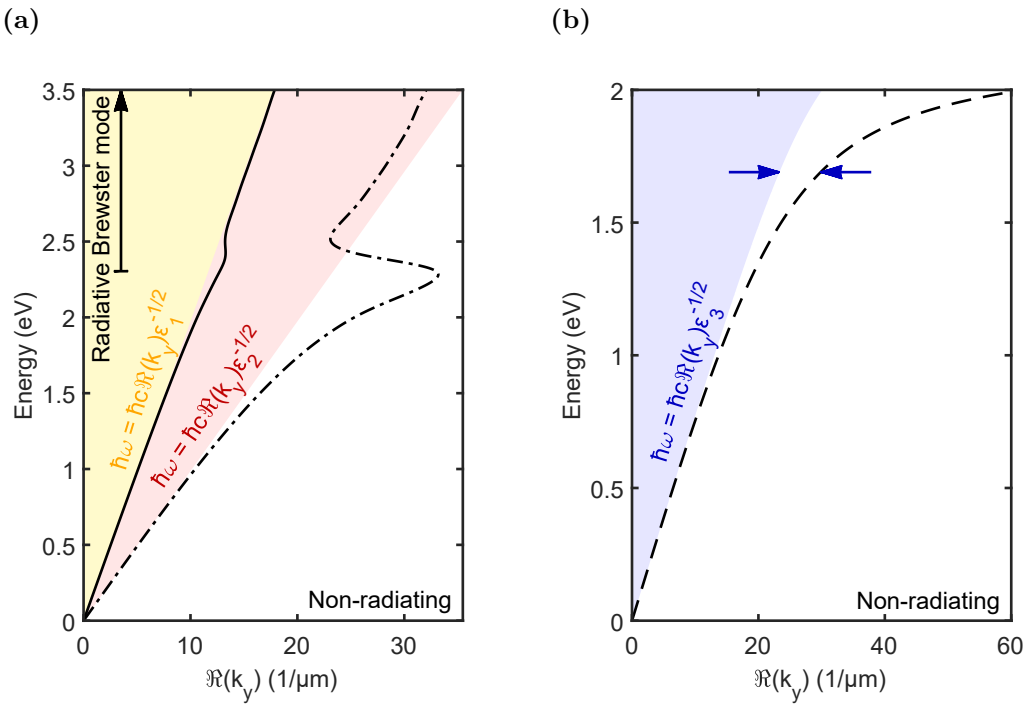

Figure 3.2: **(a)** Dispersion relation of surface plasmon polaritons propagating along the interface of a dielectric and a flat gold film. As first dielectric air with $\varepsilon_1 = 1$ is considered (solid line) and secondly an arbitrary dielectric with $\varepsilon_2 = 4$ is chosen (dash-dotted line). The area marked in yellow comprises all modes that can be addressed in air by incident light, i.e. the left border of this area corresponds to $\theta = 90°$ while at the right border $\theta = 0°$ holds. In the other dielectric on the other hand the red marked area is addressable. Consequently the modes present in the rightmost unmarked area are considered the non-radiative modes. At higher energies the so called Brewster mode is present, not describing true surface waves but wave propagation into the metal instead. **(b)** As third dielectric $Cd_{0.73}Mg_{0.27}Te$ was chosen (dashed line) with an energy dependent ε_3 [Lip69]. One can see for all three dielectrics the wave vector mismatch of the SPP mode with respect to their corresponding light cone, shown exemplary by the blue arrows at $E = 1.69\,\text{eV}$. In fact the mismatch of light incident from air and the (Cd,Mg)Te / Au SPP is even larger. Thus surface plasmon polaritons on a flat gold film can not be excited by incident light irrespective of the selected dielectric material. The relative permittivity of gold was taken from experiment in all cases [Joh72] and is extended at low energy values $E < 0.64\,\text{eV}$ by the FEM (2.6).

As discernible in Figure 3.2b where the focus lies in the lower energy region $E < 2\,\mathrm{eV}$, surface plasmon polaritons can not be addressed by incident light in contrast to the Brewster mode discussed before. Here the case of an SPP at the gold / $Cd_{0.73}Mg_{0.27}Te$ interface is shown by the dashed line and the related blue marked light cone. The main reason why surface plasmon polaritons can not be excited is the wave vector mismatch of the dispersion with respect to the corresponding light cone. This mismatch is indicated by the blue arrows at $E = 1.69\,\mathrm{eV}$, which is present though for all three examples shown. There are ways to overcome this lattice mismatch which will be discussed in Section 3.3, but for now we will take a brief look at the electric near-field distribution of this particular surface plasmon polariton.

With all components of the wave vector being known, we can fully describe the electric field of a surface plasmon polariton in the following way [Mai07, p. 25]

$$\boldsymbol{E}_j \propto \begin{pmatrix} 0 \\ k_{\mathrm{z},j} \\ -k_{\mathrm{y}} \end{pmatrix} \frac{e^{\mathrm{i}(k_{\mathrm{y}}y + k_{\mathrm{z},j}z) - \mathrm{i}\omega t}}{\varepsilon_0 \varepsilon_j \omega} \quad \text{where} \quad j = \mathrm{m}, \mathrm{d}. \tag{3.11}$$

The corresponding electric field distribution at an energy of $\hbar\omega = 1.67\,\mathrm{eV}$ is shown in Figure 3.3, where the colour scale represents the electric field intensity $\Re(\boldsymbol{E})^2$, while the arrows represent the electric field vector $\Re(\boldsymbol{E})$. Here the upper layer is the metal (Au) while as dielectric the material $Cd_{0.73}Mg_{0.27}Te$ was chosen consistently with the actual studied samples presented in Section 6. $\varepsilon_{\mathrm{m}}(1.67\,\mathrm{eV}) = -19.574 + 1.216\mathrm{i}$ [Joh72] and $\varepsilon_{\mathrm{d}}(1.67\,\mathrm{eV}) = 7.369$ [Lip69] are used as relative permittivities. The interface of these two materials is indicated by the black line at zero depth. One can clearly see the evanescent character of these interface bound waves, which is characterized by the respective energy attenuation length of $L_{\mathrm{m}} = 1/(2\Im(k_{\mathrm{z,m}})) \approx 11\,\mathrm{nm}$ in the metal and $L_{\mathrm{d}} = 1/(2\Im(k_{\mathrm{z,d}})) \approx 28\,\mathrm{nm}$ in the dielectric. Notably, the electric field's energy is confined spatially in a sub-wavelength region close to the interface. This is a key feature present in plasmonic systems and allows to sensitively probe changes of the material properties near the interface. One thus could think of miniaturized photonic circuits with length scales that are much smaller than those currently achieved [Bar03] and even use the excited surface plasmon polaritons to taylor the cooling processes in the metal [Spi16] to mention only two examples.

In the direction of propagation as indicated by the black arrow, the energy attenuation length is considerably larger with $1/(2\Im(k_{\mathrm{y}})) \approx 924\,\mathrm{nm}$ for the SPP with wavelength $\lambda_{\mathrm{SPP}} = 2\pi/\Re(k_{\mathrm{y}}) = 216\,\mathrm{nm}$. In fact, the wavelength of the SPP is always shorter with respect to the wavelength in the dielectric material. Interestingly, due to the Drude-like as well as the interband damping in real metal, the $1/\sqrt{e}$ propagation length (after which the light intensity $\propto |E|^2$ has decayed by a factor e) of the

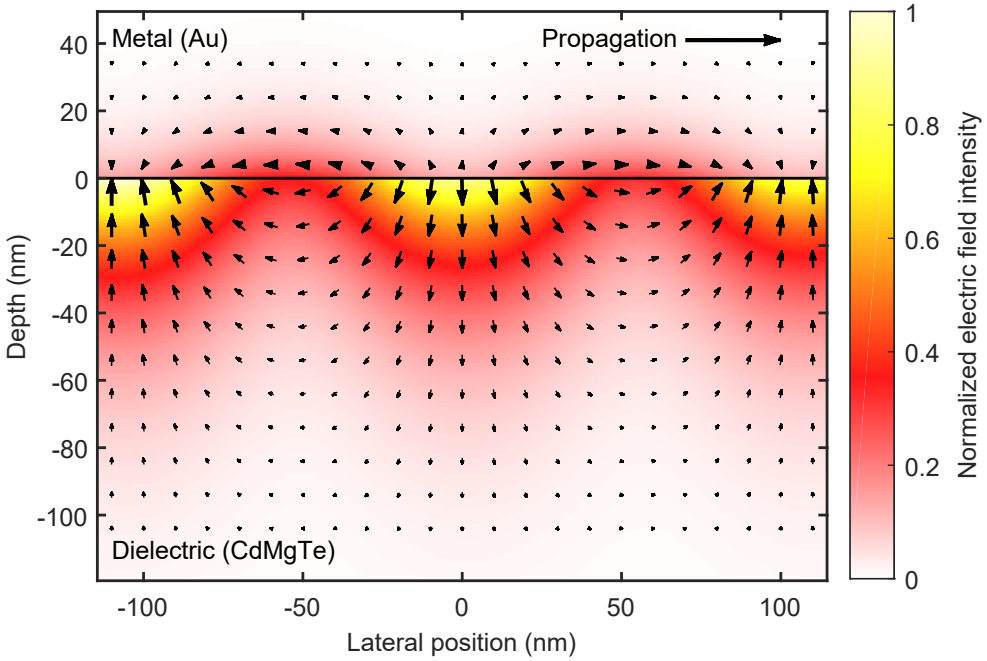

Figure 3.3: Electric field distribution of an SPP propagating along the interface of gold and $Cd_{0.73}Mg_{0.27}Te$ according to 3.9 and 3.11. The distribution has only one parameter namely its energy $E = \hbar\omega = 1.67\,\text{eV}$, while all other properties defined by the refractive indices of gold and $Cd_{0.73}Mg_{0.27}Te$, which were determined by Johnson and Christy [Joh72] and Lipson and Lipson [Lip69] respectively.

surface plasmon polariton is limited to approximately four times its wavelength at this energy.

If air is considered as the dielectric ε_d instead, this propagation length is drastically increased to about 35 µm for an SPP wavelength of 723 nm. Regarding the propagation length, indeed air is the ideal dielectric as one can see from this example. Still (Cd,Mg)Te is used as the dielectric of choice in our case which enables us to place the interface in proximity of a (Cd,Mn)Te quantum well (QW) for which the (Cd,Mg)Te is used as surrounding material and as a spacer with freely selectable thickness, in contrast to the case of air as the dielectric.

3.3 Excitation of Surface Plasmon Polaritons

We will now come back to the problem of having a wave vector mismatch between the incident light and the surface plasmon polariton that we want to excite, as mentioned in the last section. This was shown in Figure 3.2b, where the wave vector of the SPP is to the right of the light cone and thus has larger momentum than the incident light, irrespective of the incidence angle chosen $0° \leq |\theta| \leq 90°$. In this case the two prerequisites of energy and momentum conservation can not be fulfilled at the same time and consequently incident light can not excite an SPP wave at the interface of flat metal and dielectric.

Fortunately the wave vector mismatch can be overcome by two fundamentally different approaches, involving either an additional optical element close to the interface or a specific structuring of the sample itself. The first rather simple of these strategies is based on a prism in total internal reflection geometry within proximity of the interface, enabling a coupling via photon tunnelling. Here two geometries are distinguished, the Otto [Ott68] and Kretschmann [Kre68] configuration, in dependence of the material – dielectric or metal – to which the prism is in contact. Furthermore near-field scanning optical microscopy (NSOM) may be used with its confined optical near field allowing photon tunnelling from the tip's sub-wavelength aperture into the metal film. In contrast to these approaches utilizing a macroscopic optical element, either a prism or tip, we focus on the second variant including microscopic structuring of the sample itself. [Mai07, pp. 42-50]

There are several ways to enable diffraction, like focusing the light on the sample edge, on a single groove in the metal film or by exploiting the samples intrinsic surface roughness. One more prominent example, which is used throughout our studies discussed in this thesis, is the use of a hybrid plasmonic semiconductor structure with a grating coupler, instead of using the flat gold film used in the calculations shown before. The coupler is formed by perforating the gold film periodically in a distance of several 100 nm called grating period a, each time removing a slit with a size on the order of 10 nm from the film as described later in Section 6. For the sake of simplicity, we will limit ourselves to gratings with periodicity in y-direction. As described before this method is based on diffraction, which in this case takes place on the grating structure, resulting in several diffracted beams. These beams are distinguishable based on their respective diffraction order $m \in \mathbb{Z}$ describing the increase or decrease of the in-plane wave vector k_y by multiples of the grating's reciprocal lattice vector $2\pi/a$

$$k_{SPP} = k_y + \frac{2\pi}{a} m, \tag{3.12}$$

while the perpendicular component k_x remains unchanged.

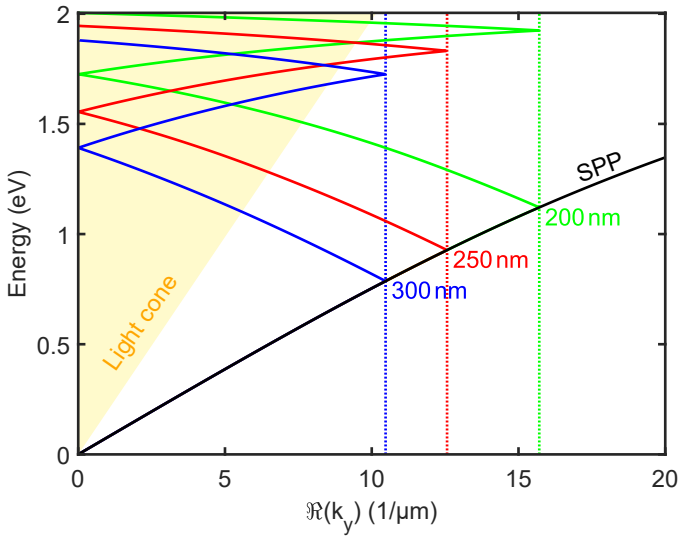

Figure 3.4: Dispersion of the unfolded $m = 0$ surface plasmon polariton at the interface of gold and $Cd_{0.73}Mg_{0.27}Te$ represented by the solid line, as shown already in Figure 3.2b. Additionally three different folded SPP dispersions are shown in green ($a = 200\,\text{nm}$), red (250 nm) and blue (300 nm). Each of these three curves consist of a lower branch with negative group velocity $v_g = d\omega/dk < 0$ where $m = -1$ and a higher energetic branch $m = +1$ that is propagating in positive y-direction. The area marked in yellow represents the $0° \leq \theta \leq 90°$ light cone in air, in which the now folded SPP dispersion is located. Due to the grating structure, incident light allows to excite SPPs at an energy tunable by the grating constant.

Now we are finally in a situation where surface plasmon polaritons can be excited by incident light as both wave vectors can be matched $k_0 \sin(\theta) = k_y + {}^{2\pi m}/_a$, with the wave vector of light in air/vacuum $k_0 = 2\pi/\lambda = \hbar\omega/c$. This is illustrated in Figure 3.4. The unfolded ($m = 0$) SPP dispersion describing the propagation at a $Cd_{0.73}Mg_{0.27}Te$ / gold interface lays still outside the light cone. Its folded replicas on the other hand cross the yellow marked light cone, with the exact curve shape depending on the grating parameter a.The three distinct replicas of the SPP dispersion are folded back into the first Brillouin zone $-\pi/a < \Re(k_y) \leq \pi/a$ of their respective grating (green $a = 200\,\text{nm}$, red 250 nm and blue 300 nm dotted line). Here, the energetically lowest branch corresponds to the $m = -1$ diffracted dispersion and for the highest branch shown $m = -2$ holds, both possessing a negative group velocity $v_g = d\omega/dk < 0$. The third branch energetically in between has positive group velocity and $m = +1$. These SPP branches describing waves propagating in opposite y-direction meet solely at $k_y = \theta = 0$, e.g. at around $E = 1.5\,\text{eV}$ with the corresponding SPP wave number being $k_{SPP} = 2\pi m/a$ where $m = \pm 1$. A second crossing point is imaginable at the edge of the Brillouin zone, though no excitation

with incident light is allowed there for the shown grating parameters. Further even higher diffraction orders $m = +2, -3, +3...$ are present but not shown here in order to avoid confusion. The comparison of the three folded SPP dispersion curves illustrates that an increased lattice constant a results in a decreased course of the dispersion curve with respect to the energy at an arbitrary point within the dispersion diagram. The position of the first $k_{\mathrm{y}} = 0$ intersection of the $m = \pm 1$ branches for example can be tailored to be at a specific energy by choosing the correct grating constant. This is indeed what we will do later in Subsection 8.2.5, in order to improve the overlap of an energetically fixed exciton resonance with the SPP dispersion curve.

The description of the SPP dispersion of a plasmonic grating by the dispersion of a smooth film being folded back into their first Brillouin zone, without having any further effect on their wave vector or energy, is just a first approximation. It is called the empty lattice approximation, as it is valid only for bulk material where the energy of electrons in this so called empty lattice (i.e. with a close to constant potential) is the same as for free electrons. This means it is valid in this special case of a plasmonic grating for

1. thick gold and dielectric films where the respective thickness is much larger than the energy attenuation length $h_j \gg L_j$ where $j = \mathrm{m}, \mathrm{d}$ and
2. in the limit of very small slit sizes $w \ll a$.

For a real hybrid plasmonic semiconductor structure typically both these requirements are not fully satisfied. This results in the need for a more sophisticated description of the SPP dispersion, as the perturbation induced by an either too thin gold layer or a too wide slit size induces an interaction of different SPP modes. As a consequence band gaps are formed within the SPP dispersion, not only at the edge of the Brillouin zone but also at its centre. [Gru06, p. 113]

3.4 Wood's Anomaly

There is one exceptional case worth to mention here, which occurs when the diffracted light propagates along the interface and thus for the diffracted angle $\theta_m = 90°$ holds. In this case

$$\sin(\theta_m) = 1 = \frac{1}{\sqrt{\varepsilon}_{\mathrm{d}}} \left(\sin(\theta) + \frac{\lambda}{a} m \right) \quad \text{where} \quad m = \pm 1, \pm 2, \pm 3... \tag{3.13}$$

the light is diffracted into the y-direction and propagates along the metal dielectric interface. This second surface wave named Wood's anomaly was observed in the reflection spectra of metal gratings already in 1902 by Wood [Woo02]. Both surface

waves, the surface plasmon polariton (3.12) and the one described in (3.13) lead to an increased absorption and re-emission of the absorbed light to some extend and are observed in our experiments due to their distinct features in the spectrum of emitted/reflected light, as discussed e.g. in Subsection 8.3.3. While already discovered in the very beginning of the 20th century, the accurate description required decades to be found until the 1970s where the use of laser sources and photoresist layers allowed to manufacture high quality grating structures for the first time. [May12]

Chapter 4

Magneto-Optical Effects

Until now we discussed how an electromagnetic wave behaves when being incident on the surface or an interface of non-magnetic media. But in fact this behaviour may strongly change for magnetized media, irrespective of how this magnetization is achieved. This could be either due to an external magnetic field or just be caused by the intrinsic magnetic order in some media. There are several magneto-optical effects, which are distinguished based on the geometry they occur in. The first magneto-optical effect was already discovered in 1846 by Faraday [Far46], who observed a polarization rotation of the light that was transmitted through magnetized glass. This effect is called Faraday effect, if the magnetization of the medium is oriented parallel to the propagation direction of the transmitted light. In 1877 Kerr [Ker77] discovered a rotation of the polarization direction and a change in ellipticity of initially linear polarized light reflected from the pole of an electromagnet. While this effect is often referred to as the Kerr effect the precise term is polar magneto-optical Kerr effect, as there are also other manifestations of such effects in reflection. One further example of a related effect is the transverse magneto-optical Kerr effect, discovered in 1896 by Zeeman [Zee96]. In this chapter an introduction into the origins of the magneto-optical effects will be given. As essentially all magneto-optical effects are a consequence of the Zeeman effect [Zve97, Ch. 1], the related giant Zeeman effect in the studied (Cd,Mn)Te diluted magnetic semiconductor systems will be described as a starting point in this chapter.

4.1 Giant Excitonic Zeeman Effect in (Cd,Mn)Te

In this section the giant Zeeman effect of excitons in (Cd,Mn)Te will be described. For a proper description of the magnetic properties of this material, one should take into account that pure CdTe is diamagnetic. If now a small share of the diamagnetic Cd is substituted by paramagnetic Mn, the resulting (Cd,Mn)Te compound is called a diluted magnetic semiconductor (DMS). In these DMS structures the sp–d exchange

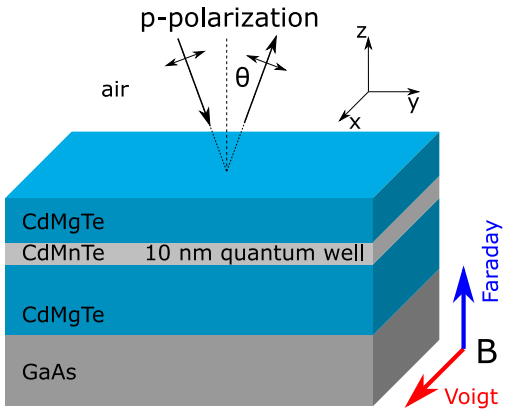

Figure 4.1: (Cd,Mn)Te quantum well structure within an external magnetic field applied either in Faraday (blue arrow) or Voigt geometry (red arrow).

interaction of the d-band electrons of the magnetic ions with the conduction band electrons (s-band) and valence band holes (p-band) allows to achieve a large exciton Zeeman splitting already in moderate external magnetic fields [Gaj78; Fur88; Gaj10]. The alignment of magnetic moments of the Mn^{2+} ions consequently dominates the overall magnetization in such a crystal at low temperatures. While the magnetization increases linearly at low magnetic field strength, it is saturating at high magnetic field. Such an evolution of the magnetization can be modelled for a system of non-interacting spins with total spin quantum number S by the Brillouin function

$$B_S(\xi) = \frac{2S+1}{2S} \coth\left(\frac{2S+1}{2S}\xi\right) - \frac{1}{2S} \coth\left(\frac{1}{2S}\xi\right). \tag{4.1}$$

In the present case of (Cd,Mn)Te the Mn^{2+} ions have $S = 5/2$ due to the half-filled d-type subshell [Gaj10, p. 14].

4.1.1 Faraday Geometry

The assumption of non-interacting manganese ions holds only for very low Mn concentrations below 1 %, while for higher concentrations the Mn ions begin to order antiferromagnetically. This leads to a decrease in the resulting magnetization per Mn ion. If we consider the magnetization as the mean spin value per Mn^{2+} ion instead, and thus consider only the isolated Mn ions, an empirical description can be obtained by introducing a temperature correction T_0, while keeping the spin quantum number S unchanged. The mean spin component in Faraday magnetic field (z-direction, see

Figure 4.1) reads

$$\langle S_\mathrm{z}\rangle = SB_S(\xi) \quad \text{where} \quad \xi = \frac{g_\mathrm{Mn}\mu_\mathrm{B}S}{k_\mathrm{B}(T-T_0)}B, \tag{4.2}$$

$g_\mathrm{Mn} = 2$ is the electron g-factor, μ_B is the Bohr magneton, k_B is the Boltzmann constant, B is the magnetic field strength and T is the temperature. The temperature offset T_0 generally depends on the Mn mole fraction of the compound semiconductor and is used as a fit parameter in our case.

The magnetic ions are aligned by an external magnetic field B, while the carriers are influenced via ion-carrier interaction. We will describe this interaction in the mean field approximation and thus consider the mean spin $\langle S_\mathrm{z}\rangle$ in the thermal equilibrium instead of the individual Mn^{2+} spins. Furthermore we presume that the virtual crystal approximation holds and thus the random magnetic ion distribution is replaced by an artificial periodical structure i.e. restoring the crystal periodicity. Within these approximations the conduction band splits into two components at the Γ-point of the Brillouin zone, both possessing the opposite spin $S_\mathrm{e,z}$. The energy level splitting of the conduction band in Faraday geometry (F) is thus given by

$$\Delta E_\mathrm{e,F} = N_0\alpha x S_\mathrm{e,z}\langle S_\mathrm{z}\rangle \qquad \text{where} \quad S_\mathrm{e,z} = \pm\frac{1}{2}. \tag{4.3a}$$

The valence band on the other hand splits into four equidistant components distinguished by the hole spin $J_\mathrm{h,z} = \pm 1/2$ for the light holes and $\pm 3/2$ for the heavy holes. The energy level splitting in this case is given by

$$\Delta E_\mathrm{h,F} = \frac{N_0\beta}{3} x J_\mathrm{h,z}\langle S_\mathrm{z}\rangle \qquad \text{where} \quad J_\mathrm{h,z} = \pm\frac{1}{2}, \pm\frac{3}{2}. \tag{4.3b}$$

Here x is the concentration of isolated Mn^{2+} ions, $N_0\alpha = 0.22\,\mathrm{eV}$ and $N_0\beta = -0.88\,\mathrm{eV}$ are the exchange integral values of the conduction and valence-band, respectively [Gaj10, pp. 16-18].

As we consider a (Cd,Mn)Te quantum well structure the confinement of excitons in z-direction, perpendicular to the quantum well plane, also plays an important role. We assume that the confinement in z-direction is stronger than the lateral confinement and discuss the theory for (Cd,Mn)Te multiple quantum wells in in-plane magnetic field presented by Kuhn-Heinrich et al. [Kuh94] that was generalized by Poddubny in [Spi18, Ch. S1]. The influence of confinement is discussed further in the next subsection, as it plays a more important role in Voigt geometry.

The level splitting of electrons (e) and holes (h) is shown in Figure 4.2a by the black lines. The heavy and light hole valence bands are split at zero magnetic field by Δ_lh (purple arrow). Furthermore, the four relevant dipole-allowed transitions within

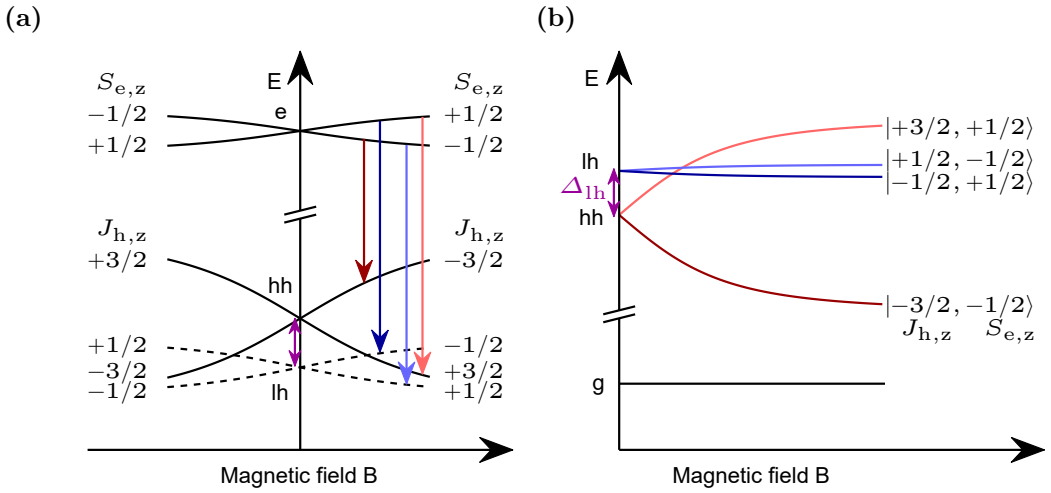

Figure 4.2: (a) Energy diagram and Zeeman splitting of conduction and valence band states in Faraday geometry (single particle picture). The heavy and light hole valence bands are split by Δ_{lh} as shown by the purple arrow. Vertical lines indicate the relevant dipole-allowed optical transitions with circular polarization in the xy-plane (see Figure 4.1 for the geometry). The dark and light lines correspond to σ^+/σ^- polarization respectively. **(b)** Energy diagram from **a** in the exciton picture. In the high magnetic field limit, the giant Zeeman splitting overcomes the hh-lh splitting. In this limit, the two central transitions correspond to the light hole exciton ($\mathrm{lh}_{+,-}$, dark and light blue lines, respectively) while the outer ones correspond to the heavy hole exciton ($\mathrm{hh}_{+,-}$, dark and light red lines, respectively). The labelling of exciton states in this case is given by the $|J_{\mathrm{h,z}}, S_{\mathrm{e,z}}\rangle$ notation.

magnetic field are shown by the coloured arrows. The two left transitions represented by the dark red and dark blue line are σ^+ circularly polarized with $S_{\mathrm{e,z}} - J_{\mathrm{h,z}} = 1$, while the right two light blue and light red lines are exemplary for the σ^- transitions where $S_{\mathrm{e,z}} - J_{\mathrm{h,z}} = -1$ holds. With two further approximations, i.e. neglecting the $e-h$ exchange interaction and the use of a constant exciton binding energy, the exciton Zeeman splitting of these four transitions can easily be calculated as the difference of the band splittings presented in Figure 4.2a. The strongest splitting in Faraday geometry is thus observed for the heavy hole excitons with the Zeeman splitting

$$\Delta E_{\mathrm{hh,F}} = N_0(\alpha - \beta)x\langle S_{\mathrm{z}}\rangle. \tag{4.4a}$$

For the light hole exciton, the splitting is weaker with

$$\Delta E_{\mathrm{lh,F}} = N_0(\alpha + \beta/3)x\langle S_{\mathrm{z}}\rangle. \tag{4.4b}$$

These splittings are depicted in Figure 4.2b in the exciton picture, where the red curves show the heavy hole transitions and the blue curves show the light hole transitions.

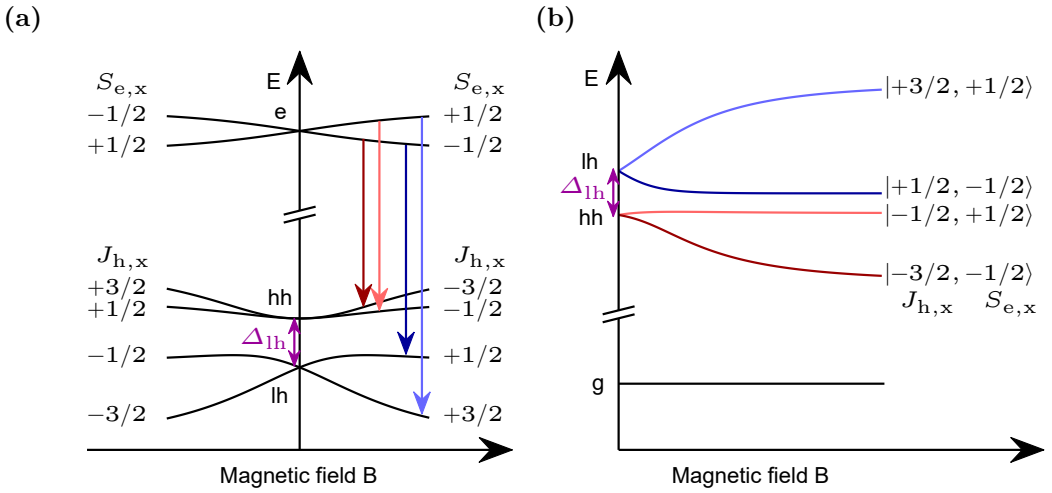

Figure 4.3: (a) Energy diagram and Zeeman splitting of conduction and valence band states in Voigt geometry (single particle picture). Vertical lines indicate the relevant dipole-allowed optical transitions with elliptical polarization in the yz-plane (optical transitions with linear polarization along magnetic field direction are not considered here). Red/blue lines correspond to σ^+/σ^- polarization in the yz-plane in the limit of large magnetic fields where the electron and hole eigenstates are defined by the angular momentum projections on magnetic field direction $S_{e,x}$ and $J_{h,x}$, respectively. At $B = 0$ the heavy hole and light hole states are split by Δ_{lh}. **(b)** Energy diagram from **a** in the exciton picture. For low magnetic fields the upper two transitions correspond to the light hole exciton ($lh_{+,-}$, light and dark blue lines, respectively) while the lower ones correspond to the heavy hole exciton ($hh_{+,-}$ light and dark red lines, respectively). Due to admixture from the light holes to the heavy holes the states at high magnetic field are denoted as labelled within the figure. The labelling of exciton states in this case is given by the $|J_{h,x}, S_{e,x}\rangle$ notation.

The ground state (g) is represented by the black line. The energetically lowest transition is the heavy hole exciton emitting σ^+ polarized light on recombination. For the simulations shown later in this thesis, only the hole contribution of the heavy hole Zeeman splitting is of interest, which reads

$$\Delta_{h,F} = -\frac{\beta}{\alpha - \beta}\Delta E_{hh,F}. \tag{4.5}$$

4.1.2 Voigt Geometry

The Zeeman splitting in Voigt geometry is shown in Figure 4.3a. The conduction band splits in the same way as in the Faraday configuration. For the splitting of the valence band on the other hand, a Luttinger Hamiltonian needs to be solved, which includes both the Zeeman splitting and the effect of size quantization in z-direction.

Instead of presenting the diagonalization step by step, the following discussion will be limited to the most important results.

Let us start with the case of zero magnetic field. Here the hole angular momentum is oriented in z-direction $\boldsymbol{J}_\mathrm{h} \parallel \boldsymbol{z}$ and thus perpendicular to the QW plane. Heavy and light hole bands split energetically due to the confinement. The effective hole wave vector in z-direction is $k_\mathrm{z} = \pi/h_\mathrm{q}$ in the approximation of infinite barriers and neglecting strain, where h_q is the quantum well thickness. The respective light-heavy hole splitting is proportional to k_z^2 and about

$$\Delta_\mathrm{lh} \approx 20\,\mathrm{meV} \tag{4.6}$$

for the given structure in this approximation. For finite barrier height this splitting is decreased. As experimentally confirmed for this structure from reflection spectra, this decrease is compensated by the additional contribution due to strain and (4.6) holds. Now the heavy hole Zeeman splitting can be evaluated also in Voigt geometry resulting in [Spi18, Supplement S1]

$$\Delta_\mathrm{h,V} = \frac{\Delta_\mathrm{h,F}^3}{18\Delta_\mathrm{lh}^2}. \tag{4.7}$$

As compared to the Faraday geometry the Zeeman splitting is suppressed, as it requires the admixture of light hole states and it is cubic in B in the low magnetic field limit. This can be nicely seen in Figure 4.3a by the two congruent heavy hole (hh) valence bands around $B = 0$. Due to the weaker influence of the confinement on the light hole states their splitting is stronger. With increasing magnetic field strength the angular momentum of the valence band states begins to tilt from z into x-direction until it is fully oriented along the direction of magnetic field $\boldsymbol{J}_\mathrm{h} \parallel x$ in the high magnetic field limit.

Now we will discuss the σ-type optical transitions again that are shown in Figure 4.3a as vertical coloured lines. At zero magnetic field, the transitions of the heavy and light hole states are circularly polarized in the xy-plane, corresponding to the in-plane oscillations of the exciton dipole moment. Due to the transverse magnetic field the light and heavy hole states admix resulting in a tilting of the plane of polarization into the magnetic field direction and consequently elliptical polarization in the yz-plane. In the limit of large magnetic fields the hole angular momentum is oriented in magnetic field direction and both heavy hole transitions are circularly polarized in the yz-plane. Consequently the degree of circular polarization P_c for these two transitions reaches unity in this limit, while it is zero if no magnetic field is applied. Please note that both heavy hole transitions are σ^+ circularly polarized (red arrows in Figure 4.3a) with relative angular momentum projection $S_\mathrm{e,x} = (-1/2)-(-3/2) = (+1/2)-(-1/2) = 1$ and thus i.e. their circular polarization

P_c has the same sign, which is crucial for the observation of the effects discussed in Chapter 8.

In the low magnetic field limit, the degree of circular polarization for the heavy hole excitons reads [Spi18, Supplement S1]

$$P_c \approx \frac{2}{3}\frac{\Delta_{h,F}}{\Delta_{lh}} \propto B \tag{4.8}$$

in the approximation of infinite QW barriers and thus is linear with respect to the magnetic field B, which is surprising at first considering the cubic dependence of the heavy hole Zeeman splitting on the magnetic field strength presented before in Eq. (4.7), but is in full agreement with the experimental data presented in Section 8.4.

4.2 Magneto-Optical Kerr effect

Now that the Zeeman effect and the resulting splitting of energy levels has been introduced, we will proceed with the magneto-optical Kerr effect (MOKE) induced by this level splitting, which describes the influence of magnetization on the light reflected from the surface of a medium. In order to do so, we have to distinguish three distinct geometries of the sample's magnetization with respect to the plane of light incidence, which are illustrated in Figure 4.4. The polar magneto-optical Kerr effect (PMOKE) is shown in Figure 4.4a, with the magnetization in the incidence plane, but oriented perpendicular to the surface $\boldsymbol{M} \parallel \boldsymbol{z}$. In the second case 4.4b the magnetization is longitudinal and thus both in the incidence and surface plane simultaneously $\boldsymbol{M} \parallel \boldsymbol{y}$. The resulting effect is called the longitudinal magneto-optical Kerr effect (LMOKE). The third case is different in this respect, as here the magnetization is perpendicular to the incidence plane $\boldsymbol{M} \parallel \boldsymbol{x}$, as shown in Figure 4.4c. This effect is called the transverse magneto-optical Kerr effect (TMOKE).

The magnetization influences two different properties of the reflected light depending on the geometry that is being observed. More precisely, either the polarization or the intensity of the reflected light is altered. These two influences can be separated depending on the orientation of magnetization with respect to the incidence plane. If the magnetization is in the incidence plane (PMOKE, LMOKE), the reflected light's polarization is changed, while for transverse magnetization (TMOKE) only the intensity of reflected light is altered. One should mention here that all three magneto-optical Kerr effects are ordinarily changing the properties of light reflected from a magnetized sample, although TMOKE for example can be studied also in transmission [Poh13]. This thesis aims not only at elucidating the transverse

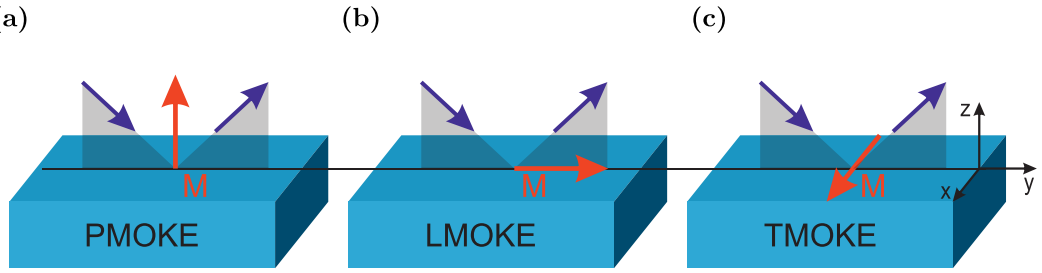

Figure 4.4: Three different geometries in which magneto-optical Kerr effects influence the properties of light reflected from a magnetized material. We distinguish two manifestations of these effects as they either rotate the polarization of the reflected light or change its intensity. The **(a)** polar and **(b)** longitudinal magneto-optical Kerr effect, abbreviated as PMOKE and LMOKE respectively, are inducing a rotation of the polarization called Kerr rotation. The transverse magneto-optical Kerr effect TMOKE **(c)** on the other hand is a pure intensity effect and is in the focus of our studies.

intensity effect TMOKE in the vicinity of narrow optical resonances as discussed in Chapter 9, but also introduces a new class of transverse intensity effect in emission named transverse magnetic routing of light emission (TMRLE), which is presented in Chapter 8.

4.3 Gyrotropic Permittivity

In this section we will further discuss the influence of magnetization on the properties of reflected light by introducing its impact on the relative permittivity tensor $\boldsymbol{\varepsilon}$ of the material under study. The limitation on the dielectric dipole response while neglecting the magnetic dipole response ($\mu = 1$) is a valid approximation as the magnetic response is about four orders of magnitude weaker than its dielectric counterpart in the visible spectral range [Gie09], which is of interest here. The magnetization results in off-diagonal elements of the relative permittivity tensor and as a consequence a different refractive index for left- and right-circularly polarized light. Such a medium is called gyrotropic and can be described in the case of crystals in the following form with implicit summation over a set of indexed terms [Zve97, p. 22]:

$$\varepsilon_{ij} = \varepsilon^0_{ij} - \mathrm{i} e_{ijk} g_k + \delta_{ijkl} M_k M_l, \tag{4.9}$$

where e_{ijk} is the Levi-Civita tensor and $g_k = a_{km} M_m$, with the three tensors $\varepsilon^0_{ij}, a_{km}, \delta_{ijkl}$ defined by the crystallographic symmetry. The effects within this thesis are measured consistently in transverse magnetic field (i.e. in x-direction) and

as the TMOKE is linear in magnetization [Zve97, p. 41] we fixed $\delta_{ijkl} = 0$. This allows to write Eq. (4.9) for isotropic media in the following way

$$\boldsymbol{\varepsilon} = \begin{pmatrix} \varepsilon_\mathrm{d} & 0 & 0 \\ 0 & \varepsilon_\mathrm{d} & -\mathrm{i}g \\ 0 & \mathrm{i}g & \varepsilon_\mathrm{d} \end{pmatrix}. \tag{4.10}$$

With this as a starting point, the derivation of the formula describing the TMOKE strength is possible, though we will show only the result here, as the extensive derivation is rather cumbersome (for details see [Zve97, pp. 43-45]). Furthermore we will consider only the interface of dielectric ε_d and air $\varepsilon_\mathrm{Air} = 1$, which leads us to the characteristic TMOKE parameter δ for the light reflection from a semi-infinite magnetic medium

$$\delta = -\Im\left(\frac{8\varepsilon_\mathrm{d}\tan\theta}{(\varepsilon_\mathrm{d}-1)(\varepsilon_\mathrm{d}-\tan^2\theta)}Q\right) = 2\,\frac{I(\theta,+B)-I(\theta,-B)}{I(\theta,+B)+I(\theta,-B)}. \tag{4.11}$$

Here $Q = g/\varepsilon_\mathrm{d}$ is the so called magneto-optical parameter and θ is the angle of reflection for the light coming from the air side and the reflection occurs at the magnetized dielectric. Furthermore $I(+B)$ and $I(-B)$ are the reflected intensities for the two opposing directions of magnetic field B. [Zve97, p. 47]

One can see from Eq. (4.11) that δ describes the relative change in intensity, induced by the external magnetic field B in the case of a paramagnetic material. For ferromagnetic materials the magnetization should be considered instead. There are a few more things to note here: Firstly, there are two slightly different definitions of the TMOKE δ in literature, which differ by a factor of two. We use the definition from Pohl et al. [Poh13]. Secondly, this definition is slightly simplified from the experimental point of view, as we assume a constant overall intensity $2I(0) = I(+B) + I(-B)$, which holds in the case of TMOKE as it is an uneven effect with respect to the magnetic field B in paramagnetic materials. Ordinarily, the definition of TMOKE uses the formula $\delta = (I(+B) - I(-B))/I(0)$, which requires the knowledge of the reflected intensity at three points in magnetic field instead of two, unnecessarily increasing the measurement duration by about 50 % to 100 %[1].

The TMOKE δ is an uneven function with respect to both the angle of reflection and the magnetic field direction and thus $\delta = 0$ both at $B = 0$ or $\theta = 0$, which we will also see later in the experiment. As we have assumed $\mu = 1$ the TMOKE is observed only in p-polarization and is absent in s-polarization, which is not strictly the case

[1] In ferromagnetic media the intensity in the absence of magnetization $I(M \to 0)$ is difficult to measure directly. Instead usually the average of the two $I(B = 0)$ measurements in either increasing or decreasing magnetic field is used in such a case, thus resulting in the 100 % increased measurement duration stated here.

otherwise if $\boldsymbol{\mu}$ has off-diagonal elements. However, it is usually much weaker than the effect for p-polarized light, which is on the order of $\delta \approx 10^{-4}$ [Bor19] in the case of (Cd,Mn)Te afar from the optically allowed transitions. The small off-resonant effect strength even in p-polarization is a consequence of another property of the TMOKE: It requires an absorptive medium with $\Im(\varepsilon_\mathrm{d}) \neq 0$ as otherwise all contributions in Eq. (4.11) are real numbers and the TMOKE δ vanishes. Interestingly the polar magneto-optical Kerr effect and the transverse counterpart are not independent and instead bound by the following equation:

$$\delta \sin\theta = 4(\Phi_\mathrm{K} - \Psi_\mathrm{K}) \tag{4.12}$$

with the Kerr rotation angle Φ_K and the ellipticity angle Ψ_K in p-polarization [Zve97, pp. 45-45]. Please note that the used definition of δ also gives an additional factor of two here.

4.4 Enhanced Magneto-Optical Effects in Plasmonic Crystals

In dielectric materials the off-resonant TMOKE in the transparency region is very weak, due to the negligible absorption. As a consequence the TMOKE was usually studied in ferromagnetic metals showing a weak spectral dependence within the visible and infrared spectral range with a typical value of $\rho \approx 10^{-3}$ [Kri67]. Resonant TMOKE on the other hand exhibits a notable magnitude even in nearly transparent media when in the vicinity of the absorption band provided by different types of resonances.

These resonances present in hybrid magneto-photonic structures can be provided for example by waveguide modes [Che14; Syl16], optical Tamm states [Vin10] and surface plasmon polaritons [Bel11; Bor18]. One of the interesting features especially of the plasmonic devices is the possibility to localize light to sub-wavelength dimensions. The localized fields result in an enhanced sensitivity to changes of the optical properties near the interface at which the SPP wave is propagating. The combination of plasmonics and magneto-optics is considered mutually beneficial [Aki12]: The magnetic field allows to control the SPP dispersion via the magnetic layer's refractive index, while the SPP localization can be utilized to enhance the magneto-optical effects. These devices allow to combine plasmonic and magneto-optical effects in a single structure and thus belong to the field of research called *magneto-plasmonics*. The interplay of magneto-optics and SPPs was studied in the beginning on smooth ferromagnetic films [Bur86; Hic87]. In a next step bimetallic systems were used consisting of noble and ferromagnetic metals, in which the SPP propagates along the

noble metal / air interface [Gon07; Tem10]. Due to the proximity to the ferromagnetic surface also the TMOKE strength was enhanced.

Nowadays plasmonic crystals (PCs) – the combination of a magnetic layer with a periodically perforated gold film on top – aroused some interest. As shown by Belotelov et al. [Bel11], the TMOKE is enhanced by more than one order of magnitude in a bismuth iron garnet (BIG) PC measured in transmission, reaching about $\delta = 1.5\,\%$ in this structure. By increasing the bismuth substitution level, also the TMOKE strength was enhanced by nearly another order of magnitude to $\delta = 13\,\%$ [Poh13] (shown in Figure 7.5). The increase of the TMOKE is caused mainly by the shift of the SPP resonance in transverse magnetic field [Bel13]. Further examples show that the TMOKE can be drastically enhanced in multiple hybrid metal-dielectric structures at the resonance of the SPPs [Fer11; Bor16; Bos16; Ign16].

Not only the TMOKE but also other magneto-optical effects like the Faraday rotation can be enhanced in such structures. It was shown for a thin-film EuS PC that the Faraday rotation is enhanced by one order of magnitude, due to the interplay of SPPs and photonic waveguide modes in such a system [Chi13]. In their work a Faraday rotation of 14° was observed in a less than 200 nm thick film with embedded gold nanowires at $B = 5\,\mathrm{T}$ and $T = 20\,\mathrm{K}$. Similarly Kreilkamp et al. [Kre13] observed an enhancement of TMOKE in gold nanowires placed on a photonic waveguide, close to the hybrid waveguide-plasmon polariton resonance. They noticed a large TMOKE of $\delta = 1.5\,\%$ while the high transparency of the system was preserved due to the rather large nanowire distance. One should mention that the aforementioned techniques for enhancing the TMOKE share one disadvantage, which is the relative high loss in plasmonic nanostructures in general [Khu15]. As the magneto-optical effects on the other hand can be orders of magnitude larger as compared to the pure magnetic material, the field of magneto-plasmonic is still promising for instance for the development of novel devices in miniaturized photonic circuits [Bel13].

All these studies were performed in a regime that we call the *weak coupling regime*. In this regime the relatively large linewidth Γ of the plasmonic resonances, induced by the strong absorption in metals, significantly exceeds the Zeeman splitting Δ. The spectral dependence of δ in this case shows a characteristic S-shape around the plasmonic resonance, crossing zero at the central frequency and possessing maxima and minima at the slopes of the resonance. In our case on the other hand we deal with narrower resonances compared to the plasmonic excitations. The optical resonances presented here arise from excitons in a diluted magnetic semiconductor QW structure, but also other confined quantum states such as rare earth ions in dielectrics show similarly narrow resonances. Due to the small damping Γ of these resonances accompanied by the giant Zeeman splitting Δ in diluted magnetic semiconductors, the fundamentally new *strong coupling regime* with $\Delta/\Gamma \gg 1$ can be established. In

this second regime the exciton spin precession in magnetic field is faster with respect to the exciton damping Γ, which enables the observation of the Zeeman splitting immediately in the reflectivity spectrum. In the weak coupling regime on the other hand, the splitting is not observed. Not only the reflectivity but also the TMOKE spectrum has a fundamentally different dependence on the Zeeman splitting in these two regimes, which will be discussed in Chapter 9. Surprisingly, TMOKE was not yet studied in this second regime irrespective of the system presented in this thesis.

Chapter 5

Transverse Spin Angular Momentum of Evanescent Surface Waves

Within free space a collimated light beam carries solely a transverse electric field, which is oriented in the plane perpendicular to the propagation direction. Depending on the phase between the two electric field vectors that describe this plane, the light has linear, elliptical or circular polarization. When the light on the other hand impinges on an absorbing material like a metal surface and is reflected, the electric field inside this material possesses both transverse and longitudinal components. Interestingly, the electric field is partially oriented parallel – longitudinal – to the direction of light propagation and moreover the longitudinal component is phase shifted by $\pi/2$ with respect to the transverse one. This results in light elliptically polarized in the plane of incidence, with the electric field spinning in time around its normal vector. This circular motion is described by the transverse spin angular momentum (SAM) of light, which will be discussed in this chapter. See also the progress article by Aiello et al. [Aie15] for a more detailed introduction into this fascinating topic.

5.1 Spin-Momentum Locking at the Metal-Dielectric Interface

Now the transverse angular momentum of light near the interface of an absorptive medium and a dielectric will be further discussed. Rodríguez-Fortuño et al. [Rod13] gave a vivid example of the fascinating phenomena arising from this transverse SAM of light. In his work a circularly polarized dipole is discussed. It is assumed here that the electric field of the dipole emission is oriented in the yz-plane and thus spinning around an axis pointing in x-direction. If this dipole is located in free space, it is emitting with equal intensity into the lateral directions, irrespective of the direction of its circular motion or in other words its transverse SAM S_x. Now we introduce

a medium in proximity of the dipole which is absorptive and assume the normal to the interface pointing in z-direction (see also Figure 5.1). Due to this interface the emission of this dipole becomes directional. Thus, more light is emitted either in positive or negative y-direction, propagating along the surface of this medium as an evanescent wave. The spin of the dipole emitter S_x is locked to the propagation direction $\boldsymbol{k}$ of the launched evanescent wave. This effect is called spin-momentum locking

$$\boldsymbol{k} \propto \boldsymbol{S} \times \boldsymbol{e}_\mathrm{z} \tag{5.1}$$

and will be discussed explicitly in this section [Bli15a; Bli15b]. In the following example we assume a dipole with the dipole moment $\boldsymbol{p}$ that is emitting at $E = 1.67\,\mathrm{eV}$. It is placed near the interface of two semi-infinite homogeneous media, namely in (Cd,Mg)Te with $\varepsilon_1 = 7.4$ and in only $h = -25\,\mathrm{nm}$ distance to the interface of gold with $\varepsilon_2 = -19.6 + 1.2\mathrm{i}$. Thus, this example is closely related to the one already shown in Figure 3.3, where we discussed the electric field distribution of a surface plasmon polariton propagating at the interface of the same materials. As shown in Reference [Spi18] the wave equation with an inhomogeneous source term allows to describe the electric field in the following way

$$\begin{aligned} \nabla \times \nabla \times \boldsymbol{E} - \varepsilon(z) \left(\frac{\omega}{c}\right)^2 \boldsymbol{E} &= \frac{\boldsymbol{p}}{\varepsilon_0} \left(\frac{\omega}{c}\right)^2 \delta(\boldsymbol{r} - \boldsymbol{r}_0) \\ \text{where} \quad \varepsilon(z) &= \begin{cases} \varepsilon_1, & z \leq 0 \\ \varepsilon_2, & z > 0 \end{cases}. \end{aligned} \tag{5.2}$$

Here $\boldsymbol{r}_0 = (0, 0, h)^\top$ is the dipole location and $\boldsymbol{r} = (x, y, z)^\top$ is the position vector.

To explore how the transverse SAM S_x of the dipole emission will influence the emission direction we will solve Eq. (5.2) in the $z \leq 0$ subspace. We want to discuss the case of a dipole with polarization $\boldsymbol{p}$ in the yz plane, which may be given as follows

$$\boldsymbol{p} = \frac{p_0}{2} \begin{pmatrix} 0 \\ \sqrt{1 - P_\mathrm{c}} + \sqrt{1 + P_\mathrm{c}} \\ \mathrm{i} \cdot (\sqrt{1 - P_\mathrm{c}} - \sqrt{1 + P_\mathrm{c}}) \end{pmatrix} \tag{5.3}$$

where P_c is the circular polarization degree in the yz-plane. This dipole is fully circular polarized for $|P_\mathrm{c}| = 1$ and has linear polarization in y-direction for $P_\mathrm{c} = 0$, while the factor p_0 defines the amplitude and relative phase of the dipole emission. Due to the translation symmetry in the x- and y-direction in this rather simple example with two semi-infinite media, a semi-analytical solution to the wave equation exists. This solution is based on the electromagnetic Green's function, which already is the solution of the wave equation for a point source that we need here. In the $z \leq 0$ subspace the emitted electric field is composed of two parts:

$$\boldsymbol{E} = (\boldsymbol{G}_0 + \boldsymbol{G}_\mathrm{R}) \cdot \boldsymbol{p}, \tag{5.4}$$

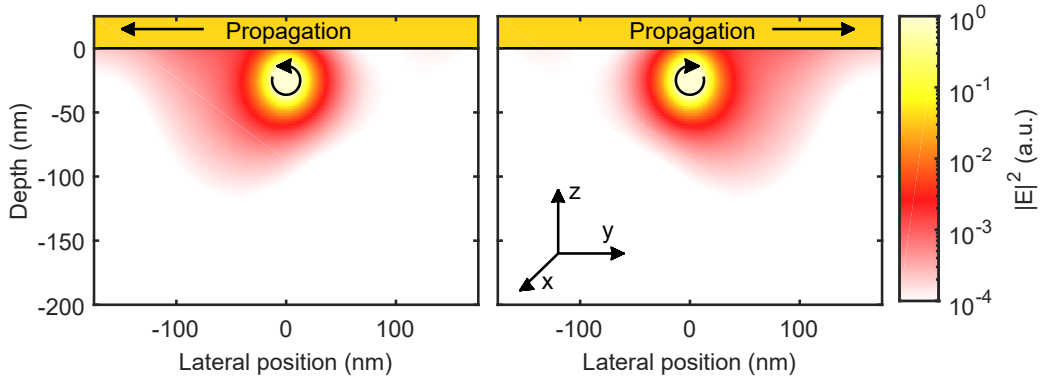

Figure 5.1: Near-field distribution of the electric field E originating from the emission of a dipole. In the left panel a dipole with negative spin $S_\mathrm{x} < 0$ ($P_\mathrm{c} = -1$) is shown, while for the right panel $S_\mathrm{x} > 0$ ($P_\mathrm{c} = +1$) holds. The dipole is placed at $\boldsymbol{r}_0 = (0, 0, -25\,\mathrm{nm})^\top$ inside (Cd,Mg)Te ($\varepsilon_1 = 7.4$) close to an interface with gold as the second medium ($\varepsilon_2 = -19.6 + 1.2\mathrm{i}$). The resulting electric field distribution is uneven: The emitter with $S_\mathrm{x} > 0$ is preferentially emitting in the positive y-direction while the emitter with $S_\mathrm{x} < 0$ emits in the negative y-direction. This is a consequence of the spin-momentum locking in structures with broken mirror symmetry.

where the first part $\boldsymbol{G}_0$ is the Green's function describing the propagation of the emitted light in bulk (Cd,Mg)Te and the second part $\boldsymbol{G}_\mathrm{R}$ describes the contribution from the waves reflected at the gold / (Cd,Mg)Te interface. The part describing the bulk propagation is given by [Spi18, Supplement S2]

$$\boldsymbol{G}_0(\boldsymbol{r}, \boldsymbol{r}_0) = \left(\left(\frac{\omega}{c}\right)^2 \mathbb{1} + \frac{\boldsymbol{\nabla}\boldsymbol{\nabla}}{\varepsilon_1} \right) \frac{\mathrm{e}^{\mathrm{i}k_1 R}}{4\pi\varepsilon_0 R} \quad \text{where} \quad \boldsymbol{R} = \boldsymbol{r} - \boldsymbol{r}_0. \tag{5.5}$$

In the Green's function that describes the reflection from the interface, we will restrict the calculations to the transverse magnetic polarized waves, and thus can present it according to [Tom95; Spi18] in the following way

$$\boldsymbol{G}_\mathrm{R} = \frac{1}{2\varepsilon_0} \left(\frac{\omega}{c}\right)^2 \iint \frac{\mathrm{d}k_\mathrm{x}\mathrm{d}k_\mathrm{y}}{(2\pi)^2} \frac{r_\mathrm{TM}}{k_{\mathrm{z},1}} \mathrm{e}^{\mathrm{i}\boldsymbol{k}_\perp \cdot \boldsymbol{R}} \mathrm{e}^{-\mathrm{i}k_{\mathrm{z},1}(z+h)} \boldsymbol{e}^-_\mathrm{TM}(\boldsymbol{k}) \otimes \boldsymbol{e}^+_\mathrm{TM}(\boldsymbol{k}), \tag{5.6}$$

where r_TM is the Fresnel coefficient of the TM polarized reflection from (3.2) and

$$\boldsymbol{e}^\pm_\mathrm{TM} = \frac{k_{\mathrm{z},1}\boldsymbol{e}_\mathrm{y} \mp k_\mathrm{y}\boldsymbol{e}_\mathrm{z}}{\sqrt{|k_{\mathrm{z},1}|^2 + k_\mathrm{y}^2}} \tag{5.7}$$

are the basis vectors of a TM polarized wave with the z-component of the wave vector reading $k_{\mathrm{z},1} = \sqrt{(\omega/c)^2\varepsilon_1 - k_\perp^2}$. The electric field distribution that is resulting from (5.4) is shown in Figure 5.1 as a false colour image. In the left half of this figure a

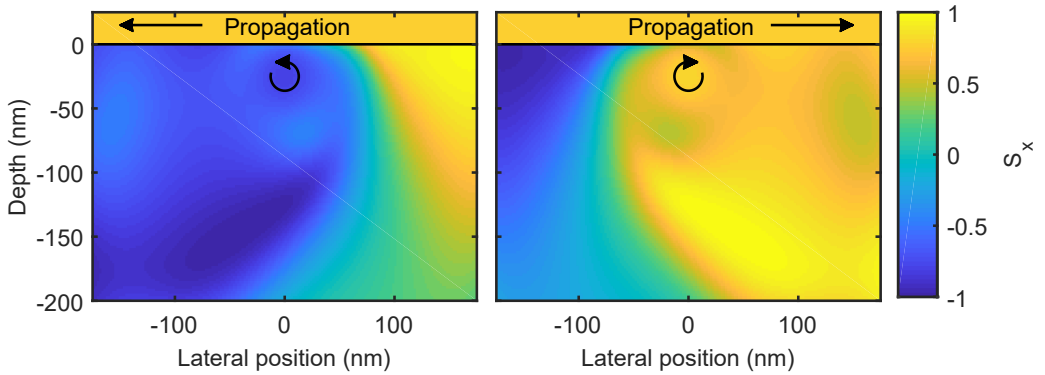

Figure 5.2: Transverse SAM of the electric field originating from the emission of a dipole. In the left panel a dipole with negative spin $S_x = -0.8$ is shown, while for the right panel $S_x = +0.8$ holds immediately at the dipole location $\boldsymbol{r}_0 = (0, 0, -25\,\mathrm{nm})^\top$. The dipole is placed inside (Cd,Mg)Te as surrounding medium with $\varepsilon_1 = 7.4$ in proximity to an interface, with gold as the second medium ($\varepsilon_2 = -19.6 + 1.2\mathrm{i}$). In the left panel where the emitter has $S_x < 0$ one can see that the left propagating surface waves prevail. The opposite behaviour is observed on the right where the dipole emission with $S_x > 0$ is preferentially propagating in the positive y-direction.

dipole with circular polarization degree $P_c = -1$ is located at the position indicated by the circular arrow. Already in this simple structure the dipole emission is not equally distributed in the lateral directions, but instead the dipole emits preferentially in the negative y-direction. Note especially that there is some intensity left at $y = -100\,\mathrm{nm}$ while there is none on the other side at $y = 100\,\mathrm{nm}$. The origin of this effect is the locking of the transverse SAM S_x of the emission to the evanescent surface wave that carries the same transverse spin. These surface waves are present near an interface that breaks the mirror symmetry, which in our case is the z-direction.

We can calculate this transverse spin angular momentum for the given electric field [Bli15b; Spi18]

$$S_x = \mathrm{i}\frac{[\boldsymbol{E} \times \boldsymbol{E}^*]_x}{|\boldsymbol{E}|^2} \tag{5.8}$$

and get a value of $S_x \approx -0.8$ immediately at the dipole location for the emitter with $P_c = -1$. One should note that the transverse SAM ranges from $-1 \leq S_x \leq 1$ with $|S_x| = 1$ representing an electric field fully circular in the xy plane. If we compare this directional emission with the opposite case presented in the right panel of Figure 5.1 where $P_c = +1$ and accordingly $S_x = +0.8$ at the dipole location, we can see the opposite behaviour. In this case the emission is preferentially coupling to the surface modes propagating into the positive y-direction. For a dipole in free space the transverse SAM would vanish rapidly with increasing distance to the dipole ($S_x \to 0$). As shown in Figure 5.2 this is not the case anymore in a symmetry

broken structure which gives rise to a non-zero transverse SAM even at larger dipole distances.

In other words, right-going evanescent waves have positive spin $S_x > 0$ while for the left-going waves $S_x < 0$ holds. This is one of the basic principles of the effect presented in Chapter 8. In the DMS structures studied there, the polarization of the emission can be effectively controlled by a magnetic field, due to the Giant Zeeman effect introduced in 4.1. In combination with a mirror symmetry broken structure this enables the spin-momentum locking of transverse SAM S_x and the propagation direction $\boldsymbol{k}$ in these structures, while the Giant Zeeman splitting couples S_x to the magnetic field B. We named the effect arising under these two conditions the transverse magnetic routing of light emission (TMRLE) and reported on it in [Spi18].

5.2 Transverse Spin of Surface Plasmon Polaritons

The surface plasmon polariton is a special case of an evanescent surface wave. We already saw the electric field distribution of such an SPP in Figure 3.3 propagating at the interface of gold and $Cd_{0.73}Mg_{0.27}Te$ at an energy of $E = \hbar\omega = 1.67\,\text{eV}$. Now we can also calculate its transverse SAM according to Eq. (5.8). In this case we get a transverse SAM $|S_x| = 0.89$ that is independent of the lateral position. The sign of the transverse SAM depends on the material in which the electric field is present, as it has opposite sign when comparing metal and (Cd,Mg)Te. Furthermore, for the wave propagating in the opposite direction, also S_x changes its sign.

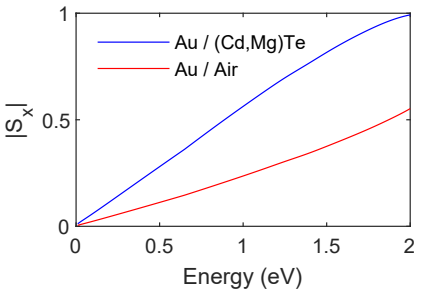

Figure 5.3: Transverse SAM $|S_x|$ versus energy of an SPP wave propagating either at the Au / (Cd,Mg)Te (blue line) or at the Au / Air interface (red line).

Here one can see an interesting difference with respect to other evanescent waves: The transverse spin angular momentum of surface plasmon polaritons is of the same magnitude in both semi-infinite materials, while this is usually not the case for an arbitrary surface mode. The transverse SAM of the surface plasmon polariton at the interface of gold and (Cd,Mg)Te is less than unity irrespective of the chosen energy value, as shown in Figure 5.3. At the interface of gold and air the transverse spin is even lower $S_x < 0.14$. Counter-intuitively at first, this suggests that a dipole emitter

is most efficiently routed close to an interface supporting SPP waves, if the dipole's transverse SAM is lower than the maximum value of ± 1 as well.

5.3 Establishing the Dipole Emission

As already stated in the introduction, the control over the propagation direction of light is required in many domains of modern optics [Ben11; Lod17]. With the spin-momentum locking of an emitter in proximity to the metal-dielectric interface, one prominent near-field approach for establishing directional emission was already introduced in this chapter. Now the question arises how to achieve the dipole emission with the necessary circular polarization in the yz-plane. In a first approach Rodríguez-Fortuño et al. [Rod13] introduced a SiO_2 based structure with a flat gold film on top. The gold film was interrupted by a single groove. The dipole emission was interchanged in their studies by light incident on this slit under nearly grazing incidence. They interpreted the incident light as a fake dipole with the polarization of the incident light representing the dipoles polarization. And indeed they already observed directional emission in this case in accordance with our considerations in Subsection 5.1. They could show that for linear polarized incident light two opposite SPP waves of equal intensity are excited, while circular polarized incident light excited only the left- or right-going SPP wave. In literature further similar approaches for establishing directional emission were presented. A dipole emitter in proximity to an optical waveguide for example also allows to observe directional emission [Mar15]. Instead of a dipole emitter again circular polarized light can be used which in this case is incident on a nanoparticle [Pet14].

Establishing the control over the propagation direction by the use of magnetic forces would be highly appealing for applications in magneto-optical storage, nanophotonic circuits and precision metrology [Tem10; Aki12; Arm13; Bos16]. In order to achieve this control in emission a dedicated tailoring of the structures is required. So far this has only been demonstrated in Faraday geometry for the emission of chiral objects, where directionality is established along the axis parallel to the magnetic field [Rik97]. Interestingly, in the transverse geometry where directionality is established perpendicular to the magnetic field no intensity effects have been reported yet, irrespective of the system studied here. In our studies we examine an improved structure in which the emission of excitons is considered as the dipole emitter. The selection rules and thus its polarization is controlled by a magnetic field via the Zeeman effect, enabling magnetically controlled directional emission.

5.4 Scattering Matrix Method

The numerical calculation with the Green's function approach like in Subsection 5.1 is the method of choice for the simulation of near-field emission in a simple smooth structure. In case of far-field calculations or for more elaborated structures with additional layers or a periodic metal film as described in Section 3.3 one usually prefers calculations based on the scattering matrix (S-matrix) method. This method is also used within this thesis for the calculation of photoluminescence (PL) and reflection spectra in the formulation introduced by Whittaker and Culshaw [Whi99]. The S-matrix characterizes the scattering of electromagnetic waves at a structure and to that end relates the intensities of the incoming (forward going) and the reflected (backward going) waves.

Part III

Experimental Methods

Chapter 6

Material Properties of the (Cd,Mn)Te / (Cd,Mg)Te Samples

All samples presented within this thesis are hybrid magneto-plasmonic semiconductor nanostructures similar to the one shown in Figure 6.1a. Based on a semi-insulating GaAs (100) substrate, the $Cd_{.73}Mg_{.27}Te$ buffer layer ($E_g \approx 2.1\,\text{eV}$ at 2 K) was grown by molecular beam epitaxy (MBE)[1]. On top of this layer the 10 nm thick $Cd_{.974}Mn_{.026}Te$ diluted-magnetic-semiconductor QW layer ($E_g = 1.656\,\text{eV}$ at 2 K) is located. A $Cd_{.73}Mg_{.27}Te$ cap layer covers the QW both as a spacer between the QW layer and the perforated gold film on the surface and as an electronic barrier for the excitons in the QW.

These four layers – substrate, buffer, QW and cap – form the semiconductor structure which is later referred to as the *bare semiconductor structure*, i.e. with no further surface structuring (Sample 1b, 2b and 3b). For the plasmonic structures, $200 \times 200\,\mu\text{m}^2$ gold gratings were patterned on top of the semiconductor structure (Sample 1, 2 and 3). The so-called 'lift-off'-processing was done by first applying a photoresist layer on top of the semiconductor. An inverse mask was inscribed into the photoresist layer by electron beam lithography.After this development step a photographic developer was used in order to remove all the photoresist in those areas were gold is supposed to stick to the dielectric. Immediately before the evaporation of gold, the sample was subject to a short plasma treatment for descumming directly in the metal evaporation chamber. A continuous gold layer is brought onto the sample by thermal evaporation and covers both the photoresist and resist-free areas on the sample. In this step no metal is used to promote the adhesion of the gold layer. The residual photoresist is dissolved in an acetone bath subsequently. The gold deposited on top of the photoresist is carried off with it in this step. Only the gold

[1] MBE is an epitaxial process that paved the way to the growth of high-quality structures with well-defined layer arrangement and precisions ultimately down to a single layer of atoms. Due to this accurate precision the development of structures like quantum wells or even quantum dots is possible. [Hen13]

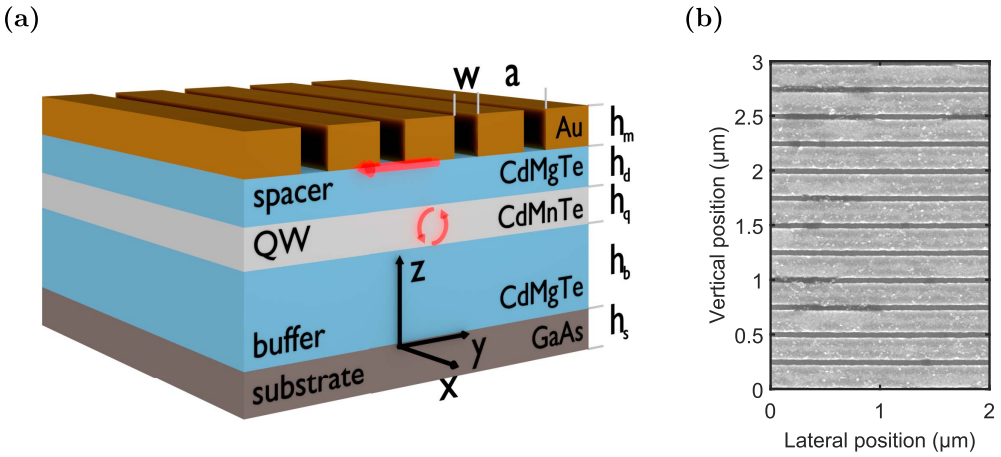

Figure 6.1: (a) Schematic sketch of the hybrid magneto-plasmonic semiconductor nanostructure. The following geometrical parameters are shown: grating period a, slit width w, grating thickness h_{m}, spacer thickness h_{d}, QW width h_{q}, buffer thickness h_{b} and substrate thickness h_{s}. The corresponding values for each sample are listed in Table 6.1. **(b)** Image of the plasmonic grating on Sample 2 acquired by scanning electron microscopy (SEM). Here the grating period is $a = 250\,\mathrm{nm}$, the slit width is $w = 50\,\mathrm{nm}$ and the thickness of the Au layer is about $h_{\mathrm{m}} = 45\,\mathrm{nm}$. Figure adapted with permission from Reference [Spi18].

which is in direct contact with the semiconductor surface remains. The samples were subsequently imaged via scanning electron microscopy (SEM) in order to validate the grating period $a = 250\,\mathrm{nm}$ and slit width $w = 45\,\mathrm{nm}$ as shown in Figure 6.1b.

The grating parameters were chosen in order to tune the first order far-field emission of the SPPs at the semiconductor / gold interface close to the exciton frequency $\omega_{\mathrm{SPP}} \approx \omega_{\mathrm{X}}$ especially at small emission angles $\theta < 24°$, which are accessible within this experiment (see also Chapter 7). The reflectivity and photoluminescence spectra shown exemplary in Figure 6.2 for Sample 1 with a 250 nm period grating structure confirm the proper choice of grating parameters. Figure 6.2a shows the p-polarized angle resolved reflectivity spectra at low temperatures of $T = 10\,\mathrm{K}$ both from experiment (left) and scattering matrix simulation (right). Both spectra were calculated as follows

$$R(\omega,\theta) = \frac{I_{\mathrm{Grating}}(\omega,\theta) - I_{\mathrm{Background}}(\omega,\theta)}{I_{\mathrm{Film}}(\omega,\theta) - I_{\mathrm{Background}}(\omega,\theta)}, \tag{6.1}$$

where $I_j(\omega,\theta)$ is the angle resolved intensity spectrum of the plasmonic grating coupler ($j = \mathrm{Grating}$), the flat unpatterned gold film ($j = \mathrm{Film}$) or the background intensity with blocked white light source ($j = \mathrm{Background}$). The simulated spectra are

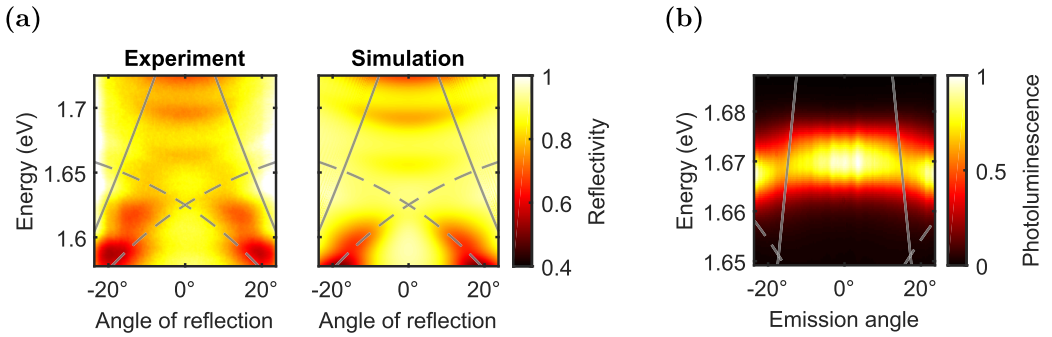

Figure 6.2: Reflectivity and photoluminescence spectra of Sample 1. **(a)** False colour plot of the experimental (left) and simulated (right) angle resolved reflectivity spectra. The solid lines show the dispersion of the Wood's anomaly as calculated from Eq. (3.13). The dashed lines follow the (Cd,Mg)Te / gold SPP dispersion as defined by the maximum of absorption in simulations with infinite buffer thickness. Interference fringes which originate from the finite buffer thickness are suppressed in this approximation. The spectra are taken at $T = 10\,\mathrm{K}$. **(b)** Contour plot of the angle resolved PL spectrum of the QW emission. A laser with a photon energy of 2.25 eV was used for off-resonant excitation. Temperature and notation for lines representing the SPP dispersion are consistent with (a).

calculated as described in Section 5.4. From these reflectivity spectra the dispersion of the surface plasmon polariton resonances is determined.

Grey lines in Figure 6.2 represent the dispersion of the Wood's anomaly (solid line) and the SPP at the (Cd,Mg)Te / gold interface (dashed line) respectively. The features spectral position strongly depends on the angle of incidence. If spectra are taken next to the grating i.e. on the bare QW structure or if the s-polarized spectra are detected, these features are absent. Consistently in both experiment and simulation the broad dips in reflectivity at energies of about 1.6 eV can be attributed to the (Cd,Mg)Te / gold SPP, whereas the Wood's anomaly follows the contour line at about constant 90 % reflectivity. While the position of the Wood's anomaly is calculated according to Eq. (3.13), the dispersion of the (Cd,Mg)Te / gold resonance is following the maximum of absorption in simulations with infinite buffer thickness (not shown here). The main advantage of simulations with infinite buffer thickness is the absence of the thin film interference fringes. These are present in the real structure as seen distinctly in the reflection spectra by the fast oscillations with a period of about 25 meV. Both experiment and simulation exhibit the same features and show good agreement.

In Figure 6.2b a false colour plot of the angle resolved PL spectrum $I(\hbar\omega, \theta)$ at $T = 10\,\mathrm{K}$ is shown. The QW exciton emission band is centred at 1.67 eV with a weak dependence on the emission angle. Due to the narrow spectral width at half

maximum of 10 meV, as compared to a white light source, also the spectral range which may be observed in the TMRLE experiments is limited to energies from 1.65 eV to 1.69 eV.

The three studied semiconductor structures differ mainly in two points. On the one hand Sample 1 has a larger cap layer with $h_\mathrm{d} = 250\,\mathrm{nm}$ thickness as compared to Sample 2 and 3 with a small cap layer of about 30 nm. On the other hand Sample 2 is modulation doped, which increases the carrier mobility in this sample. This is realized by a 3.5 nm thick modulation doped layer in the buffer with 40 nm distance to the QW. A second 2.5 nm thick modulation doped layer is located in the spacer with 20 nm distance to the QW. On all (Cd,Mn)Te samples, a 5.3 nm thin ZnTe layer was grown between the substrate and buffer layer to reduce the lattice mismatch (not shown in table/figure). The further relevant structure parameters are listed in Table 6.1. Additionally, Sample 2 was used for another set of grating structures with different grating periods a varied between 200 nm to 320 nm in steps of 10 nm. Due to the large number of gratings, their size was reduced to $50 \times 50\,\mu\mathrm{m}^2$.

Table 6.1: Geometrical parameters of the (Cd,Mn)Te / (Cd,Mg)Te DMS QW structures. The samples are either manufactured with a plasmonic nanostructure on top (Sample 1, 2 and 3) or just the bare semiconductor structure is studied (Sample 1b, 2b and 3b).

Parameter		Sample					
Variable	Meaning	1	1b	2	2b	3	3b
a	grating period	250 nm	–	250 nm	–	560 nm	–
w	slit width	50 nm	–	50 nm	–	50 nm	–
h_m	grating thickness	45 nm	–	45 nm	–	45 nm	–
h_d	spacer thickness	250 nm		32 nm		30 nm	
h_q	QW width	10 nm		10 nm		10 nm	
h_b	buffer thickness	3.25 µm		5.62 µm		3.05 µm	
h_s	substrate thickness	400 µm		400 µm		400 µm	

Chapter 7

Experimental Setups

In this chapter three different optical setups are presented, which were used in this thesis. First, the magneto-photoluminescence setup is described where a magnetic field in Faraday geometry of up to 5 T was used in order to determine the concentration of Mn^{2+} ions in the studied DMS structures. Next, a setup which allows to apply a high magnetic field in Voigt geometry and detect its influence on either the reflected or emitted light's intensity at a fixed angle follows. Finally, the Fourier spectroscopy setup is introduced in the last section enabling the detection of fine-grained angular resolved spectra in a single shot, where the magnetic field strength on the other hand is one order of magnitude smaller as compared to the fixed angle setups.

7.1 Magneto-Photoluminescence Setup for the Determination of the Mn^{2+} Concentration

Magneto-photoluminescence measurements of the bare QW structure allow the evaluation of giant Zeeman splitting in the samples discussed in Section 6. All measurements using this setup were performed at the Ioffe Institute in Saint Petersburg during a research stay in the laboratory of Victor F. Sapega. A He-Ne laser with photon energy of 1.96 eV was used to populate the QW with excitons, while the structure was mounted in the variable temperature insert of a liquid helium bath cryostat at $T = 2\,\mathrm{K}$. Superconducting coils allowed the application of up to 5 T magnetic field in Faraday geometry. The emitted light was spectrally dispersed by a double monochromator and detected in circular σ^+ and σ^- polarization by a photomultiplier connected to a photon counting unit. Due to the strong polarization degree already in moderate magnetic fields (e.g. 98 % at about $\approx 200\,\mathrm{mT}$), only the energetically lower σ^+ polarized exciton transition was observable while the emission of the higher σ^- polarized energy transition has vanished.

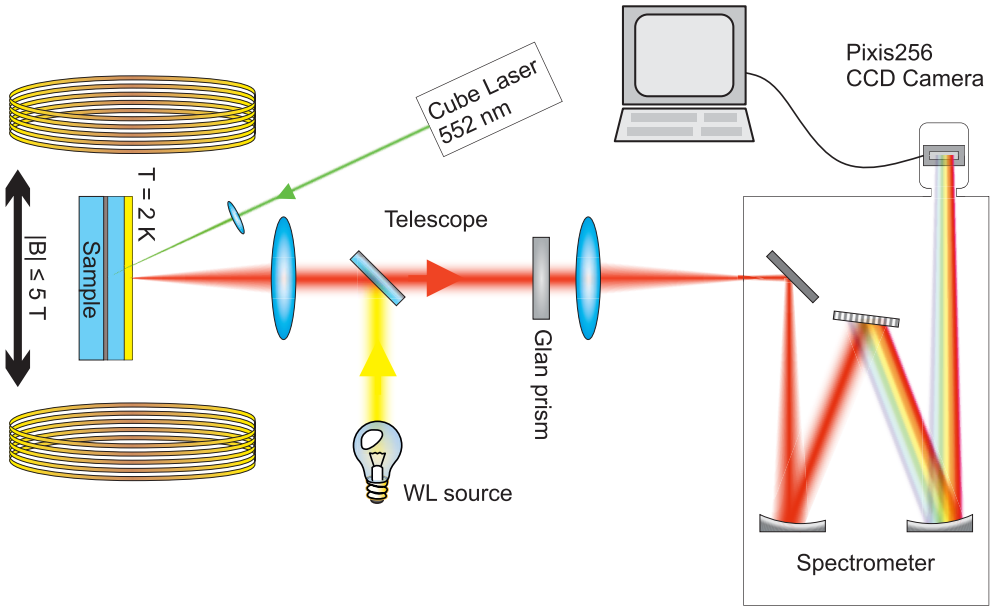

Figure 7.1: Scheme of the high magnetic field spectroscopy setup (top view). For resonant excitation a tungsten halogen lamp (light bulb and yellow beam) and for non-resonant excitation a 552 nm continuous wave laser (green) was used. The emitted light shown in red is linearly p-polarized by a Glan-Thompson prism. A telescope consisting out of two achromatic doublet lenses maps the Fourier plane onto the spectrometer slit. Here the light is spectrally dispersed before hitting the CCD camera. A long-pass filter can be used to block the scattered excitation laser light.

7.2 Fixed Angle and High Magnetic Field Setup

This setup was designed to discover the maximum strength of the TMRLE (discussed in Chapter 8) and the TMOKE (Chapter 9). By saturating the Mn^{2+} magnetization in high magnetic fields of up to $|B| = 5\,\mathrm{T}$ and at a low temperature of about $T = 1.6\,\mathrm{K}$ also the effect strengths of TMRLE and TMOKE are expected to approach their maximum value, as both effects are induced by this Mn^{2+} magnetization. The corresponding setup is illustrated in Figure 7.1 and can be used in two different experimental schemes.

Resonant excitation In the case of resonant excitation, a tungsten halogen lamp (*Spectral products* ASB-W-030) was used as a white light (WL) source. In the scheme it is represented by the light bulb and the yellow light beam. This thermal light source possesses a flat spectrum and is emitting over a broad range of wavelengths

from 300 nm to 2600 nm and thus is particularly suitable for reflectivity or TMOKE measurements. The light bulb is surrounded by a metal shielding which is constantly cooled by a fan in order to keep the lamp at almost constant temperature. On one side it has an opening with a lens allowing the emitted light to exit the shielding while being focused onto the aperture of a fibre (not shown in the figure). On the other side of the fibre the light is out-coupled and collimated by an air-spaced doublet collimator (*ThorLabs* F810SMA-635). A single $f = 200\,\mathrm{mm}$ achromatic lens was used both to focus the whitelight onto the sample and to collimate the reflected light. The incoming and emerging light beams are separated spatially as shown in Figure 7.2a. The WL spot size is limited by a diaphragm before the light is passing through the top of the lens, resulting in an angle of reflection of $\theta = (5.0 \pm 0.3)^\circ$ under which the reflected light is reaching the lower half of the lens.

Non-resonant excitation For the non-resonant measurements, a 552 nm continuous wave laser (*Coherent* 1230938) was used. It is represented in the scheme by the white rectangle emitting a green laser beam. The 2.25 eV laser is mounted to a heat sink in order to dissipate the generated heat and keep the laser at constant temperature. No additional cooling is required as only small excitation powers are necessary for the experiments. Furthermore a laser intensity stabilizer (*BEOC* LPC) was used in this setup to keep the laser power constant at about 300 µW during the measurement at different magnetic field strength. The laser light was focused onto the sample, in order to excite excitons in the QW, while the emission was collimated by a different achromatic doublet lens as shown in Figure 7.2b. In contrast to the case of reflection where the angle of reflection is limited by the aperture of the cryostat windows, the emission angle can be larger as the sample itself can be rotated. In our experiments this angle of emission is fixed by gluing the sample on a 15° wedge. The resulting emission angle of $(15 \pm 5)^\circ$ was chosen wide-ranged as compared to the resonant case in order to increase the detected intensity. This choice is justified by the weak angle dependence in this range as present later in Subsection 8.2.4 for the angle resolved TMRLE measurements.

In both cases the sample was mounted inside the variable temperature insert of a bath cryostat at $T = 1.6\,\mathrm{K}$. Superconducting coils allowed transverse magnetic fields of up to $B = 5\,\mathrm{T}$ to be applied. The collimated light is subsequently linearly p- or s-polarized by the combination of a half-wave plate mounted in a computer controllable rotary stage (*OWIS* 43.065.356C) and a Glan-Taylor polarizer. An achromatic doublet lens focuses the light onto the spectrometer slit before it is spectrally dispersed and detected by a two-dimensional charge-coupled device (CCD) matrix detector.

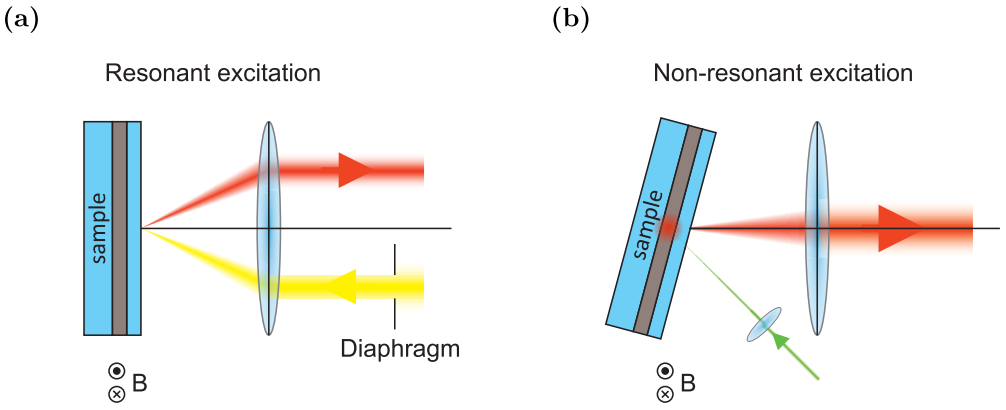

Figure 7.2: Scheme of the high magnetic field spectroscopy setup (side view). **(a)** The case of resonant excitation with the WL represented by the lower yellow beam and the reflected light as the red upper beam. Both are focused / collimated by the same $f = 200\,\mathrm{mm}$ achromatic doublet lens. A diaphragm is limiting the angle of reflection to $\theta = (5.0 \pm 0.3)°$. **(b)** The non-resonant excitation case. In contrast to the resonant case, the emission angle was fixed by gluing the sample on a 15° wedge. The emission was collimated by a $d = 25.4\,\mathrm{mm}$, $f = 300\,\mathrm{mm}$ achromatic doublet lens resulting in $\theta = (15 \pm 3)°$.

As the effects to be determined are intensity effects, they are intrinsically sensitive to changes in the excitation intensity. As a consequence in the non-resonant case the excitation laser light was stabilized as stated before. In the resonant case the situation is more challenging, as a laser intensity stabilizer is not designed for broadband light sources. In order to keep the effects of a potential intensity drift as low as possible, the linear p- and s-polarized spectra where measured in an alternating sequence. As in s-polarization the magnetic field dependent effects are not present in Voigt magnetic field, in the resonant case the spectrally-integrated s-polarized intensity was used for normalization of the p-polarized spectra

$$\tilde{I}_\mathrm{p}(\lambda) = \frac{I_\mathrm{p}(\lambda)}{\sum_\lambda I_\mathrm{s}(\lambda)}. \tag{7.1}$$

7.3 Angular Resolved Optical Spectroscopy Setup

In this section the setup for angular resolved imaging is presented, which is shown in Figure 7.3. The optical components and their function within the setup will be discussed before their position within the setup is calculated explicitly. This type of experimental setup is also called Fourier imaging spectroscopy setup as it is imaging the reciprocal k space. It allows not only to acquire a broad spectral dependence in a single acquisition but also the angular dependence at the same time.

Excitation of the sample

Depending on the type of measurement – reflection or photoluminescence – two types of light sources were used. As already stated in Section 7.2, in the case of resonant excitation a tungsten halogen white light lamp is utilized, emitting over a broad range of wavelengths. In the non-resonant case on the other hand a green 2.25 eV laser was used for excitation of excitons in the QW of the sample structure.

The incoming light is passing a 50:50 non-polarizing beam splitter cube (*Thorlabs* CM1-BS014) anti-reflection coated for ideal performance in the 700 nm to 1100 nm wavelength range, which corresponds to the desired wavelength range for the samples described in Section 6. Within the specified wavelength range approximately the same intensity of light is transmitted or orthogonally reflected independently of its polarization. The reflected light can be used for monitoring the incident light intensity during the measurement. The polarization of the transmitted light on the other hand is subsequently set by an achromatic calcite Glan-Taylor polarizer (*Dayoptics* PGT7015) and an achromatic half-wave plate to be either in p- or s-polarization. As most effects of interest in this thesis (e.g. TMOKE) are manifested only in p-polarization, this is also the default polarization which the optics let pass if not stated otherwise. By using a half-wave plate for setting the beams polarization, a beam path misalignment induced by the beam offset at different Glan orientations is avoided.

The excitation light is now focused onto the sample by a microscope objective (*Mitutoyo* 378-824-5) with long working distance. The light is focused into a spot of about 20 µm diameter in the non-resonant case and 200 µm diameter in the resonant case. In the non-resonant case the excitation density was kept well below 50 W/cm^2 in order to avoid heating of the Mn system. The infinity corrected microscope objective (MO) with 20x magnification is optimized for a wide spectral range of 480 nm to 1800 nm. The numerical aperture of 0.4 defines the maximum angle $\theta_{\max} = \arcsin(0.4) \approx 23.58°$ under which light is incident on the sample or collected from it. With its 20 mm working distance, it can be used even for investigating samples at cryogenic temperatures, as described in the following.

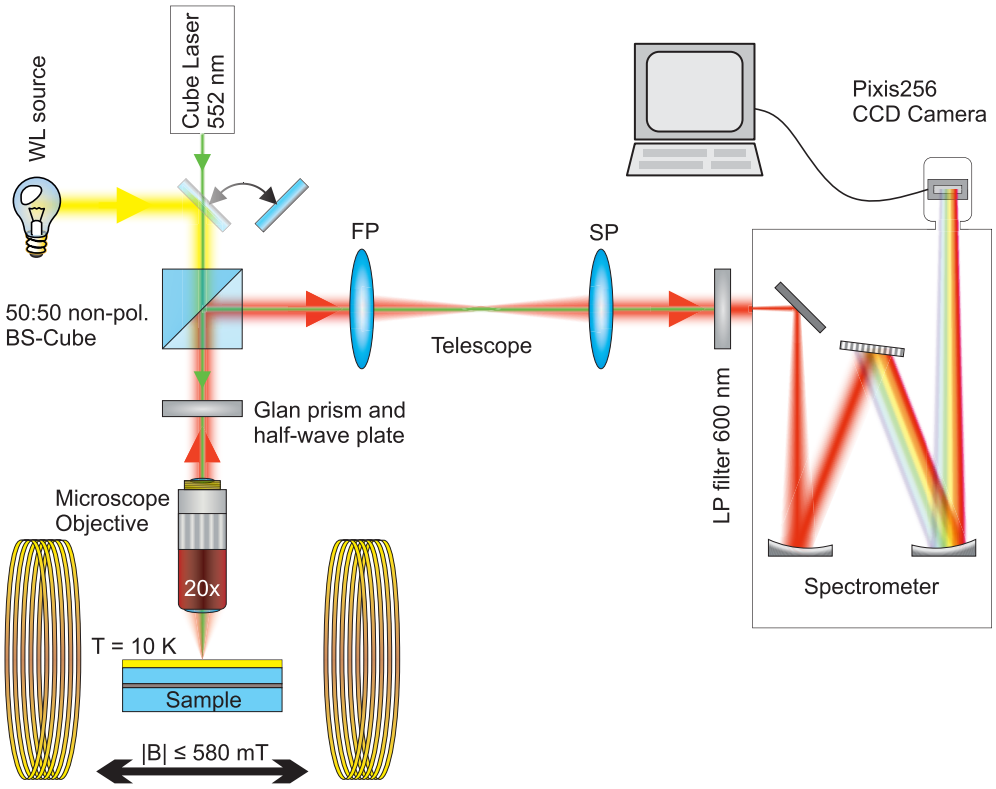

Figure 7.3: Scheme of the angular resolved spectroscopy setup (top view). For excitation a 552 nm continuous wave laser (green beam) or white light source (yellow beam) can be used. The emitted / reflected light (red beam) is first polarized and then reflected inside a beam-splitter cube. A telescope consisting of two achromatic doublet lenses maps the Fourier plane onto the spectrometer slit. Here the light is spectrally dispersed before hitting the CCD camera. A long-pass filter can be used to block the excitation laser light. By removing the FP lens, the setup is switched to spacial resolution.

Flow cryostat and magnetic field

The experimental setup was optimized for the use with a helium flow cryostat (*Oxford instruments* MicrostatHe-R) in which the sample is kept in vacuum during measurements. Within the flow cryostat, the sample is usually glued onto a copper sample holder by silver conductive paint, because of its good thermal conductivity. A continuous flow of liquid helium ideally evaporating at the heat exchanger of the flow cryostat cools the cold finger, which is connected to the sample holder. The temperature is measured at the heat exchanger, which was kept constant at 5 K resulting in 10 K at the sample if not stated otherwise. Stabilization of the temperature was achieved by combining a heater with a proportional-integral-derivative (PID) feedback controller (*Oxford instruments* MercuryiTC).

The flow cryostat is fixed between the two copper coils of a water cooled electro magnet (*GMW Associates* 5403EG) providing up to 700 mT of transverse magnetic field $\boldsymbol{B} \parallel \boldsymbol{x}$, depending on the distance of the steel ferrites. For the maximum magnetic field strength a ferrite distance of 40 mm is necessary, leaving not enough space for sample movement. Therefore the ferrite distance had to be increased to 50 mm resulting in a maximum magnetic field strength of $B_{\mathrm{max}} = 580\,\mathrm{mT}$ at the highest applicable coil current of 40 A. The coil current is limited by the utilized bipolar magnet power supply (*Kepco* BOP20-50MG) which was controlled automatically by the measurement program in LabView.

Superior stability is the most crucial and challenging point in this experiment. When changing the magnetic field strength, magnetic components of the setup may start to interfere with each other and even in the non-magnetic components a magnetic field might be induced. Thus the microscope objective is mounted in a cage specially designed for this experiment providing high stability. This is achieved by fixing the objective not only from the lower side, but rotational symmetric from four sides along its optical axis. In addition, the microscope objective holder can only be moved along the optical axis in order to move it roughly into focus, while preventing it from moving within magnetic field.

On most samples there is a specific area which shall be studied, which makes it necessary to move the sample not only into focus but in all three dimensions and consequently the whole flow cryostat. As stability is the main concern, a three dimensional crossed-roller bearing stage (3x *Newport* M-426) is used. This type of stage is highly stable and each stage can be fixed on a certain position, restricting further movement along this axis.

Detection of collected light

The light which was either reflected (resonant case) or emitted (non-resonant case) from the sample is collected and collimated by the same MO in back-scattering geometry. At a distance of twice the focal length of the MO $2f = 20\,\mathrm{mm}$ with respect to the sample the Fourier plane is located. Here, the horizontal direction corresponds to the light's momentum along the magnetic field direction k_{x} while in the vertical direction the momentum projection perpendicular to the magnetic field but within the sample plane k_{y} is present.

Subsequently the light passes the polarization optics once again resulting in the detection of the respective polarization only. When impinging on the beam splitter cube, this time the deflected light is of interest. A telescope consisting of a pair of achromatic doublet lenses ($f_{\mathrm{FP}} = 400\,\mathrm{nm}$ and $f_{\mathrm{SP}} = 300\,\mathrm{nm}$) maps the Fourier plane onto the spectrometer slit. In the non-resonant measurements additionally a 600 nm

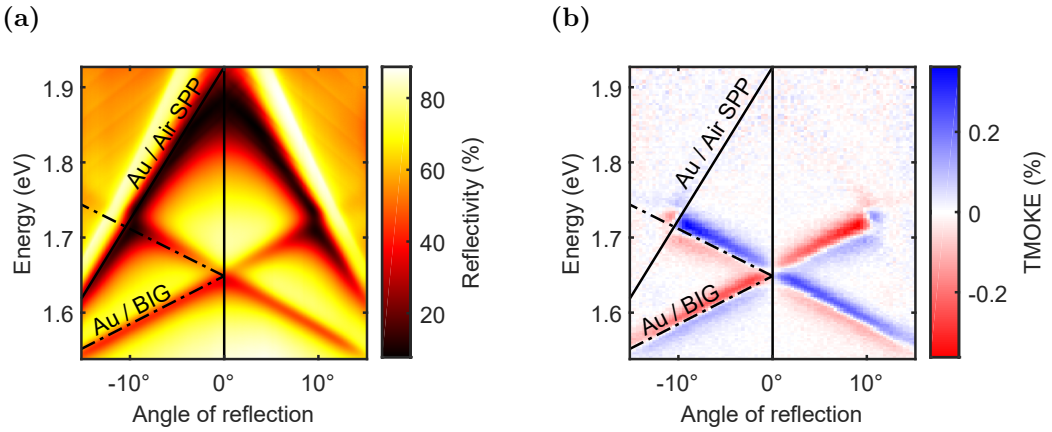

Figure 7.4: (a) The first measurement taken on the Fourier imaging setup already shows its capabilities and richness of detail. Shown here is a false colour plot of the angular resolved reflection spectrum of the bismuth iron garnet (BIG) plasmonic hybrid structure reported on in Reference [Poh13]. The surface plasmon polariton resonances of the plasmon propagating on the gold / air interface is distinctly observed here (solid line) as well as the plasmon on the gold / BIG interface (dash-dotted line). The spectra are taken at room temperature on both the gold grating and a flat gold film for normalization. **(b)** False colour plot of the angular and spectrally resolved transverse magneto-optically Kerr effect in reflection. The TMOKE was calculated according to Eq. (4.11), representing the relative change of reflected intensity when applying a transverse magnetic field $B \approx 50\,\mathrm{mT}$.

long-pass filter is used in front of the spectrometer to suppress the stray light from the excitation laser.

The usually 150 µm wide opened spectrometer slit confines the light in horizontal direction, thus ideally only the $k_x = 0$ light passes into the single imaging monochromator (*Acton* SP2500i). Herein the light is spectrally dispersed in horizontal direction (6.4 nm/mm), while in vertical direction the angular k_y information is stored. Finally the light is detected by a charge coupled device camera (*Princeton Instruments* PIXIS 256) with 256×1024 pixels in vertical and horizontal direction, respectively. Each pixel has a size of $26 \times 26\,\mu\mathrm{m}^2$ resulting in a total size of $6.656 \times 26.624\,\mathrm{mm}^2$. Overall, this results in a spectral resolution of $\Delta\lambda \leq 0.6\,\mathrm{nm}$ and an angular resolution of $\Delta\theta \leq 0.5°$.

Comparison of Fourier imaging spectroscopy and regular fixed angle spectroscopy

The first measurement taken on this setup, at that time still with a slightly different configuration of optical components, is shown in Figure 7.4a. Here the optical parameters were $f_{\mathrm{MO}} = 20\,\mathrm{mm}$, $f_{\mathrm{FP}} = 300\,\mathrm{mm}$, $f_{\mathrm{SP}} = 400\,\mathrm{mm}$ and a different CCD

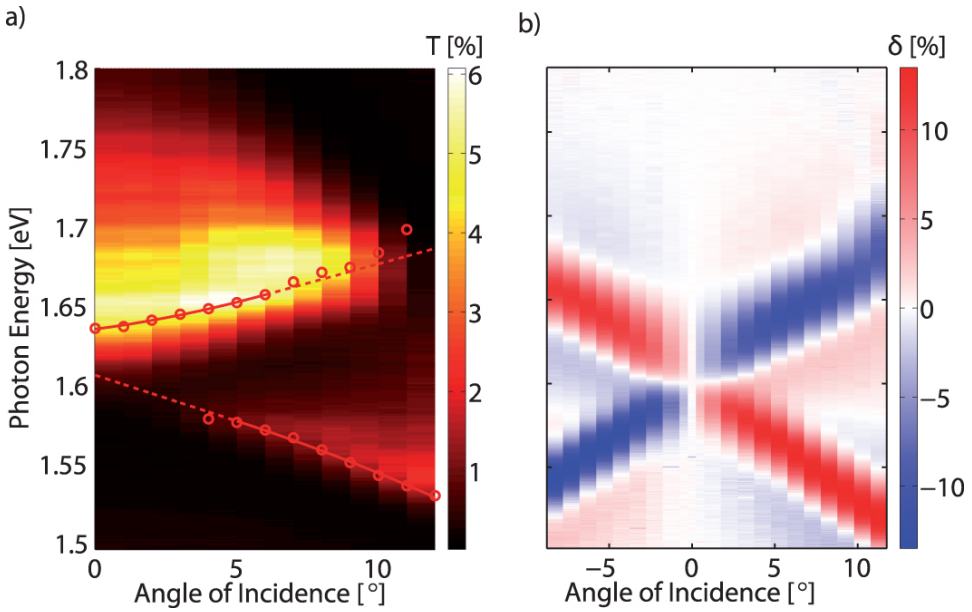

Figure 7.5: Measured angle dependence of the transmitted light spectrum of a bismuth iron garnet plasmonic hybrid structure between $\theta = 0°$ and 12° in steps of 1° without applied magnetic field. Open circles show the position of the Fano resonances. The dashed lines are meant as guide to the eye. (b) Measured angle dependence of the TMOKE in transmission with an applied external magnetic field of $B \approx 80\,\mathrm{mT}$. For symmetry reasons the effect vanishes for normal incidence and reverses sign when the angle of reflection is reversed. For angles $\theta \geq 4°$ a remarkably high value of $\delta = 13\,\%$ is reached. Figure reprinted and caption adapted with permission from Reference [Poh13].

camera was used with $8 \times 26.8\,\mathrm{mm}^2$ size split into 400×1340 pixels. In this measurement the angular resolved reflection spectrum is shown for the bismuth iron garnet (BIG) plasmonic structure, which was also studied by Pohl et al. [Poh13]. The surface plasmon polariton resonances at the gold and air interface (solid line) and at the gold / BIG interface (dash-dotted line) are clearly visible here as strong dips in the reflectivity. For calculation of the reflectivity, spectra on the plasmonic grating and on a flat gold film were taken and the latter one used for normalization.

In Figure 7.4b on the other hand the relative change in reflected intensity is shown when applying a transverse magnetic field of $B \approx 50\,\mathrm{mT}$, calculated as shown in Eq. (4.11). One can see strong TMOKE of $\delta = 0.3\,\%$ in reflection at the resonance of surface plasmon polaritons propagating at the interface of gold and the magnetic BIG layer. As expected, at the interface of gold and air on the other hand no TMOKE is observed, due to the relatively large magnetic layer distance. The Fourier imaging spectroscopy setup allows to resolve these features in reflectivity and TMOKE spectra with much more detail as compared to the measurements taken previously. For comparison in Figure 7.5 similar measurements on the same structure are shown,

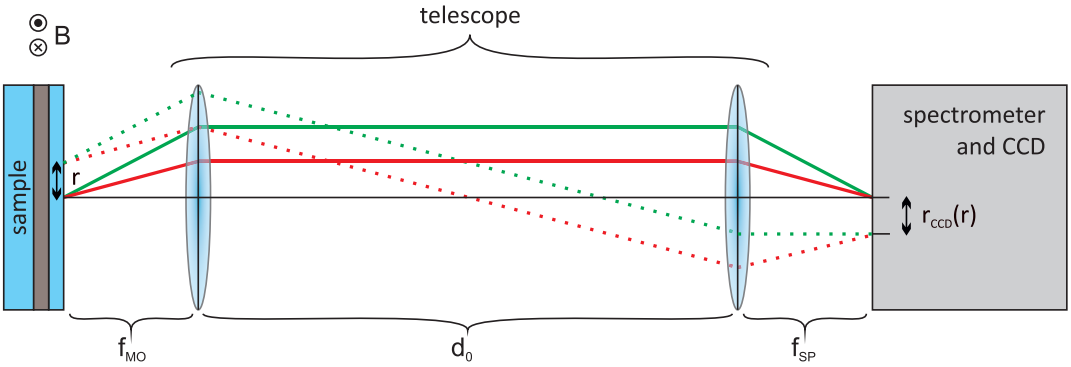

Figure 7.6: Scheme of a regular spacial resolved spectroscopy setup (side view). The light emerging from the sample is collimated by a microscope objective (MO) before being focused onto the slit of the spectrometer by the lens SP resulting in a spacial image of the sample. Thus the light's position on the CCD camera depends only on the position from which it originates but not on its angle (see solid / dotted lines in red / green).

reprinted from Reference [Poh13]. Here the transmitted light spectrum taken at different angles of sample rotation – and thus different angles of incidence – is shown on the left. On the right the corresponding values of TMOKE are presented.

As one can see, due to the 1° steps in angle of reflection the resolution of the measurement is worse by about one order of magnitude as compared to the angular resolution in the measurement shown in Figure 7.4. Another advantage of the setup designed within the scope of this thesis is the fixed transverse magnetic field direction. As mentioned before, in the prior setup the sample itself was rotated to change the light's angle of reflection, resulting in a potentially unwanted slight admixture of the Faraday magnetic field component. This is not the case in this setup as the magnetic field direction is always in-plane of the analysed structure. The main feature of this setup is its ability to take the full angular resolved spectrum in a single shot, with no further adjustments during the measurement process. At the same time this is also the main disadvantage, as you can not simply switch to a fixed angle measurement. Furthermore taking the full angular resolved spectrum takes a longer time than a single measurement at a fixed angle due to the decreased light intensity when distributed over the angular range.

Optical Beam Path Adjustment

Until now, only the optical components have been discussed, but not their specific position within the optical beam path. The experimental details and the adjustment procedure is described in this paragraph, based on the paraxial approximation.

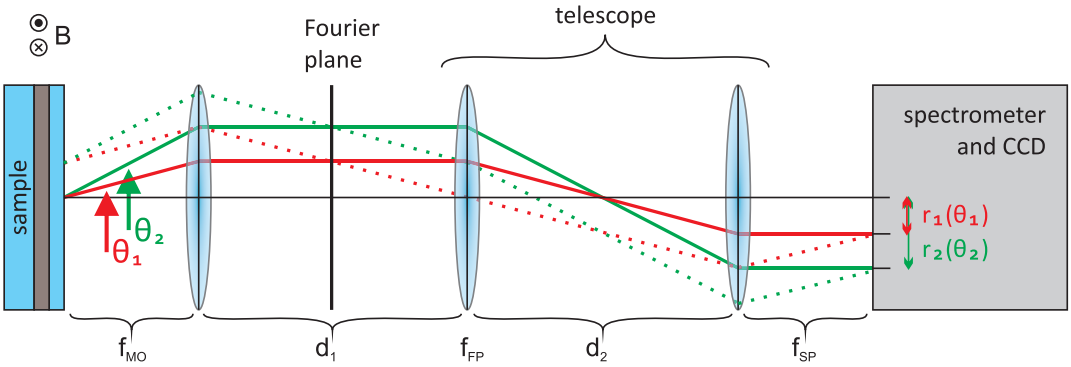

Figure 7.7: Scheme of the angular resolved spectroscopy setup (side view). In $2f_{\mathrm{MO}}$ distance from the sample the Fourier plane is located. Here, the vertical position of the light when incident on the CCD is only depending on its angle of reflection θ. By adding an additional lens (FP) the Fourier plane is mapped onto the spectrometer slit in combination with the already aligned SP lens. For $d_1 = f_{\mathrm{MO}} + f_{\mathrm{FP}}$ the position on the CCD depends only on the emission angle, i.e. not on the sample position (see solid / dotted lines in red / green).

When spatially imaging the light emerging from the sample the situation is as simple as shown in Figure 7.6. First, the sample is positioned in the focus of the microscope objective with focal length $f_{\mathrm{MO}} = 10\,\mathrm{mm}$ (not to be confused with the working distance). The light emerging from the sample around the optical axis is collimated by the MO regardless of its angle (red / green solid lines). If the light on the other hand is emerging from a different position within the field of view, e.g. in a distance of r from the optical axis, it is not collimated. In order to project the spacial image of the sample onto the CCD, an achromatic doublet lens (SP) with focal length $f_{\mathrm{SP}} = 300\,\mathrm{nm}$ is used, placed within its focal length distance afar from the spectrometer slit. Thus according to the ray transfer matrix analysis the resulting size on the CCD and the corresponding incidence angle are

$$\begin{aligned} r_{\mathrm{CCD}}(r,\theta) &= -\frac{f_{\mathrm{SP}}}{f_{\mathrm{MO}}} r \quad \text{and} \\ \theta_{\mathrm{CCD}}(r,\theta) &= -\frac{f_{\mathrm{MO}}}{f_{\mathrm{SP}}}\theta - \frac{f_{\mathrm{MO}} + f_{\mathrm{SP}} - d_0}{f_{\mathrm{MO}} f_{\mathrm{SP}}} r. \end{aligned} \tag{7.2}$$

As expected, the position on the CCD depends only on the position on the structure and not on the respective angle. Additionally for a distance between the MO and SP lens of $d_0 = f_{\mathrm{MO}} + f_{\mathrm{SP}}$ the incidence angle on the CCD does not depend on the sample position. For the given optics a magnification factor of $\frac{f_{\mathrm{SP}}}{f_{\mathrm{MO}}} = 30$ is present.

In order to measure the reciprocal space though, the vertical position on the CCD should ideally depend only on the angle θ. After both the MO and SP lens are in

place, this can be achieved by inserting one additional achromatic doublet lens (FP) in between the MO and the SP lens, as shown in Figure 7.7. This lens has a focal length of $f_{\mathrm{FP}} = 400\,\mathrm{mm}$ in our experiment. When calculating the size and angle on the CCD again for this more complex case of a three lens setup, this results in

$$\begin{aligned} r_{\mathrm{CCD}}(r,\theta) &= -\kappa_0\theta - \kappa_1 r \quad \text{and} \\ \theta_{\mathrm{CCD}}(r,\theta) &= -\kappa_2\theta + \frac{1-\kappa_1\kappa_2}{\kappa_0} r, \end{aligned} \tag{7.3}$$

with the variables

$$\begin{aligned} \kappa_0 &= \frac{f_{\mathrm{SP}} f_{\mathrm{MO}}}{f_{\mathrm{FP}}}, \\ \kappa_1 &= \frac{f_{\mathrm{SP}}}{f_{\mathrm{FP}} f_{\mathrm{MO}}}(f_{\mathrm{FP}} + f_{\mathrm{MO}} - d_1) \quad \text{and} \\ \kappa_2 &= \frac{f_{\mathrm{MO}}}{f_{\mathrm{FP}} f_{\mathrm{SP}}}(f_{\mathrm{FP}} + f_{\mathrm{SP}} - d_2). \end{aligned} \tag{7.4}$$

As one can see, if the distance between the MO and the FP lens is chosen randomly, the image on the CCD does depend both on the position on the sample r and the emission / reflection angle θ which would lead to a distorted image of the reciprocal space. This can easily be avoided for a distance between the MO and FP lens of $d_1 = f_{\mathrm{MO}} + f_{\mathrm{FP}} = 410\,\mathrm{mm}$ resulting in $\kappa_1 = 0$ and thus

$$r_{\mathrm{CCD}}(r,\theta) = -\kappa_0\theta \quad \text{and} \quad \theta_{\mathrm{CCD}}(r,\theta) = -\kappa_2\theta + \frac{r}{\kappa_0}, \tag{7.5}$$

which also represents the experimental situation in our case. The conversion factor from angle θ to position r_{CCD} is given by $\kappa_0 = 7.5\,\mathrm{mm}$ resulting in a spot radius of $|r_{\mathrm{max}}| = \kappa_0\theta_{\mathrm{max}} = 3\,\mathrm{mm}$. It is the ideal combination of lenses with the spot size being very close to the height of the CCD. The distance between the FP and SP lens can be chosen rather freely according to the experimental conditions, as it does not influence the angular resolution of this setup. On the other hand, if the distance is $d_2 = f_{\mathrm{FP}} + f_{\mathrm{SP}} = 700\,\mathrm{mm}$ the light would be collimated when incident on the slit of the spectrometer as $\kappa_2 = 0$ resulting in the most simple form

$$r_{\mathrm{CCD}}(r,\theta) = -\kappa_0\theta \quad \text{and} \quad \theta_{\mathrm{CCD}}(r,\theta) = +\frac{r}{\kappa_0}, \tag{7.6}$$

which is shown in Figure 7.7. In conclusion the distance between each of the three lenses should sum to their respective focal lengths.

Part IV

Results

Chapter 8

Transverse Magnetic Routing of Light Emission

Within this chapter we will introduce transverse intensity effects where light emission is routed and controlled by an external magnetic field. The effect named transverse magnetic routing of light emission (TMRLE) was discovered within the scope of this PhD thesis and is first reported on in our Nature Physics publication [Spi18]. Furthermore some of the experimental results presented in this chapter were gathered in the context of the master thesis of Lars Klompmaker [Klo17] and the bachelor thesis of Gabriel Honorio [Hon16], supervised by the author of this thesis.

Section 8.1 is about how the polarization of an emitter in a diluted magnetic semiconductor quantum well is established, induced by the giant Zeeman effect of excitons in a magnetic field. In the subsequent Section 8.2 the near-field effect – the most intense and also most important manifestation of TMRLE – is introduced. Here it is shown that the effect is only present for the emission with transverse magnetic polarization and 2D spectra are shown which illustrate how it depends on the emission angle. Further optimization of the grating period is proposed as one way to increase the effect's strength, before two kinds of far-field effects are discussed in Section 8.3. In the final three sections it is studied how the effect depends on the magnetic field strength (Sec. 8.4), the laser power (Sec. 8.5) and the sample temperature (Sec. 8.6).

8.1 Value of Magnetization – Giant Zeeman Effect

In this section the influence of an external magnetic field on the emission from QW excitons is described. As shown in Section 4.1, the exciton spectral line splits into several lines, depending on the selected polarization and the geometry of the magnetic field. In this case Sample 3 (see Section 6 for details) was studied, placed in a Faraday magnetic field of up to $B = 5\,\mathrm{T}$ at a temperature of $T = 2\,\mathrm{K}$ while being excited by a

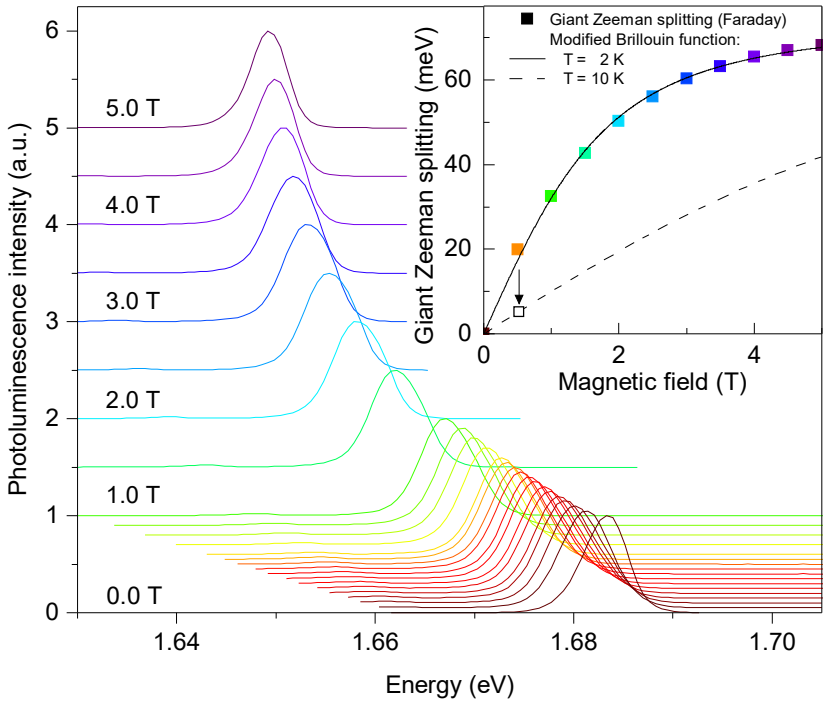

Figure 8.1: Circularly polarized (σ^+) photoluminescence spectra of QW excitons for magnetic fields up to 5 T in Faraday geometry at $T = 2\,\mathrm{K}$. Inset shows the magnetic field dependence of the exciton Zeeman splitting $\Delta E_{\mathrm{hh,F}}$ which is determined as twice the shift of the PL peak position with respect to the zero field peak. The solid line is a modified Brillouin function fit (Eq. (4.4a)) with $x = 0.0258 \pm 0.0003$, $T_{\mathrm{eff}} = (3.1 \pm 0.1)\,\mathrm{K}$ and $S_{\mathrm{eff}} = 5/2$. The dashed line shows the Zeeman splitting obtained from Eq. (4.4a) using the same parameters but for increased temperature $T = 11.1\,\mathrm{K}$. From this curve, we obtain the conditions $\Delta E_{\mathrm{hh,F}} = 5\,\mathrm{meV}$ at $T = 10\,\mathrm{K}$ and $B = 520\,\mathrm{mT}$ (open square) that are present in the Fourier imaging setup. Figure reprinted with permission from Reference [Spi18].

633 nm He-Ne laser using the setup described in Section 7.1. Sample 3 incorporates a 10 nm (Cd,Mn)Te quantum well based on a (Cd,Mg)Te epilayer and buried below the (Cd,Mg)Te cap. Diluted magnetic semiconductor QWs represent a model system with bright exciton emission and well known parameters [Fur88; Gaj10]. The giant Zeeman effect of hole spin levels in this structure originates from the strong $p-d$ exchange interaction between valence band holes and the Mn^{2+} ions [Fur88; Kuh94; Gaj10].

The QW emission originating from optically active heavy hole excitons, the lowest QW energy states, is detected spectrally resolved in circular σ^+ and σ^- polarization. The dependence of the σ^+ polarized emission line on the magnetic field strength is shown in Figure 8.1. At zero magnetic field, the emission line is located at an energy of

$E_{\sigma^+,0\,\mathrm{T}} = 1.683\,\mathrm{eV}$. With increasing magnetic field strength it shifts to lower energies, until it finally reaches $E_{\sigma^+,5\,\mathrm{T}} = 1.649\,\mathrm{eV}$ at a magnetic field of 5 T. Ordinarily, the Zeeman splitting is calculated as the energy difference between the σ^+ and σ^- polarized emission. As the intensity of the σ^- polarized emission vanishes quickly with increasing magnetic field – as a large splitting leads to a strong polarization of emitted light – the splitting is approximated as twice the energy difference of emission at $B = 0$ and $B \geq 0$

$$\Delta E_{\mathrm{hh,F}} = 2 \cdot (E_{\sigma^+,B=0} - E_{\sigma^+,B\geq 0}). \tag{8.1}$$

Consequently, the observed splitting reaches values of up to $\Delta E_{\mathrm{hh,F}} = 68\,\mathrm{meV}$ as shown by the filled squares in the inset of Figure 8.1. As pointed out in Subsection 4.1.1, the Zeeman splitting can be described by the modified Brillouin function (4.4a). For these structures the modified Brillouin function has two free parameters. The concentration of isolated Mn^{2+} ions x and the effective temperature of the manganese system $T_{\mathrm{eff}} = T + T_0$. Please note that in our case x is not the overall Mn concentration but the Mn^{2+}-ion concentration, which is why $S_{\mathrm{eff}} = 5/2$ is not used as a free parameter here. These two parameters can be extracted from fitting the Zeeman splitting as indicated by the solid line in the inset of Figure 8.1. From the fit a Mn^{2+} concentration of $x = 0.0258 \pm 0.0003$ and an effective temperature of $T_{\mathrm{eff}} = (3.1 \pm 0.1)\,\mathrm{K}$ were determined.

In some of the consequent sections a different experimental setup was used with a lower magnetic field of 520 mT and an increased sample temperature of 10 K. To compensate for these changed conditions the Zeeman splitting is calculated with an adjusted effective temperature of $T'_{\mathrm{eff}} = T_{\mathrm{eff}} + 8\,\mathrm{K} = 11.1\,\mathrm{K}$ resulting in a value of $\Delta E_{\mathrm{hh,F}} \approx 5\,\mathrm{meV}$ (empty square in the inset of Figure 8.1). If only the hole contribution is of interest, it might be calculated as follows

$$\Delta_{\mathrm{h,F}} = \frac{|\beta|}{|\alpha - \beta|} \Delta E_{\mathrm{hh,F}} = 4\,\mathrm{meV}. \tag{8.2}$$

The aforementioned measurements of the Zeeman effect were carried out on heavy hole excitons in Faraday magnetic field. In the following sections the focus lies on measurements in Voigt magnetic field though. Of special interest is the emission's degree of circular polarization in the yz-plane, as it is related to the transverse SAM and the TMRLE strength. As stated in Subsection 4.1.2, the degree of circular polarization can be calculated using Eq. (4.8). Taking into account the heavy hole Zeeman splitting from Eq. (8.2), the degree of circular polarization predicted for the idealized QW with infinite walls reads in this particular case

$$P_{\mathrm{c},\uparrow} \approx P_{\mathrm{c},\downarrow} \approx \frac{2}{3} \frac{\Delta_{\mathrm{h,F}}}{\Delta_{\mathrm{lh}}} = \frac{2}{3} \frac{4\,\mathrm{meV}}{20\,\mathrm{meV}} \approx 13\,\%, \tag{8.3}$$

where the ↑ arrow denotes the $|J_{\mathrm{h,x}}, S_{\mathrm{e,x}}\rangle = |+3/2, -1/2\rangle$ and ↓ the $|-3/2, +1/2\rangle$ exciton transition. The highest polarization degree was reached at the external magnetic field of $B = 5\,\mathrm{T}$ at a temperature of $T = 2\,\mathrm{K}$. The value of the giant Zeeman splitting exceeds $\Delta E_{\mathrm{hh,F}} = 68\,\mathrm{meV}$ with a hole contribution of $\Delta_{\mathrm{h,F}} = 54\,\mathrm{meV}$. Here the low field approximation from Eq. (8.3) does not apply anymore. However, the degree of circular polarization can be calculated according to [Ivc05; Spi18] yielding

$$P_{\mathrm{c},\uparrow} \approx 94\,\% \quad \text{and} \quad P_{\mathrm{c},\downarrow} \approx 82\,\%. \tag{8.4}$$

8.2 Near-Field Effect

In this section the TMRLE will be discussed, which is observed for magnetically polarized emitters that are located close to a surface breaking the medium's mirror symmetry. More explicitly, the wavevector $\boldsymbol{k}$ of the directional emission is proportional to

$$\boldsymbol{k} \propto \boldsymbol{B} \times \boldsymbol{e}_{\mathrm{z}}, \tag{8.5}$$

with the unit vector $\boldsymbol{e}_{\mathrm{z}}$ pointing in the direction normal to the surface and the magnetic field $\boldsymbol{B}$ pointing solely in x-direction.

The effect requires two key conditions in order to appear. On the one hand this is a light source whose optical selection rules are modified by the magnetic field. Any magnetic material fulfils this first condition. On the other hand the transverse spin of the emitted light (angular momentum) should be non-vanishing, i.e. $\boldsymbol{S} \parallel \boldsymbol{e}_{\mathrm{x}} \perp \boldsymbol{k}$. The second condition requires a structure with broken $z \to -z$ symmetry, like a planar mirror [Bek15]. When propagating inside a medium apart from the surface, a conventional electromagnetic plane wave remains linearly polarized and its propagation direction is independent of its polarization direction. Therefore, in bulk material only weak directionality effects can be expected. Sub-wavelength optical fields on the other hand possess strong transverse spin like all evanescent waves and carry a spin flux, whose spin is locked to their propagation direction [Ley07; Bli15b; Lod17].

This enables fascinating phenomena like the application of lateral forces on near surface particles controlled by the polarization of light [Rod15]. Furthermore photonic wheels in tightly focused beams [Aie15] and the photonic spin Hall effect in hyperbolic materials [Kap14] are manifestations of this near surface spin momentum locking. The generation of such photonic spin fluxes has been established both in dielectric photonic structures containing a quantum dot [Lux13; Söl15; Col16] or a single atom [Jun13; Sho14]. In the case of plasmonic excitations – where collective oscillations of electrons in a metal occur – plasmon scattering on nano-particles allowed to visualize these

spin fluxes [Lin13; Rod13; Bau14; OCo14; Pet14; Rod14; Lef15; Sin17]. In summary, sub-wavelength evanescent optical fields that are present in photonic as well as plasmonic nanostructures are expected to enable the transverse magnetic routing of light emission.

8.2.1 Sign of TMRLE for Photonic and Plasmonic Spin Fluxes

The exciton emission from a diluted magnetic semiconductor quantum well was studied for the experimental demonstration of TMRLE. As described before the effect is expected to be significantly enhanced by sub-wavelength optical fields. Thus also hybrid plasmonic structures with a metallic grating in close proximity to the QW were considered. The grating placed on top of the semiconductor structure contributes in two ways:

- Surface plasmon polaritons are supported at the metal-semiconductor interface.
- Optical spin fluxes which are carried by surface modes at the gold / (Cd,Mg)Te interface are out-coupled into the far-field radiation.

The lowest QW energy states correspond to optically active heavy hole excitons as described in Section 8.1 from which the emission originates. The excitons can be considered localized due to the QW inhomogeneity and thus modelled as point electric dipoles. While at zero magnetic field B, their angular momentum projection is $J_\mathrm{z} = \pm 1$ along the QW confinement z-axis. This corresponds to circularly polarized dipoles rotating in the xy-plane clockwise or counter-clockwise, $d_\mathrm{x}\boldsymbol{e}_\mathrm{x} \mp \mathrm{i}d_\mathrm{y}\boldsymbol{e}_\mathrm{y}$ with $d_\mathrm{x} = d_\mathrm{y}$. Therefore light of equal intensity is emitted in all lateral directions and no directional emission is observed.

With an in-plane magnetic field $\boldsymbol{B} \parallel \boldsymbol{x}$ on the other hand, the selection rules of the optical transitions are modified and the emission becomes elliptically polarized in the yz-plane. This corresponds to dipoles with polarization $\boldsymbol{d}^{\pm}_\mathrm{X} = d_\mathrm{y}\boldsymbol{e}_\mathrm{y} \mp \mathrm{i}d_\mathrm{z}\boldsymbol{e}_\mathrm{z}$. As mentioned in Eq. (4.8) the related circular polarization degree is $P_c = \pm 2d_\mathrm{y}d_\mathrm{z}/(d_\mathrm{y}^2 + d_\mathrm{z}^2) \approx \pm\frac{2}{3}\Delta_{\mathrm{h,F}}/\Delta_\mathrm{lh}$ for $\Delta_{\mathrm{h,F}} \ll \Delta_\mathrm{lh}$. Here Δ_lh is the energy splitting between heavy- and light-hole states due to confinement and strain in the QW. The Zeeman splitting of heavy-holes in Faraday geometry $\Delta_{\mathrm{h,F}}$ grows linearly for small B and was already introduced in Eq. (8.2). As all the structures discussed are mirror symmetry broken with respect to the z-axis, the optical field carries non-zero transverse SAM. Therefore the excitons with elliptically polarized dipole moments couple preferentially, depending on the magnetic field sign, either to right-going or left-going waves. This results in the directional emission effect called TMRLE which is the main focus of this chapter.

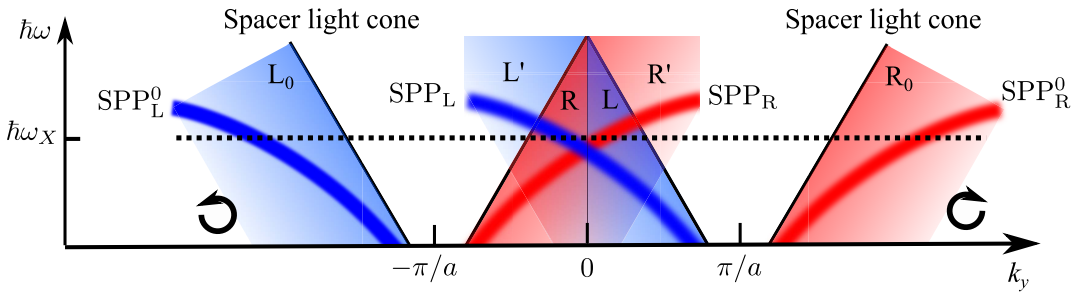

Figure 8.2: Schematic presentation of the dispersion for evanescent electromagnetic waves in the plasmonic grating. Their contribution to TMRLE in the far-field emission is shown in blue and red colour. The dispersion branches of the SPPs at a homogeneous gold boundary are $\mathrm{SPP}^0_{\mathrm{R,L}}$ and the diffracted dispersion branches are $\mathrm{SPP}_{\mathrm{R,L}}$. The photonic modes on a flat gold film are labelled by R_0 / L_0. The labels R / R' and L / L' represent the modes shifted by the reciprocal lattice vector. In the area with a dashed label the sign of plasmonic and photonic modes is the same and vice versa. Figure adapted with permission from Reference [Spi18].

The working principle is shown in Figure 8.2. Here the red / blue outer areas show the situation for a flat gold film, where R_0 and L_0 represent the photonic modes while $\mathrm{SPP}^0_{\mathrm{R}}$ and $\mathrm{SPP}^0_{\mathrm{L}}$ are the surface plasmon polariton modes. The colour on the other hand shows the impact on directionality (see Eq. (8.7)) with $C > 0$ in blue and $C < 0$ in red. Translating the regions R_0 and L_0 by the grating's reciprocal lattice vectors $k_{\mathrm{y}} = -2\pi/a$ and $k_{\mathrm{y}} = 2\pi/a$ leads to the areas R, R′, L, L′. In the same way also the surface plasmon polariton dispersion is shifted into the grating's first Brillouin zone resulting in $\mathrm{SPP}_{\mathrm{R}}$ and $\mathrm{SPP}_{\mathrm{L}}$. Interestingly, the directionality of transverse photonic and plasmonic spin fluxes observed in the far field can either compensate or enhance each other in periodic structures. This becomes apparent when looking at the region L, which is crossed both by $\mathrm{SPP}_{\mathrm{R}}$ and $\mathrm{SPP}_{\mathrm{L}}$. While L and $\mathrm{SPP}_{\mathrm{L}}$ enhance each other, L and $\mathrm{SPP}_{\mathrm{R}}$ compensate each other. At a given frequency the spin has maxima both at the SPP branches and in the regions just below the light dispersion lines. Here k_{z} is small and thus the electric field $E \propto e^{-|k_z z|}$ is rather strong. The regions of the diffracted right- and left-propagating evanescent waves overlap each other in the dispersion diagram. Consequently at both of their boundaries the transverse spin sign reverses, i.e. at the L′–R and L–R′ boundary. Additionally, the routing effect becomes larger in the regions L′ (R′) as the opposite sign evanescent wave contribution from the region R (L) vanishes. Depending on the energy the relative sign of the transverse spin for the diffracted SPPs and photons changes. While the sign is the same below the crossing point of the $\mathrm{SPP}_{\mathrm{R}}$ and $\mathrm{SPP}_{\mathrm{L}}$ branch it is opposite above the crossing point.

8.2.2 Directionality of Emission

To reduce the strength of directionality down to a single number the normalized difference of the two intensities I_+ and I_- can be studied, which are observed for positive and negative transverse SAM $S_\mathbf{x}$

$$\rho(\theta) = \frac{I_+(\theta) - I_-(\theta)}{I_+(\theta) + I_-(\theta)}. \tag{8.6}$$

Here θ is the emission angle in air which is used in the subsequent experiments. This quantity is positive if more light is detected at a given angle θ for an emitter with positive SAM $S_\mathbf{x} > 0$. On the contrary less emission under this angle at positive SAM results in a negative ρ. Here the optimum is reached if the emission intensity is zero for one emitter polarization resulting in $|\rho| = 100\,\%$. In the experiment the spin of the emitter is pinned to the magnetic field i.e. $S_\mathbf{x} \propto B_\mathbf{x}$, due to the modified selection rules introduced in Section 4.1. Thus in the experiments I_+ represents the intensity measured at positive magnetic field and vice versa.

However, there is one theoretically possible scenario where the quantity ρ would give erroneous results, i.e. if the light source's overall intensity does change when its spin is flipped. One example is a light source that emits only at positive spin thus $I_+(\theta) > 0$ and $I_-(\theta) = 0$ irrespective of the emission angle θ. This would give an effect strength of $\rho = 100\,\%$ for all θ, i.e. both at $+\theta$ and $-\theta$. In order to quantify how well the emission is routed into a specific direction, we compare ρ for two opposing emission angles and call the resulting factor directionality:

$$C(\theta) = \frac{\rho(+\theta) - \rho(-\theta)}{2} \tag{8.7}$$

This quantity is robust to omnidirectional intensity changes. Usually, apart from statistical variations, the emission intensity is about constant for all measurements taken. In the following experiments the two quantities ρ and C are thus considered equivalent. This assumption is indeed valid, except for C being antisymmetric when inverting the emission angle $\pm\theta$ due to the way it was defined in Eq. (8.7), while ρ might underlie statistic variations and other disturbances and thus might be not strictly antisymmetric. As a rule of thumb, in the case of an angular resolved spectrum ρ is plotted as it is the more intuitively accessible description of the measured data. In the case of a spectrum at fixed angle usually the directionality C is shown as it contains also the data at the same but negative emission angle and thus is the more significant parameter in this case.

Two special cases are interesting to discuss here. On the one hand, at the minimal emission angle of $\theta = 0°$ the two angles $\pm\theta$ being compared are identical, which

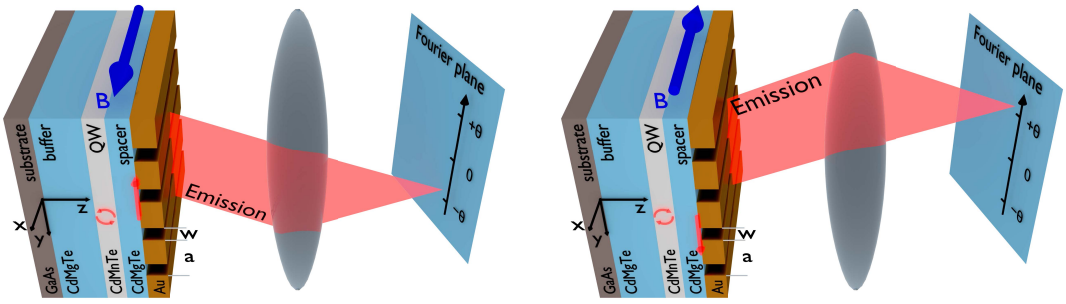

(a) Positive magnetic field $B_x > 0$ **(b)** Negative magnetic field $B_x < 0$

Figure 8.3: Scheme of transverse magnetic routing of light emission (TMRLE).
All elements necessary to observe TMRLE are depicted in this figure. The external magnetic field is shown as a blue arrow. In (a) the magnetic field is positive which leads to the exciton emission to be polarized as indicated by the red circular arrows. Emission polarized in this way launches a SPP propagating in negative y-direction. This SPP is then coupled out under the emission angle $-\theta$. A Fourier imaging setup is used to convert the angular dependence of emitted light into the spatial dependence in the Fourier plane which is projected onto the spectrometer slit. In (b) on the other hand, the magnetic field direction is flipped resulting in the inverted exciton polarization, SPP propagation direction and emission angle.

obviously leads to no difference in observed intensity thus $C(0°) = 0$. On the other hand, at the maximum emission angle of $\theta = 90°$ the structure's symmetry in propagation direction is not broken anymore also leading to $C(90°) = \rho = 0$. The angle of maximum effect strength thus is in between these two and depends on the degree of circular polarization of the emitter, on the two materials used, on the magnetic field, etc. and is non-trivial to determine.

8.2.3 Polarization Dependence

The TMRLE requires emitter and detected light to be TM polarized (p-polarization) while it is expected to be zero in TE polarization (s-polarization). This can be easily confirmed by detecting the PL intensity of Sample 2 at a fixed emission angle of $\theta = 15°$ with the setup described in Section 7.2. As stated in Section 6, Sample 2 consists of a 10 nm thick (Cd,Mn)Te QW sandwiched between a (Cd,Mg)Te epilayer and cap as the light source and a rectangular gold grating on top with $a = 250$ nm period.

A 552 nm-laser is used for excitation with a photon energy of 2.25 eV in order to populate the QW with excitons. The emission band of QW excitons is centred at the energy $\hbar\omega \approx 1.67$ eV and depends weakly on the emission angle θ. The spectral width at half maximum of the PL band of about 10 meV allows to measure the emission

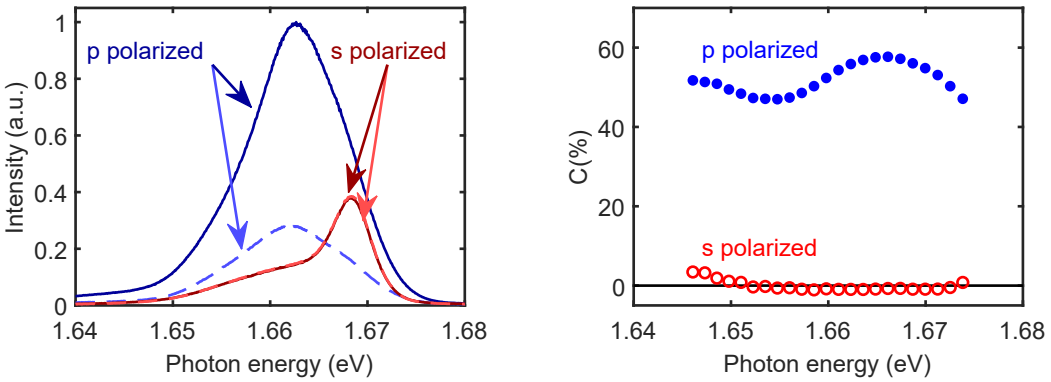

(a) PL spectra of p- and s-polarized emission at $T = 2\,\mathrm{K}$, $B = \pm 1.5\,\mathrm{T}$ and $\theta = 15°$. Spectra for positive magnetic field are shown as solid lines. Dashed lines represent negative magnetic field.

(b) Directionality factor C for p- and s-polarized emission shown as solid and open circles, respectively.

Figure 8.4: TMRLE at high magnetic field and fixed emission angle.

pattern in the spectral range from 1.64 to 1.69 eV. During the measurement, the sample was kept at a temperature of $T = 2\,\mathrm{K}$ within an external magnetic field of $B = \pm 1.5\,\mathrm{T}$. Under these conditions, nearly all Mn^{2+} ions in the QW are polarized along the external magnetic field and the polarization reaches about 80 % as shown in Eq. (8.4).

Now the TM polarized PL intensity is measured energy resolved with a CCD behind a spectrometer in the detection path. The resulting PL spectrum is shown in Figure 8.4a as a dark blue solid curve. When inverting the magnetic field direction $B \to -B$ also the emitter's polarization flips its spin. The resulting PL spectrum is shown as a light blue dashed curve. Interestingly, this intensity is weaker by a factor of four due to the dipole now coupling to the SPP wave propagating in the opposite direction and emitting mostly at the opposite angle. From these two curves ρ can be easily calculated (see Eq. (8.6)), giving an effect strength of about $\rho = \frac{4-1}{4+1} = 60\,\%$. Measurements for the opposite angle show the same behaviour but inverse sign, as expected. Thus, instead of ρ the more significant directionality C is shown in Figure 8.4b as blue filled dots.

In case of TE polarized emission or s-polarization the situation differs significantly. The two PL spectra measured at positive and negative magnetic field coincide as shown by the red curves in Figure 8.4a. Obviously this gives no effect or $\rho = 0$ as intensity does not change in this case. Directionality is about zero for all energies

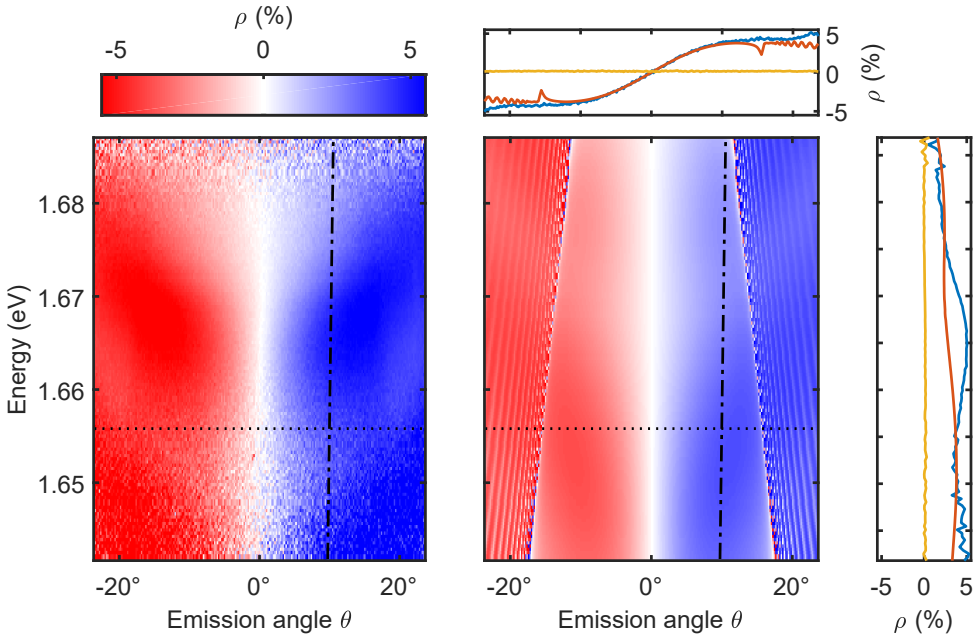

Figure 8.5: Angle- and spectrally-resolved TMRLE pattern on Sample 2 at $B = 520\,\mathrm{mT}$ and $T = 10\,\mathrm{K}$. Left and right coloured panels correspond to measured and calculated $\rho(\hbar\omega, \theta)$-patterns, respectively. Side plots at the calculated pattern shows cross-sections along fixed photon energy $\hbar\omega = 1.656\,\mathrm{meV}$ as indicated by the dotted line (upper plot) or fixed angle $\theta = 10°$ as indicated by the dash-dotted line (right plot). Blue and red curves in these plots correspond to cross-sections of experimental data and calculation results, respectively. Yellow curves in the side plots shows the absence of TMRLE signal in s−polarization.

along the exciton PL peak in TE polarization as shown as red empty circles in Figure 8.4b.

In comparison to the TMOKE (see Chapter 9) which is measured in the same geometry and on the same samples, the TMRLE is more than one order of magnitude stronger – up to 60 % instead of 1 %. It is so intense that the magnetic field induced intensity switching can even be seen with the bare eye!

8.2.4 Angle Resolved TMRLE

Now that the extent of TMRLE with up to 60 % is demonstrated, the effect will be studied further by exploring the dependence on the emission angle. One much more convenient way to do so is by detecting an angle resolved pattern with a single shot, instead of composing measurements at different fixed angles. A setup to measure

such an angle resolved pattern is given by the Fourier imaging setup described in Section 7.3. This setup has the disadvantage that the magnetic field strength is limited to $B = 520\,\mathrm{mT}$ while the sample is kept at a slightly higher temperature of $T = 10\,\mathrm{K}$, though. In a Fourier imaging setup the angular dependence of emitted light is converted into the spatial dependence in the Fourier plane. This plane is projected onto the slit of a spectrometer. Hereby angle- and spectrally-resolved exciton emission is detected as a contour pattern with a CCD camera, attached to an imaging spectrometer.

In Figure 8.5 the resulting contour pattern of such a measurement is shown. The left coloured panel corresponds to the measured $\rho(\hbar\omega, \theta)$ pattern, while the right coloured panel displays the calculated pattern. These calculations were performed by the scattering matrix method described in Section 5.4. The theoretical calculations show good agreement with the experimental data, as only the degree of circular polarization P_c was used as a fit parameter. All the simulations shown in Chapter 8 use a value of $P_\mathrm{c} = 2.6\,\%$ consistently. In comparison to the value of $P_\mathrm{c} = 13\,\%$ predicted in Eq. (8.3) for the idealized QW with infinite walls, the polarization is decreased. In the actual QW the overlap between light and heavy hole wave functions $|\langle\Psi_\mathrm{lh}|\Psi_\mathrm{hh}\rangle|^2 \ll 1$ is reduced, which can explain this discrepancy. In the limit of large magnetic fields on the other hand this discrepancy should be absent as there $\Delta_\mathrm{h,F} \gg \Delta_\mathrm{lh}$ and nearly all Mn ions are polarized along the external magnetic field with the polarization reaching $P_\mathrm{c} = 80\,\%$. Thus, the measurement of the magnetic field dependence of TMRLE as well as the calculation of TMRLE as a function of P_c are of special interest and will be focused on in Section 8.4.

Within the energy range shown here, which is predetermined by the PL spectrum of the exciton resonance, the TMRLE only has a weak spectral dependence and does not change its overall sign. The weak spectral dependence can be easily explained, as the resonance condition $\omega_\mathrm{X} = \omega_\mathrm{SPP}$ is met within this range. The spectral width of the exciton PL band of about 10 meV is much narrower than the SPP resonance with about 50 meV. For positive emission angles the effect is also positive with a strength of up to $\rho = 5\,\%$. Looking at the same negative emission angle on the other hand $\rho(\hbar\omega, \theta)$ is negative while the magnitude stays virtually the same. As expected, the effect strength is less than in the preceding chapter, as lower magnetic field and higher temperature reduce the Mn^{2+} polarization and consequently the emitter's polarization degree.

Two additional plots in Figure 8.5 show one dimensional cuts through these patterns. On top of the right panel a cut along a fixed energy of $\hbar\omega = 1.656\,\mathrm{meV}$ is shown with the experimental spectrum in blue, the calculated spectrum in red and the s-polarized experimental spectrum in yellow (two-dimensional panel not shown). While the effect in s-polarization is absent as previously discussed, up to $\pm 5\,\%$ of

effect can be observed in p-polarization. Fortunately the experimental spectrum agrees very well with its calculated counterpart. In the simulations some additional feature is discernible beginning at the Wood's anomaly (described in Section 3.4) as a white line and continuing with a slight interference for larger emission angles. In the experimental picture it is invisible to the eye as it might be blurred due to the experiments resolution of $\sigma_\theta \leq 0.5°$ and $\sigma_\mathrm{E} \leq 1.4\,\mathrm{meV}$ at this energy range.

Rightmost a cross-section along a fixed emission angle $\theta = 10°$ is shown. Again the effect in s-polarization is virtually absent while 1 % to 5 % are present in both the experimental data and calculations. In this figure an additional $\approx 20\,\mathrm{meV}$ period oscillation of ρ is observed in the experiment which can be attributed to an interference effect due to the reflection of emitted light at the substrate (see Subsection 8.3.2 for more details on this effect). One should emphasize that this is not the same interference which was observed due to the Wood's anomaly (multiple white lines in the 2D simulations). The interference visible in the 1D cut along fixed angle in the very right of Figure 8.5 is broader and originates from the interferences in the buffer.

8.2.5 Optimization of the Grating Period

Even though the proof of principle was the main interest, achieving an even more pronounced effect strength is always desirable. Until now the grating period was kept unchanged at $a = 250\,\mathrm{nm}$ yielding effect strengths of $\rho = 5\,\%$ at low magnetic fields and notable $\rho = 60\,\%$ at higher magnetic fields. Increasing the magnetic field strength further is rather futile as nearly all Mn^{2+} ions are aligned already. Modifying the grating period however allows tuning the SPP and exciton resonance closer to each other. The period dependence of directionality in Figure 8.6a and the related dispersion diagram in Figure 8.6b demonstrate this specific approach. For this dependence measurements on the same sample (Sample 2), but with varied grating periods between $a = 200\,\mathrm{nm}$ to 320 nm have been performed at consistently $B = 520\,\mathrm{mT}$ and $T = 10\,\mathrm{K}$. While the single measurements show a rich picture (see Figure 8.7), it is more intelligible to describe the whole measurement by a single number and compare these numbers for different grating periods. This is done by first constraining the measured data to a fixed angle of $\theta = 15°$ and then spectrally integrating over all measured intensities. The overall intensity is subsequently compared as described before in Eq. (8.6).

Starting with lower grating periods the directionality is slightly negative with about $C \approx -1\,\%$. With increasing grating period the effect rapidly changes its sign with positive values of roughly up to 6 % at $a = 240\,\mathrm{nm}$ as compared to about 4 % at $a = 250\,\mathrm{nm}$. It is important to emphasize this point, as changing the grating period

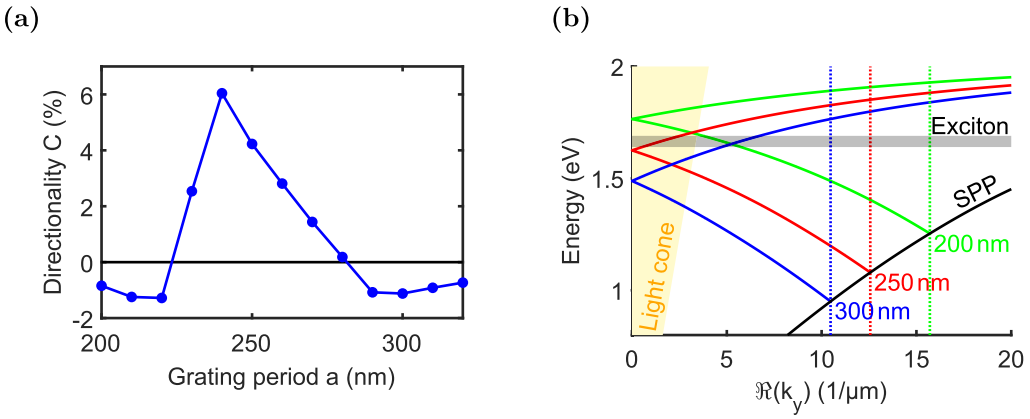

Figure 8.6: (a) Directionality C observed for different grating periods from 200 nm up to 320 nm in Sample 2 at $B = 520\,\mathrm{mT}, T = 10\,\mathrm{K}, \hbar\omega = 1.67\,\mathrm{eV}$ and $\theta = 15°$. **(b)** Dispersion diagram of QW exciton emission shown as grey shaded area and an SPP wave at the gold / (Cd,Mg)Te interface (black curve) in empty lattice approximation calculated according to Eq. (3.9). The estimated SPP dispersion was slightly shifted by $k_{\mathrm{y,SPP}} \rightarrow k_{\mathrm{y,SPP}} + 2.5\,\mu\mathrm{m}^{-1}$ to match the experimental reflection spectrum and associated numerical calculations. Green, red and blue lines represent the SPP dispersion folded into the first Brillouin zone at $k_{\mathrm{y}} = \pi/200, \pi/250$ and $\pi/300\,\mathrm{nm}^{-1}$ respectively. The orange area shows the light cone being detected in a Fourier setup with NA = 0.4. Only the SPP modes segment located inside the light cone is observed when out-coupled. TMRLE is only observed when all three areas – emission (grey area), SPP (coloured line), detection (orange area) – coincide.

by only 10 nm leads to an 1.5-fold increased effect strength. For even higher grating periods there is a slow linear decrease until reaching about $C \approx -1\,\%$ again. In conclusion, using the optimized 240 nm grating period in combination with higher magnetic fields and lower temperatures should boost the maximum effect strength even further, potentially even above 80 %.

The dispersion diagram in Figure 8.6b allows for a deeper understanding of this period dependence. In this figure the spectral range with exciton emission is depicted as a grey shaded area while the orange shaded area represent the light cone inside which light emerging from the sample can be detected. Thus, the cross section of these two areas – the detectable emission – defines our measurement range shown in the previous chapter. Additionally, the unfolded SPP dispersion is shown as a black curve. The SPP dispersion was estimated by the empty lattice approximation Eq. (3.9) for a smooth gold film which was subsequently shifted by $\Delta k_{\mathrm{y,SPP}} = -2.5\,\mu\mathrm{m}^{-1}$ to improve congruence with experimental reflection spectra and associated numerical calculations. As discussed in Section 3.3 the unfolded SPP dispersion does not intersect the light cone (orange shaded area) and thus cannot be observed in experiment without further preparation of the sample surface.

For a patterned gold grating the SPP dispersion is folded back at $k_y = \frac{\pi}{a}$ into the first Brillouin zone. The folded SPP dispersion intersects the light cone and thus can be out-coupled from the structure. But only for a limited range of grating periods the SPP resonance also lays within the grey area representing the exciton emission. All three domains have to coincide in order to see SPP-enhanced TMRLE for the emission from QW excitons. This neither is the case for the green 200 nm nor the blue 300 nm SPP resonance as there is no overlap with the emission inside the light cone. For these two grating periods SPPs and emission are far apart and only far-field effects may play a role. Comparing with the left figure shows that for these grating periods there is an offset of $C = -1\,\%$ which is unrelated to the SPPs but comes from superimposed far-field effects discussed in the next section. In between these two curves the SPP related near-field effect is dominating. Starting at slightly below 300 nm the upper SPP branch begins to enter the detectable emission which leads to an increase in directionality until at about 240 nm the best overlap is achieved. For the upper branch the SPP wave is propagating in positive y-direction as the group velocity is

$$\frac{\mathrm{d}\omega}{\mathrm{d}k_{\mathrm{y,SPP}}} > 0. \tag{8.8}$$

Further decreasing the grating period leads to a rapid decrease and another sign change of the effect. This can be easily understood, as now the lower SPP branch shifts further and can be both excited and detected. As in this case the group velocity is negative, also the polarization of the SPP wave switches its sign and couples inversely to the magnetic field resulting in a negative contribution to the overall directionality. At even lower grating periods, only the lower SPP branch is excited by the emission and the overall effect reaches its lowest point at about 220 nm before also the lower branch moves out of sight and only far-field effects dominate the picture.

Figure 8.7 shows the 2D measurements from 210 nm to 320 nm. The overall behaviour described before can be observed here as well. For the 210 nm grating the effect is negative at positive emission angles. Here the SPP and exciton resonance are distant and far-field effects are prevalent. With increasing grating period the SPP resonance is shifting and starts to cross the exciton spectral line, leading to the strong feature with opposite sign beginning at 230 nm grating period. At 240 nm it is substantially larger than the far-field effect for the entire visible spectral range and in accordance with Figure 8.6a the maximum effect strength is observed. Further increasing the period leads to a decay of the near-field effect until at 320 nm the overall picture looks comparable again to 200 nm with negative effect strength at positive angles. Yet the diverse angular and energy dependent behaviour is not fully studied and might require a more complex theoretical model for description.

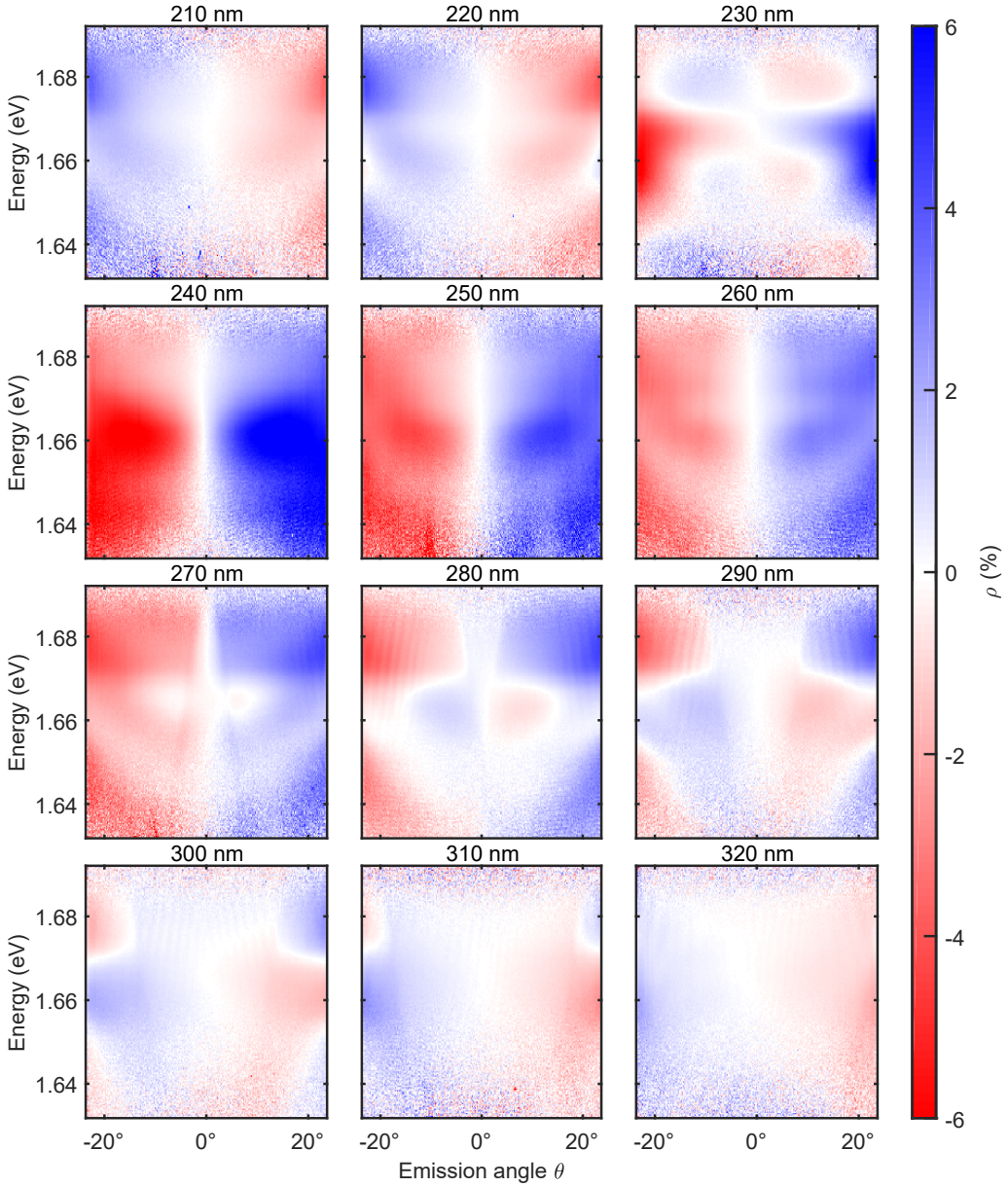

Figure 8.7: False colour plot of the angle resolved TMRLE spectrum for grating periods from 210 nm to 320 nm in Sample 2 at $B = 520\,\mathrm{mT}$ and $T = 10\,\mathrm{K}$.

8.3 Far-Field Effects

While the previous section covered the near-field effects initiated by exciton emission into the evanescent optical modes, the focus now lies on two far-field effects that can be studied in slightly altered samples with the same Fourier imaging setup. Both far-field effects are based on the interference of emitted light rays.

8.3.1 Analytical Solution of the Far-Field Routing of Light in a Structure with Finite Buffer Thickness

The near-field routing of dipole emission occurred in the proximity of the metal / dielectric interface. But in fact directional emission is already observed for a dipole located in a structure that contains no metal layer while the symmetry remains broken in the z-direction as shown in Figure 8.8a. In this structure the first far-field effect is observed. The directionality in this case is caused by the interference of several emitted light rays, i.e. between the directly emitted and the reflected electromagnetic waves. The reflection occurs at the backside of the structure where the substrate is located, as shown in Figure 8.8a. In contrast to the near-field effect, coupling to sub-wavelength optical fields is not required. Instead the distance of the dipole emitter and the closest interface can be large. In the most simple case the permittivity of the QW layer is assumed to resemble its surrounding, resulting in a three layer system – substrate, buffer and air. For this system we will now calculate the directionality pattern analytically.

We use the dipole's polarization $\boldsymbol{p}$ as introduced in Eq. (5.3). Only the TM-polarized component of the detected light beam in free space contributes to TMRLE. Each beam emitted under the angle θ outside the structure can originate either from the directly emitted light and thus has an electric field oriented in

$$\boldsymbol{e}^{\text{direct}} = \begin{pmatrix} 0 \\ \cos(\alpha) \\ -\sin(\alpha) \end{pmatrix} \tag{8.9a}$$

direction or it was reflected from the backside of the structure and thus reads

$$\boldsymbol{e}^{\text{reflected}} = \begin{pmatrix} 0 \\ -\cos(\alpha) \\ -\sin(\alpha) \end{pmatrix}. \tag{8.9b}$$

Here α denotes the angle inside the semiconductor material according to Snell's law (3.3). Now the intensity of the superimposed waves in free space can be easily calculated. Here the Fresnel coefficients $t_p^{1\to 0}$ for transmission of TM-polarized light

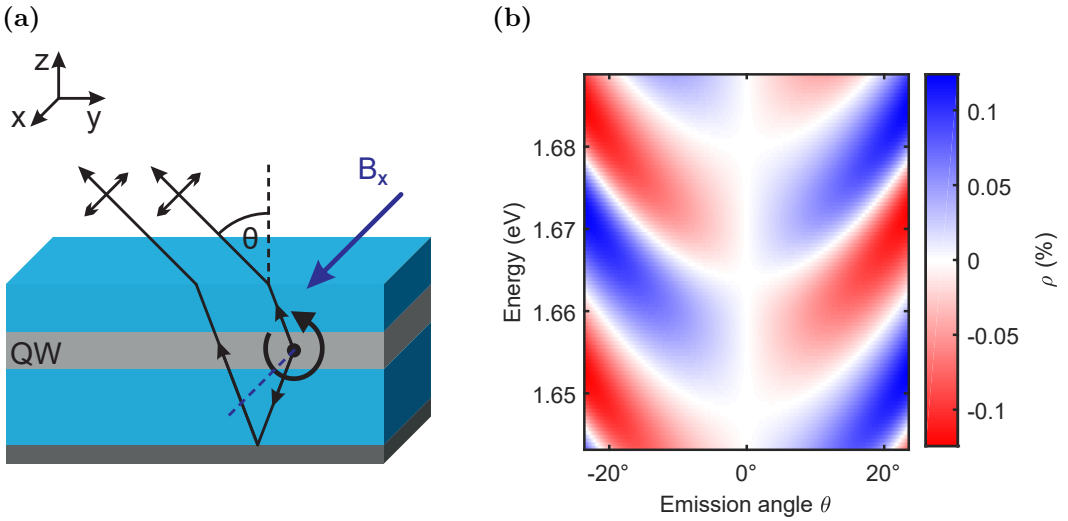

Figure 8.8: (a) Scheme of TMRLE on the unstructured part of Sample 2. Reflections at the buffer layer superimpose with the direct emission resulting in Fabry–Pérot interferences. The overall intensity at the emission angle θ in free space depends on the phase between the two beams and thus on the helicity of the dipole emitter. Figure adapted with permission from Reference [Spi18]. **(b)** Calculation of TMRLE for the structure shown in (a) based on the Fresnel equations shown in Section 3.1

from the semiconductor into free space and $r_p^{1\to2}$ for reflection of TM-polarized light at the semiconductor and substrate interface as described in Section 3.1 are used. With this said, the detected emission intensity reads

$$I = \left|\left(t_p^{1\to0}\boldsymbol{e}^{\text{direct}} + r_p^{1\to2}t_p^{1\to0}\exp\left(2\mathrm{i}\phi\right)\boldsymbol{e}^{\text{reflected}}\right)\cdot\boldsymbol{p}^*\right|^2, \tag{8.10}$$

which explicitly still depends on the circular polarization degree P_c. For the interference of the two beams also the different beam path length plays a role resulting in a phase

$$\phi = \frac{2\pi d n_1}{\lambda}\cos(\alpha) \tag{8.11}$$

between both beams, where d is the buffer thickness and n_1 is the (Cd,Mg)Te buffer refractive index [Lip69]. For the calculations a circular polarization degree of $P_\mathrm{c} = \pm 2.6\,\%$ was used and the Fresnel coefficients were calculated with the corresponding refractive indices from references [And97; Asp86]. With these two contributions the directionality ρ can be calculated according to (8.6), where I_+ is the intensity for an emitter with positive transverse SAM ($P_\mathrm{c} = 2.6\,\%$) and I_- the intensity observed for the opposite spin ($P_\mathrm{c} = -2.6\,\%$). The resulting directionality dependence $\rho(\theta, E)$ is shown in Figure 8.8b. The effect is fully antisymmetric with

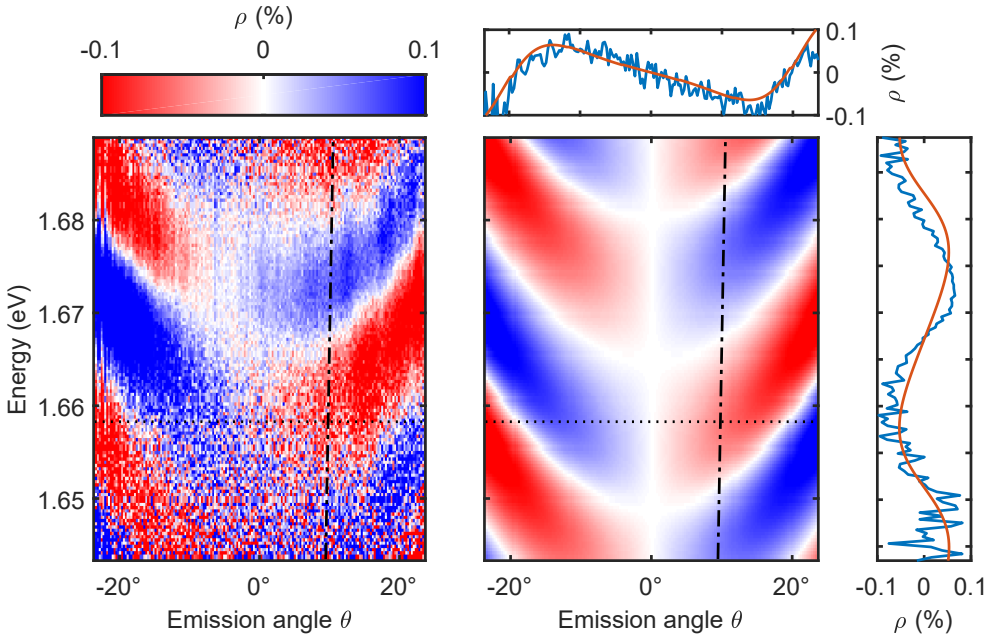

Figure 8.9: Angle- and spectrally-resolved TMRLE pattern at $B = 520\,\mathrm{mT}, T = 10\,\mathrm{K}$ for Sample 2b. Left and right coloured panels correspond to measured and calculated $\rho(\hbar\omega, \theta)$-patterns, respectively. Side plots at the calculated pattern shows cross-sections along fixed photon energy $\hbar\omega = 1.658\,\mathrm{meV}$ as indicated by the dotted line (upper plot) or fixed angle $\theta = 10°$ as indicated by the dash-dotted line (right plot). Blue and red curves in these plots correspond to cross-sections of experimental data and calculation results, respectively.

respect to the emission angle θ. This can be easily understood, as flipping the angle from $\theta \to -\theta$ is tantamount to a 180° rotation of the whole structure around the z-axis, which would invert the transverse SAM in the yz-plane as well as $P_\mathrm{c} \to -P_\mathrm{c}$ resulting in $\rho \to -\rho$. Consequently, flipping both the angle and the transverse spin would again result in the starting geometry thus yielding the same emission intensity.

8.3.2 Interference Effect on Unstructured Sample

In order to observe these interferences experimentally, the same Fourier imaging setup was used, which already has been described in Section 7.3 and Subsection 8.2.4. The resulting $\rho(\hbar\omega, \theta)$ pattern is shown in Figure 8.9. Similarly to Figure 8.5, the left coloured panel shows the experiment while the right panel corresponds to the scattering matrix calculations. The energy range shown is predetermined by the exciton PL spectrum. In contrast to the near-field effect, in this case the directionality

is several orders of magnitude smaller with $|\rho| < 0.1\,\%$. Moreover, the TMRLE pattern exhibits a strong frequency dependence with $\rho(\hbar\omega, \theta)$ oscillating around zero with a $\approx 30\,\mathrm{meV}$ period. Thus, for emitters spectrally located at the zero-crossing of these interferences or for broadband emitters covering several interference periods the overall spectrally-integrated directionality would decrease even further.

The calculated directionality pattern nicely reproduces all these features and shows good agreement with the experiment. For better comparison one dimensional cuts along the emission angle are shown in the top panel. These cuts are represented in the directionality pattern by a dotted line. Additional cuts along the energy axis are represented by dash-dotted lines and shown in the right panel. Both panels manifest the remarkable agreement between theory and experiment. However, the one dimensional energy cut exposes small deviations in the interference's shape while both the period and directionality magnitude match. This is the most simple approach for achieving directional emission but it also results in the weakest directionality.

As there are no periodic grating structures on top of the semiconductor the sample is uniform in the xy-plane. This even allows the analytical calculation of the effect, which was discussed in Subsection 8.3.1 with the result shown in Figure 8.8b. First of all, the strength of TMRLE being $|\rho| \approx 0.1\,\%$ fits well with both the experimental data and the scattering matrix based simulations. Also the overall two-dimensional $\rho(\hbar\omega, \theta)$ pattern looks virtually the same as in the simulation. All in all this near-field effect is a nice example of routing emission, as it is quite simple and can be measured even in unsophisticated structures with only a properly polarized emitter. On the other hand it is quite weak due to the lack of plasmonic enhancement and needs some effort to be measured.

8.3.3 Diffraction Effect on Patterned Sample

The second far-field effect is manifested in Sample 1, where the spacer thickness is larger with 250 nm instead of 32 nm, while here also the patterned part of the structure with a 250 nm grating is studied. Here the Fourier imaging spectroscopy setup shows a quite comprehensive picture as shown in Figure 8.10. Surprisingly the maximum strength of directionality is only slightly lower with about 2 % as compared to the 5 % which have been observed with plasmonic enhancement. Examining the same two-dimensional patterns as before, where the experiment is placed left and the simulations are shown on the right, reveals the origin of this far-field enhancement. The step-like increase of ρ at an angle of about $\theta_{\mathrm{Wood}} \approx 11°$ to $17°$ is related to the appearance of the grating's first order diffraction. The shape of this step-like increase can be understood by recalling the well known Wood's anomaly presented in Section 3.4. The directionality in this case emerges from the interference of

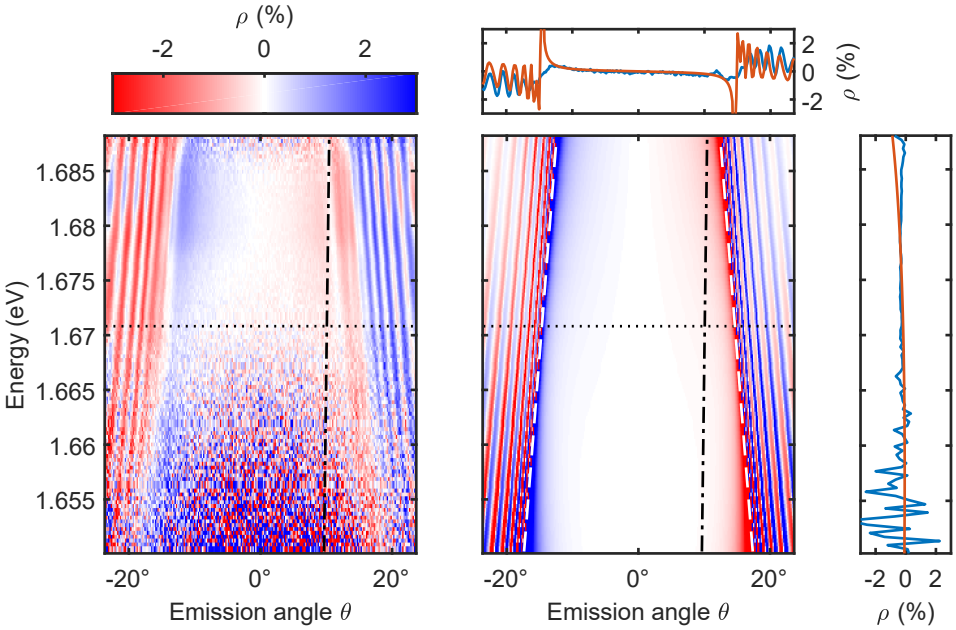

Figure 8.10: Angle- and spectrally-resolved TMRLE pattern at $B = 520\,\mathrm{mT}, T = 10\,\mathrm{K}$ for Sample 1. Left and right coloured panels correspond to measured and calculated $\rho(\hbar\omega, \theta)$-patterns, respectively. White dashed line in the calculated pattern follows the Wood's anomaly from Eq. (3.13). Side plots at the calculated pattern shows cross-sections along fixed photon energy $\hbar\omega = 1.671\,\mathrm{meV}$ as indicated by the dotted line (upper plot) or fixed angle $\theta = 10°$ as indicated by the dash-dotted line (right plot). Blue and red curves in these plots correspond to cross-sections of experimental data and calculation results, respectively.

these two diffraction orders at angles $\theta \leq \theta_{\mathrm{Wood}}$ as illustrated in Figure 8.11. Its shape predicted in Eq. (3.13) is represented by the two white dashed lines in the calculated two-dimensional panel of Figure 8.10 and shows ideal agreement with the expected shape. Additionally, the waves reflected from the sample backside contribute to the overall directionality, similar to the ones observed in Section 8.3. Also the weak effect strength at smaller emission angles is apparent. More precisely, the directionality strength is rather small with $\rho < -0.5\,\%$ for the angle range in between the Wood's anomaly. Additionally, the sign of the effect is negative for positive emission angles. Calling into mind the SPP-enhanced measurements reveals that photonic and plasmonic spin fluxes have inverse relative contribution. While for the small spacer Sample 2 mostly the SPP contributes to the directionality with positive sign for positive emission angle, in the large spacer Sample 1 the photonic effect with negative ρ for positive θ prevails. The evanescent SPP wave exponentially decays in the semiconductor which leads to the corresponding decrease of the SPP exciton interaction.

As discussed above, the non-resonant transverse spin and the plasmon transverse spin have inverse sign in this energy range. As one can see in Figure 8.2 the relative sign is energy-dependent, though. While for lower energies below the crossing point of the $\mathrm{SPP_R}$ and $\mathrm{SPP_L}$ branch the signs are the same, they are opposite above the crossing point. The situation we observe in the experiment corresponds to the latter one, with the exciton frequency being spectrally located slightly above the crossing point. Consequently, increasing the spacer thickness suppresses the plasmonic contribution which is substituted by the non-resonant one and the sign of directionality is reversed. Comparing the central parts of Figure 8.5 and Figure 8.10 visualizes this substantial difference of these two effects.

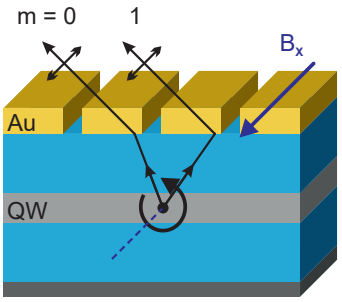

Figure 8.11: Diffraction at the grating causes interference of the beams corresponding to different orders ($m = 0, 1$), which takes place even for thick spacers. Figure adapted with permission from Reference [Spi18].

In summary it can be said that not only surface plasmon polaritons elicit directionality, though they lead to the strongest effect strength with about $\rho = 5\,\%$ at $B = 520\,\mathrm{mT}$ and $T = 10\,\mathrm{K}$. The far-field effects on the other hand show weaker effect strength and both show a strong oscillatory behaviour. Discussing the spectrally-integrated directionality shows an even more distinct picture. While the oscillatory patterns of the far-field contributions cancel each other out, the effect strength of SPP-enhanced directionality nearly persists. In other words, observing the structure at a non-zero emission angle by eye would mainly lead to a change of emitted colour for the far-field effects. The near-field effect on the other hand influences the overall intensity. Thus all approaches for establishing directionality might have their inherent use case.

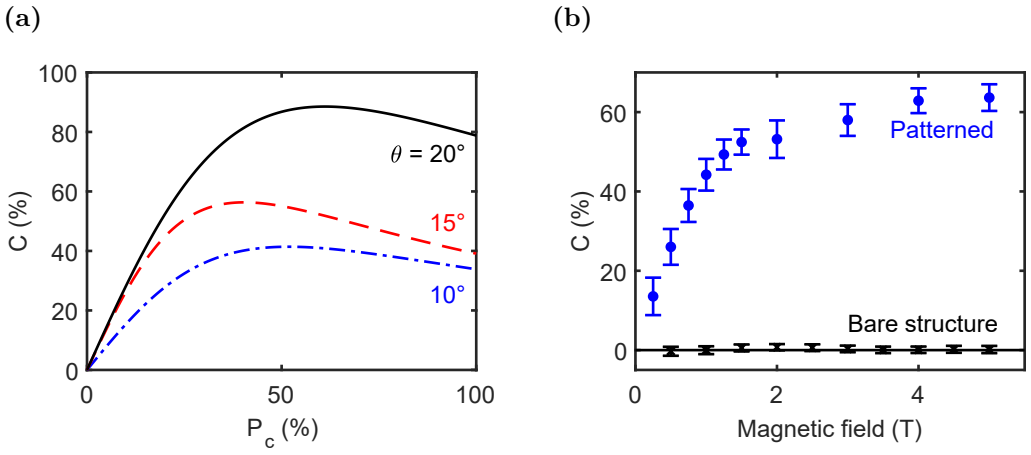

Figure 8.12: (a) Calculated directionality factor C as a function of the circular polarization degree P_c for the three emission angles 10° (dash-dotted blue line), 15° (dashed red line) and 20° (solid black line) with the parameters of Sample 2. **(b)** Experimental data of the directionality factor C as a function of magnetic field. The dependence is shown for Sample 2 on the bare structure (black crosses) and the plasmonic 250 nm grating (blue dots) at $\theta = 15°$ and $T = 2\,\mathrm{K}$. At each magnetic field step the intensities were first spectrally integrated before directionality was calculated. The error bars shown represent the standard deviation of several repetitions of the same experiment.

8.4 Dependence on Magnetic Field Strength

In Section 8.2 two different regimes were discussed, on the one hand the small Zeeman splitting regime in Subsection 8.2.4 at a rather low magnetic field of 520 mT and a slightly elevated temperature of 10 K. Here a directionality of about $|C| = 5\,\%$ could be observed on Sample 2. On the other hand in the large Zeeman splitting regime already briefly presented in Subsection 8.2.3 with a magnetic field of 1.5 T and 2 K temperature the directionality was boosted up to $|C| = 60\,\%$.

As discussed in Subsection 8.2.4, in the small Zeeman splitting regime the overlap of light and heavy hole wave functions $|\langle\Psi_{\mathrm{lh}}|\Psi_{\mathrm{hh}}\rangle|^2 \ll 1$ is reduced in the actual quantum well. In the large Zeeman splitting regime though, this discrepancy should be absent. Therefore the latter regime deserves a deeper examination, in order to clarify how the directionality factor depends on the magnetic field strength. As shown in Eq. (8.4) a maximum circular polarization degree of about 80 % can be expected at 5 T magnetic field. This regime can be reached only in the fixed angle setup using a liquid helium bath cryostat with superconducting magnet coils as presented in Section 7.2.

Figure 8.12a shows the theoretically predicted directionality strength C for p-polarized emission at three distinct angles $\theta = 10°$ to $20°$. All three curves are calculated for a fixed photon energy of $\hbar\omega = 1.67\,\text{eV}$. As one can see, very large values of up to 80 % are predicted at an emission angle of $\theta = 20°$ (solid black line) while for the 10° (dash-dotted blue line) and 15° angles the directionality reaches values of up to 40 % to 60 % respectively. Surprisingly, while for lower degrees of polarization the directionality raises linearly, at higher P_c it flattens before finally falling again. Naively one might have expected a Brillouin like function with a steep rise in directionality at low P_c and saturation at higher polarization degrees, which would not be a fully accurate description in this case. This might be related to the fact that the transverse SAM of the SPPs is less than unity as well as discussed in Subsection 5.2.

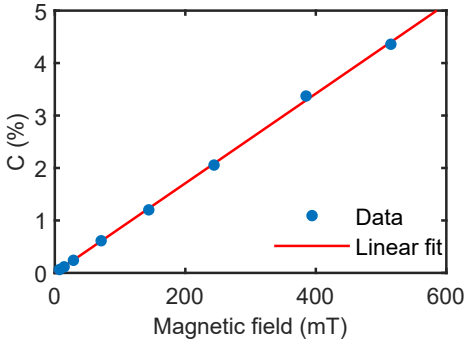

Figure 8.13: Dependence of directionality C on the magnetic field in Sample 2 at $T = 10\,\text{K}$ and $\theta = 10°$. The measurements have been performed on the plasmonic 250 nm grating and calculations are based on the spectrally-integrated intensities.

Now PL studies in this regime will be presented. These have been performed in order to ascertain that TMRLE can indeed reach such large values for the emission from strongly polarized excitons. In Figure 8.12b the experimental data for the magnetic field dependence is shown. Each data point in this graph represents the measured directionality at a fixed angle of $|\theta| = (15 \pm 3)°$ and $T = 2\,\text{K}$ on Sample 2. The measured intensities are spectrally integrated before calculating the directionality factor, thus yielding a more reliable basis for discussion of the overall effect strength. Data points on the bare part of the sample are represented in the plot by black crosses with error bars around the $C = 0$ line. As commented on in 8.3.2, the spectrally-integrated effect on the bare structure is even smaller due to the different interference fringes mitigating each other. Consequently the effect on the bare structure is confirmed negligible within this experiment.

Measurements in the plasmonic hybrid structure show a different picture. The data points of this measurement are represented by blue dots with error bars in Figure 8.12b. Here the directionality factor is boosted up to 60 % even for the spectrally-integrated intensities. This is also the saturation value, which is reached at magnetic fields of about 2 T. In other words, at positive magnetic field, the light intensity is four times stronger at 15° emission angle as compared to the same negative emission angle. This significant difference could already be observed in the spectrum in Figure 8.4a for 1.5 T of magnetic field. Remarkably enough both the observed enhancement of

directionality and its overall magnitude at a large magnetic field are in accordance with the theoretical calculations shown in Figure 8.12.

A verification of these measurements on the Fourier imaging spectroscopy setup shows a linear dependence in magnetic fields of up to 520 mT, as shown in Figure 8.13 by the following red solid line:

$$C_{\mathrm{fit}}(B) = \frac{B}{(11.70 \pm 0.08)\,\mathrm{T}}. \tag{8.12}$$

As the circular polarization degree P_{c} is expected to be linear in small magnetic fields (see Eq. (4.8)), also the directionality factor C should show a linear dependency. Thus, this result is in full accord with the theoretical predictions.

8.5 Excitation-Laser Intensity Dependence

The exciton emission needs to be properly polarized in order to show directionality. This polarization is achieved by applying an external magnetic field and by cooling down the quantum well structure. Hereby the Zeeman splitting is enhanced, which gives rise to the polarized emission. One additional factor was not discussed here so far: Observing emission from these structures requires energy to be deposited into them in some way. In case of the angular resolved setup (see Section 7.3) this is achieved by optical excitation with a 552 nm laser. The deposition of energy obviously might also lead to an increase in the temperature of the manganese system in these structures reducing its magnetization. In the following we will discuss if such a temperature increase is already taking place for the excitation intensity of $P = 3\,\mathrm{W/cm^2}$ used in most of the experiments.

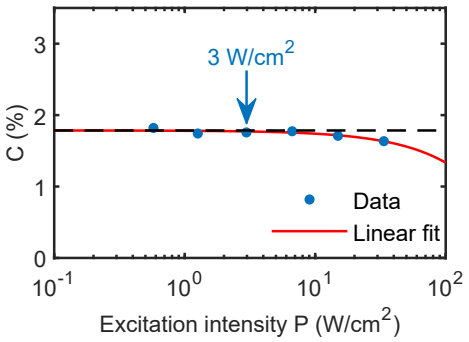

Figure 8.14: Dependence of directionality C on the excitation intensity (blue dots) with a linear fit (red solid line). At lower excitation intensities the effect strength is constant (black dashed line illustrates the offset from fit).

In order to quantify the influence of increased laser intensity on the strength of the directionality, C was measured as a function of the excitation intensity P. For each data point here the intensity was integrated spectrally and also the positive / negative angular half space was integrated before calculating the resulting directionality. Due to the integration the signal / noise ratio was significantly enhanced even at very low

excitation intensities yielding low signal strength. At the same time, the directionality strength is reduced due to this integration, as it shows the overall average effect.

The resulting dependence is depicted in Figure 8.14 as a semi-logarithmic plot with the data points shown as blue dots and the following linear fit represented by the red solid line:

$$C_{\text{fit}}(P) = (0.0179 \pm 0.0002) - (0.05 \pm 0.01)\,\frac{\text{cm}^2}{\text{kW}} \cdot P. \tag{8.13}$$

As one can see, at lower excitation intensities like the one used in the experiments, the dependence of the directionality on the laser intensity is negligible. The black dashed line illustrates the constant value of C in the low excitation intensity regime. In order to reduce the effect strength by a tenth, an excitation intensity of $40\,\text{W/cm}^2$ is necessary, which is more than one order of magnitude larger than the intensity used in our studies. Thus one can say that the manganese system is not heated by laser excitation at the intensities used here.

8.6 Temperature Dependence

In this section the dependence of directionality strength on the temperature is discussed. By decreasing the helium flow through the flow cryostat, the temperature at the heat exchanger can be adjusted. In order to keep the temperature constant at the desired level, a heater regulated by a PID controller is used. With increasing temperature of the structure, and consequently of the manganese system, its magnetization is reduced. This decrease can be observed in Figure 8.15, where the directionality is plotted as blue dots versus the heat exchanger temperature. Please note that the temperature of the sample is higher than the one measured at the heat exchanger.

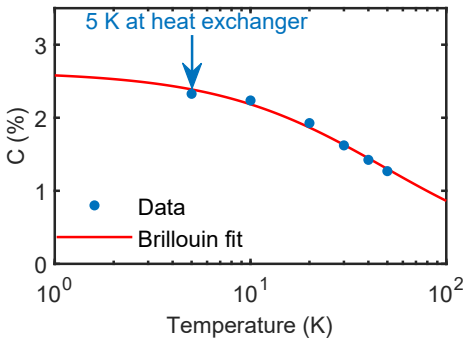

Figure 8.15: Temperature dependence of the directionality C. Angular resolved measurements are performed at 5 K temperature measured at the heat exchanger, corresponding to about 10 K at the sample.

The directionality was calculated from spectrally-integrated intensities at an emission angle range of $(10 \pm 1)°$. All measurements beyond this section were done at constant 5 K heat exchanger temperature, which is indicated in the graph and corresponds to about 10 K at the sample in this particular cryostat. For small P_c one could naively

expect the temperature dependence to directly follow the Zeeman splitting $\Delta_{\mathrm{h,F}}$ which was determined in Section 8.1, as it is linearly connected to the degree of polarization (see Eq. (8.3)), which in turn is linearly dependent on the directionality (see Figure 8.12a).

Indeed the dependence is well described within this temperature range by the following modified Brillouin function fit represented by the red solid line:

$$C_{\mathrm{fit}}(T) = C_0 B_{\frac{5}{2}}\left(\frac{A}{T_0 + T}\right). \tag{8.14}$$

Here $B_{\frac{5}{2}}$ is the Brillouin function (4.1) and $A = g_{\mathrm{Mn}}\mu_{\mathrm{B}}SB/k_{\mathrm{B}}$ depends only on the magnetic field strength and thus can be fixed at $A = 1.75\,\mathrm{K}$ for the given experimental parameters. The other two parameters were determined from the fit as $C_0 = 1.5 \pm 0.1$ and $T_0 = (49 \pm 5)\,\mathrm{K}$. As expected, with increasing temperature the directionality weakens due to the decreasing magnetization and polarization. By increasing the heat exchanger temperature from 5 K up to 50 K, the strength of directionality is halved. While qualitatively the fit agrees well with the experiment, the temperature offset T_0 from fit is higher than expected when considering only the anti-ferromagnetic type of interaction between the Mn ions [Gaj79] and the heat exchanger to sample holder rise. The dependence of the directionality strength on the temperature thus is subject to further studies and is not yet fully understood.

8.7 Emission from the Non-Magnetic Layers

In the emission spectra there is also some weak contribution from the GaAs substrate ($\hbar\omega \approx 1.53\,\mathrm{eV}$) and the (Cd,Mg)Te buffer/cap layer ($\hbar\omega \approx 2\,\mathrm{eV}$). Both materials are non-magnetic and in accordance with our expectations do not show directional emission within the precision of this experiment ($\rho < 10^{-4}$).

8.8 Summary of the Three Different Effects for Routing Emission

In this chapter we have studied three distinct implementations of a novel effect in hybrid plasmonic semiconductor nanostructures. This effect named transverse magnetic routing of light emission describes the preferential emission of light into a particular direction induced by a magnetic field. We quantify the TMRLE by the relative difference of the emission intensity and call this quantity directionality. The first two implementations are considered as far-field effects, which emerge due to

the interference of two different beam paths. The third manifestation of TMRLE is induced by the exponential decay of the evanescent surface plasmon polariton wave into the QW layer and the resulting coupling of the emission's transverse spin angular momentum to the wave vector of the evanescent wave. We could show that creating a higher Mn^{2+} magnetization by increasing the magnetic field while decreasing the temperature at the same time allows to boost the directionality by one order of magnitude to up to 60 %. This corresponds to a striking four-fold difference in emitted intensity comparing $+\theta$ and $-\theta$, visible by bare eye. The effect can be increased even further by optimizing the grating's period in order to fully match the SPP and excitonic resonances.

Simulations based on the scattering matrix method as well as analytic calculations reproduce the measured spectral- and angular-resolved directionality. The effect is linear in small magnetic fields in full accordance with the theoretical predictions. While the heating due to the excitation-laser is found to be negligible, a deliberate increase of the sample temperature decreases the directionality significantly. When detecting the s-polarized instead of the p-polarized emission, the directionality is absent. Also when detecting the emission from the non-magnetic (Cd,Mg)Te and GaAs layers the directionality is negligible. All in all, the results presented in this chapter demonstrate magnetically controllable directional emission in plasmonic diluted magnetic semiconductor nanostructures for the first time.

Chapter 9

Transverse Magneto-Optical Kerr Effect at Narrow Optical Resonances

This chapter will discuss the transverse magneto-optical Kerr effect (TMOKE), which emerges due to the Zeeman splitting of the electron levels within magnetic field. Some of the results presented in this chapter are published in similar form already in our recent paper [Bor19]. Similarly to the TMRLE presented in the previous chapter, also the TMOKE is sensitive to the in-plane magnetization orthogonal to the plane of light incidence and is usually studied in para- and ferromagnetic materials [Hub98; Kuc15; Kal16; Sol17]. While the widely used Faraday effect and polar Kerr effect are changing the polarization of the incident light, the TMOKE is an intensity effect defined by the relative change of the reflected intensity I for the two opposite directions of the in-plane magnetic field $\mathbf{B} \parallel \boldsymbol{x}$:

$$\delta = 2\frac{I(+B) - I(-B)}{I(+B) + I(-B)}. \tag{9.1}$$

The TMOKE detects modifications of the boundary conditions induced by the magnetic field and in this sense is valuable for the investigation of the magnetic properties a structure possesses near the studied interface [Hub98; Sol17]. Interestingly this can also be studied in transmission, even though TMOKE is usually studied in reflection. In order to observe TMOKE in transmission, the boundary conditions at the two interfaces of the magnetic layer are required to be different [Bon04].

9.1 TMOKE Spectrum of a Single Resonance

In Chapter 4 the magneto-optical effects were introduced with a focus on the transverse magneto-optical Kerr effect. We concluded that the TMOKE strength δ is rather small afar from optically active resonances, as a consequence of the negligible absorption in this range. The situation changes drastically if the TMOKE is observed

spectrally close to a resonance as presented recently by Pohl et al. [Poh13] who could show that the TMOKE is boosted up to $\delta = 13\,\%$ close to the SPP resonance. However, the SPP resonance is spectrally broad in contrast to an exciton resonance for example. In the following the general TMOKE properties in the vicinity of a single spectrally narrow optical resonance will be discussed. Then the experimental measurements at the light and heavy-hole excitonic resonance follow in Section 9.2. To that end we focus on a simplified magneto-optical model describing the electric dipole optical transitions in a three level quantum system. Such systems are realized in a large variety of solid-state, atomic and molecular objects with pseudo-spin in the ground or excited state[Fey57; Dzh97; Scu97]. We consider one example of such a system which is represented by a single ground state (g) coupled through the optical field to two excited states (e, with pseudo-spin projection $S_\mathrm{x} = \pm 1/2$). The latter are split due to the giant Zeeman effect by $\Delta/2$ from its prior energy position E_0 in magnetic field as discussed in Section 4.1. According to the selection rules for optical transitions, the excitation with an electromagnetic wave with σ^+ circular polarization in the yz-plane addresses the state with angular momentum projection $S_\mathrm{x} = +1/2$. Correspondingly σ^- polarized excitation addresses the $S_\mathrm{x} = -1/2$ state (see Figure 9.1). The Zeeman split energies E consequently read $E = \hbar\omega = E_0 \pm \Delta/2$. The relative permittivity tensor (4.10) for a single exciton resonance can be modelled by a Lorentz oscillator as already introduced in Eq. (2.8) with some modifications in the following way [Bor19]:

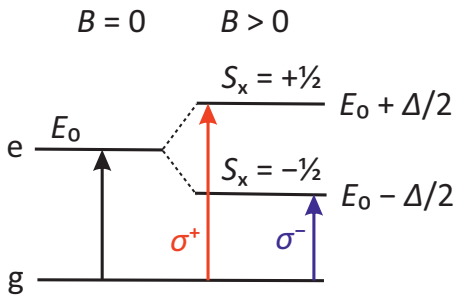

Figure 9.1: Scheme of a three-level system composed of ground (g) and two excited states (e) that are split by Δ due to the Zeeman effect in transverse magnetic field $\boldsymbol{B} \parallel \boldsymbol{x}$. The allowed optical transitions are σ^+ (red arrow) or σ^- (blue arrow) circular polarized in the yz-plane, depending on the respective pseudo-spin $S_\mathrm{x} = \pm 1/2$

$$\varepsilon_\mathrm{d} = \varepsilon_\mathrm{b}\left(1 + E_\mathrm{d}\frac{E_0 - E - \mathrm{i}\Gamma}{(E_0 - E - \mathrm{i}\Gamma)^2 - (\Delta/2)^2}\right) \quad \text{and} \tag{9.2a}$$

$$g = \frac{2\pi|\boldsymbol{d}|^2\Delta}{(E_0 - E - \mathrm{i}\Gamma)^2 - (\Delta/2)^2}, \tag{9.2b}$$

where $\boldsymbol{d}$ is the matrix element of the electron transition dipole moment, $E_d = 4\pi|\boldsymbol{d}|^2/\epsilon_\mathrm{b}$ is a dipole moment related energy and $\Gamma = \hbar\gamma$ is the linewidth of the exciton resonance and the damping in energy units simultaneously.

In the following we will consider the TMOKE in two regimes. The first regime, which we call the *weak coupling regime*, is observed when the Zeeman splitting Δ is smaller

as compared to the damping Γ and is frequently studied in a variety of experiments. Ferromagnetic metals are probably the most studied material, showing a typical value of $\rho \approx 10^{-3}$ and a weak spectral dependence within the visible and infrared spectral range [Kri67]. These materials were favoured in many cases with respect to dielectric materials, as these show only very weak off-resonant TMOKE in the transparency region, due to the negligible absorption. However, in the case of resonant TMOKE the situation is different showing a notable magnitude even in nearly transparent media when in the vicinity of the absorption band provided by different types of resonances. The second so called *strong coupling regime* is established if the Zeeman splitting Δ overcomes the damping Γ. In this case the exciton spin precession in magnetic field is faster with respect to the exciton damping Γ, which enables the observation of the Zeeman splitting immediately in the reflectivity spectrum.

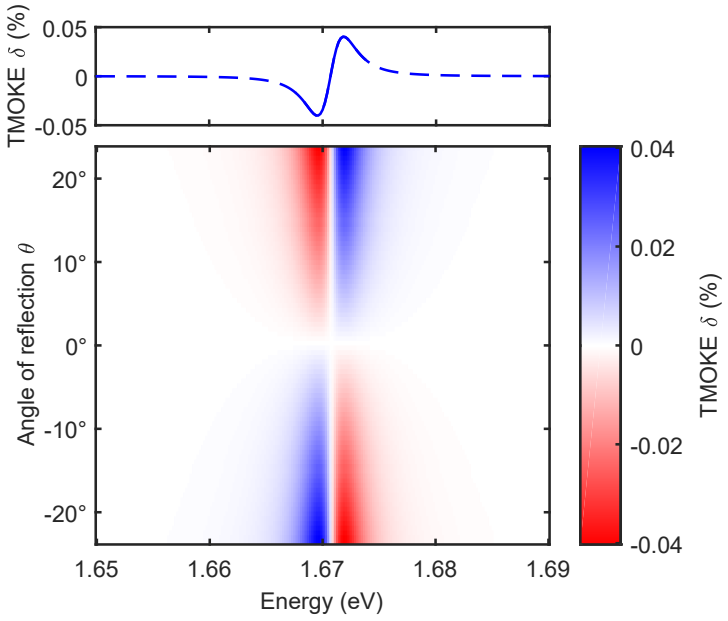

Figure 9.2: Exemplary TMOKE pattern in the weak coupling regime for $\varepsilon_\mathrm{b} = 10$, $\Delta = 0.2\,\mathrm{meV}$, $\Gamma = 2\,\mathrm{meV}$, $E_0 = 1.67\,\mathrm{eV}$ and $E_\mathrm{d} = 0.65\,\mathrm{meV}$ according to Eq. (9.3). The inset on top of the false colour image shows an one dimensional cut along the maximum angle. As emphasized by the solid part of the line, the TMOKE spectrum shows an S-shape, which changes sign at $\widetilde{E}$ and has two extrema separated by the damping Γ.

9.1.1 Weak Coupling Regime

In the weak coupling regime $\Delta/\Gamma \ll 1$ is presumed allowing some further simplifications, together with the assumption $\varepsilon_\mathrm{b} \gg \tan^2\theta$, which holds for all angles considered in experiment where $\tan^2\theta < 0.2$ and $\varepsilon_\mathrm{b} \approx 10$. As shown explicitly in Borovkova et al. [Bor19, Supplementary A] the Eq. (4.11) can be restated with the help of (9.2) in the form

$$\delta = -\frac{8E_\mathrm{d}\Delta}{\epsilon_\mathrm{b}-1}\frac{\widetilde{E}\Gamma}{[(\widetilde{E}+a)^2+\Gamma^2][(\widetilde{E}-a)^2+\Gamma^2]}\tan\theta, \tag{9.3}$$

where we introduce $a = E_\mathrm{d}/(2(\epsilon_\mathrm{b}-1))$ and $\widetilde{E} = (E_0 - E) + E_\mathrm{d} + a$ and θ is the angle of reflection shown in Figure 4.1. The corresponding TMOKE pattern in the weak coupling regime is shown in Figure 9.2 as false colour image. As one can see from Eq. (9.3) the TMOKE δ grows with $\tan\theta$ in this regime and its spectrum has an antisymmetric S-shape with respect to $\widetilde{E} = 0$. Furthermore the TMOKE minimum

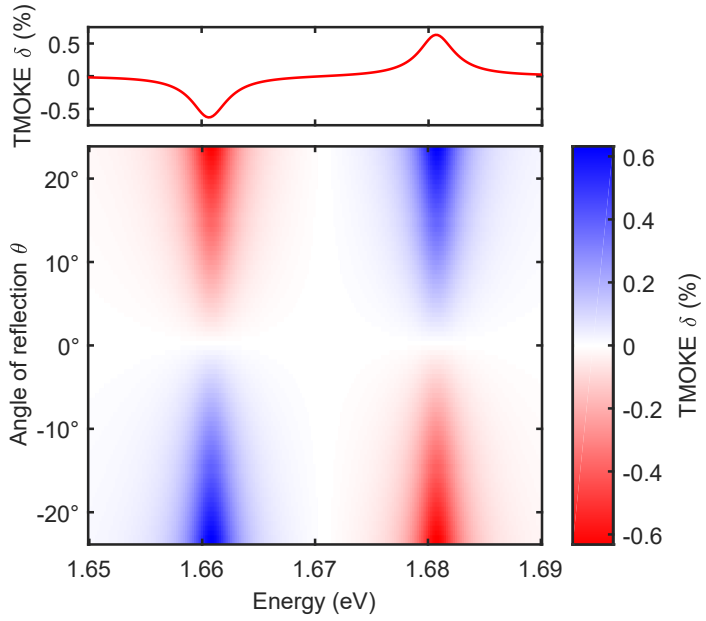

Figure 9.3: Exemplary TMOKE pattern in the strong coupling regime for $\varepsilon_\mathrm{b} = 10, \Delta = 20\,\mathrm{meV}, \Gamma = 2\,\mathrm{meV}, E_0 = 1.67\,\mathrm{eV}$ and $E_\mathrm{d} = 0.65\,\mathrm{meV}$ according to Eq. (9.5). The inset on top of the false colour image shows an one dimensional cut along the maximum angle. The TMOKE spectrum comprises two separate resonances, split by Δ. Please note also the different shape of the TMOKE spectrum, not showing an S-shape anymore.

and maximum are spectrally separated by the damping Γ with a magnitude

$$\delta = \mp \frac{3\sqrt{3} E_\mathrm{d} \Delta}{2(\epsilon_\mathrm{b} - 1)\Gamma^2} \tan\theta, \tag{9.4}$$

directly proportional to the Zeeman splitting Δ. The shape of the TMOKE spectrum on the other hand does not change with the magnetic field as long as $\Delta/\Gamma \ll 1$ holds.

9.1.2 Strong Coupling Regime

A second even more interesting regime is reached in the case of narrow optical resonances with respect to the Zeeman splitting and thus when $\Delta/\Gamma \gg 1$. TMOKE in this regime was not yet studied irrespective of the system presented here. Within the strong coupling regime the analytical expression for the magnitude of TMOKE

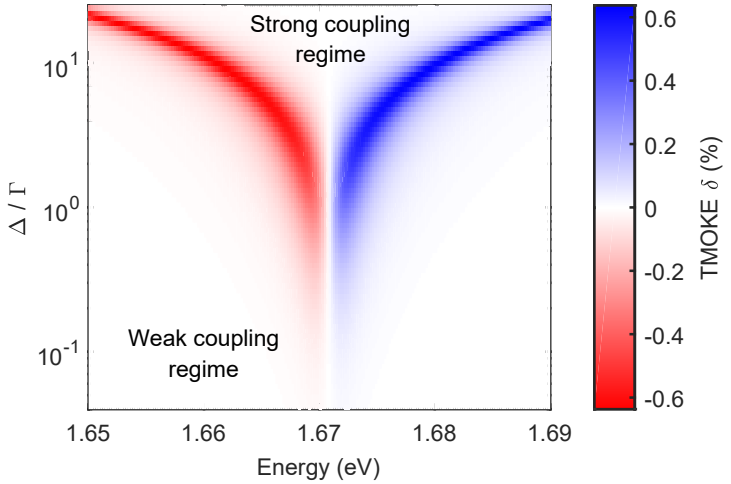

Figure 9.4: Exemplary TMOKE pattern comprising both the weak and strong coupling regime for $\varepsilon_\mathrm{b} = 10$, $\Delta/\Gamma = 0.04 - 25$, $\Gamma = 2\,\mathrm{meV}$, $E_0 = 1.67\,\mathrm{eV}$, $E_\mathrm{d} = 0.65\,\mathrm{meV}$ and $\theta = \arcsin(0.4) \approx 23°$ fixed at the maximum detectable angle in experiment.

extrema can be derived [Bor19] with the result that

$$\delta = \mp \frac{4\epsilon_\mathrm{b} E_d \tan\theta}{\Gamma} \frac{\epsilon_\mathrm{b}^2 - \epsilon_\mathrm{b} - \left(\frac{E_d}{2\Gamma}\right)^2}{\left(\epsilon_\mathrm{b}^2 - \epsilon_\mathrm{b} - \left(\frac{E_d}{2\Gamma}\right)^2\right)^2 + \left((2\epsilon_\mathrm{b} - 1)\frac{E_d}{2\Gamma}\right)^2}. \tag{9.5}$$

It can be seen that the magnitude of the extrema does not depend on the Zeeman splitting Δ anymore and thus has reached its saturation value. Contrary to the situation of weak coupling, here an increased magnetic field strength changes the shape of the TMOKE spectrum instead. As shown exemplary in Figure 9.3 the TMOKE spectrum comprises two separate peaks with opposite sign. In this regime the energy distance between these peaks is given by the Zeeman splitting Δ and thus depends on the magnetic field strength.

9.1.3 Comparison of Weak and Strong Coupling Regime

We will close this chapter with a summary of the two introduced regimes, which are condensed nicely in Figure 9.4. Here the TMOKE spectrum is shown at a fixed angle but for different ratios of Δ/Γ ranging from $\Delta/\Gamma = 1/25$ to 25. In the weak coupling regime where $\Delta/\Gamma \ll 1$ the TMOKE spectrum remains unchanged with two extrema split by Γ while the intensity increases linearly with Δ. This is still the case when Δ and Γ are on the same order of magnitude, until around $\Delta/\Gamma \approx 5$ [Bor19]. From

here on the strong coupling regime prevails where $\Delta/\Gamma \gg 1$ holds, which on the other hand comprises two separate TMOKE peaks at now saturated magnitude and spectrally split by Δ. In this regime only the spectrum changes but not the intensity δ, while in the weak coupling regime the situation was inverse. Even though for more complex systems additional peculiarities emerge, the general properties discussed above remain preserved.

9.2 Angular Resolved TMOKE Spectra at the Excitonic Resonances

Now the experimental observation of the TMOKE in these two regimes follows. To that end, the TMOKE mediated by excitons in a 10 nm thick (Cd,Mn)Te / (Cd,Mg)Te diluted magnetic semiconductor QW is investigated (For details see Table 6.1). In this structure, the 10 nm-thick DMS $Cd_{0.974}Mn_{0.026}Te$ QW layer is surrounded by the non magnetic $Cd_{0.73}Mg_{0.27}Te$ buffer and cap layer as barriers. The TMOKE is studied in the two regimes mentioned before:

1. The weak coupling regime is established in a magnetic field of $B = 580\,\mathrm{mT}$ while the sample is kept at a temperature of $T \approx 10\,\mathrm{K}$. Due to the relatively weak magnetic field also the Zeeman splitting Δ is small. We were able to acquire angle and spectrally resolved TMOKE spectra over a wide range of angles of reflection θ using a Fourier imaging setup (see Section 7.3).
2. The strong coupling regime with a varied magnetic field strength in 125 mT steps from 0.5 to 5.0 T while at constant 2 K temperature. The lower temperature and relatively high magnetic field strength result in a larger Zeeman splitting Δ, while the linewidth Γ remains about constant. In this case the measurements were performed for a fixed angle of reflection of $\theta = 5°$ as described in Section 7.2.

In both cases the sample was subject to a transverse magnetic field $\boldsymbol{B} \parallel \boldsymbol{x}$ oriented perpendicular to the plane of light incidence and thus being located in the QW plane (see Figure 4.1).

9.2.1 Weak Coupling Regime

In the beginning, we will discuss the reflection spectrum of excitonic states obtained on Sample 1b in the weak coupling regime, which is shown in Figure 9.5a. Strong oscillations in the reflection spectra of this structure (blue solid line) are present due to the interference of light reflected multiple times within the (Cd,Mg)Te buffer layer. While the reflection spectrum exhibits only a single exciton resonance originating

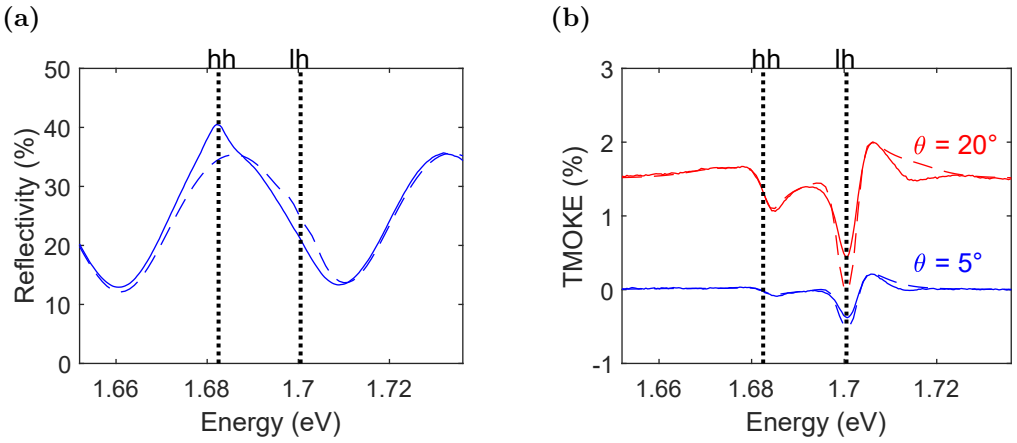

Figure 9.5: (a) Reflectivity spectrum from experiment (solid line) and simulations (dashed line) at an angle of reflection of $\theta = 5°$ and $T = 10\,\mathrm{K}$ on Sample 1b. **(b)** Two TMOKE spectra at different angle of reflection with $\theta = 5°$ shown in blue and 20° in red. Both measurements were taken at $B = 580\,\mathrm{mT}$ and $T = 10\,\mathrm{K}$ on Sample 1b. The solid lines refer to the experiment while the dashed lines correspond to the theory. For better visibility, the curves obtained at 20° were shifted upwards by 1.5 %.

from the DMS QW, represented by the weak feature at a photon energy of around 1.683 eV, the TMOKE spectrum shows a much more abundant picture. As shown in Figure 9.5b in the TMOKE spectrum two distinct resonances located at 1.683 eV and 1.701 eV are well resolved, highlighting the sensitivity of the TMOKE spectroscopy in comparison to ordinary reflection measurements.

In Subsection 4.1.2 we already briefly discussed the origin of these two resonances: The quantization of carriers inside the QW as well as uniaxial strain in the direction along the normal to the QW result in an energy level splitting of the light-hole and heavy-hole exciton resonances [Ivc05]. In a bulk crystal they are degenerate. For that reason two exciton resonances are present in the TMOKE spectrum of the DMS QW structure, with the light-hole (lh) state located at $E_{\mathrm{lh}}(B = 0) = 1.701\,\mathrm{eV}$ and the heavy-hole (hh) state observed at $E_{\mathrm{hh}}(B = 0) = 1.683\,\mathrm{eV}$. This results in a light-heavy hole splitting equal to $\Delta_{\mathrm{lh}} = 18\,\mathrm{meV}$. These energies are also marked in Figure 9.5a,b by the dotted vertical lines.

One should emphasize here that the light-hole exciton feature in the photoluminescence and reflectivity spectra was too weak to exactly determine the resonance position. This is mainly due to the fast relaxation into the ground state, which corresponds to the heavy-hole exciton. The TMOKE spectrum on the other hand reveals the positions of both exciton resonances and even more interestingly exhibits the about two times larger TMOKE strength for light-hole excitons as compared to the heavy-

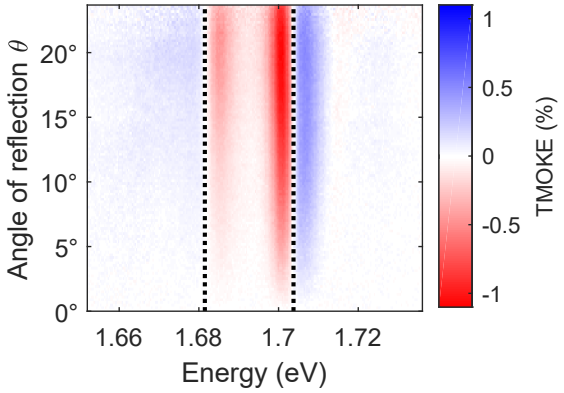

Figure 9.6: Angle resolved TMOKE spectrum in the exciton spectral range measured in the weak coupling regime at $B = 580\,\mathrm{mT}$ and $T = 10\,\mathrm{K}$ on Sample 1b. Please note that Δ/Γ is different for light- and heavy-hole contributions with 1.79 for the light and 0.5 for the heavy hole respectively. The dotted line marks the zero crossing of the TMOKE spectrum.

hole state. Also, the sign of the effect is opposite for the light and heavy-hole states. This is nicely observed in Figure 9.5b where for positive incidence angles θ the TMOKE magnitude for the lh exciton changes from positive to negative values with increasing photon energy E (rising S-shape). For the hh exciton the opposite behaviour with falling S-shape is observed. Already in the TMOKE spectrum of a single exciton resonance that was discussed based on simulations in Subsection 9.1.1 the TMOKE spectrum showed an antisymmetric S-shape.

As shown in Figure 9.6 the TMOKE δ ultimately reaches 1.1 % at $\theta = 20°$. Notably, this is several orders of magnitude larger as compared to the off-resonant reading of 0.01 % at $\theta = 20°$ and 1.578 eV. The heavy-hole excitons show a weaker TMOKE signal, as the corresponding transitions are linearly polarized in the QW plane in the absence of a magnetic field. Hence, they carry zero spin S_x along the direction of magnetic field. The heavy-hole TMOKE is only enabled due to the admixture of light-hole states within non-zero magnetic field, which is why it remains relatively weak until the Zeeman splitting Δ becomes comparable to the light and heavy-hole splitting Δ_{lh}. While this already hints at the origin of the different sign for light and heavy-hole TMOKE, a more intuitive explanation follows once we consider the strong coupling regime.

We will now proceed to the quantitative description of the TMOKE in the case of hybridized light and heavy-hole states within weak magnetic field. Therefore the effective permittivity tensor of the QW needs to be calculated. We neglect magnetic field induced orbital effects here, which can mix the light and heavy-hole resonances and thus induce spatial dispersion [Kot18] with respect to the stronger Mn-mediated

giant Zeeman splitting in DMS structures. In contrast to the single resonance scenario discussed in Section 9.1, here both light and heavy hole contribute to the resulting QW permittivity tensor in the following form:

$$\varepsilon_{\mathrm{d}} = \varepsilon_{\mathrm{b}}(1 + \chi_{\mathrm{lh}} + \chi_{\mathrm{hh}}), \tag{9.6}$$

with the light and heavy-hole susceptibilities χ_{lh} and χ_{hh} in the yz-subspace (and thus perpendicular to the magnetic field $\boldsymbol{B} \parallel \boldsymbol{x}$ with the y component oriented in the QW plane, see Figure 4.1).

As shown by Borovkova et al. [Bor19, Supplement B], the corresponding susceptibilities read:

$$\begin{aligned} \chi_{\mathrm{hh}} &= \frac{\hbar\omega_{\mathrm{LT}} D_{\mathrm{hh}}}{D_{\mathrm{hh},+} D_{\mathrm{hh},-}} \begin{pmatrix} \mathcal{Z}^2 & \mathrm{i}\mathcal{Z}/3 \\ -\mathrm{i}\mathcal{Z}/3 & 1 \end{pmatrix}, \\ \chi_{\mathrm{lh}} &= \frac{\hbar\omega_{\mathrm{LT}} D_{\mathrm{lh}}}{D_{\mathrm{lh},+} D_{\mathrm{lh},-}} \begin{pmatrix} \frac{4}{3} & -\frac{\mathrm{i}}{3}\left(\frac{E_{\mathrm{lh},-} - E_{\mathrm{lh},+}}{D_{\mathrm{lh}}} + \mathcal{Z}\right) \\ \frac{\mathrm{i}}{3}\left(\frac{E_{\mathrm{lh},-} - E_{\mathrm{lh},+}}{D_{\mathrm{lh}}} + \mathcal{Z}\right) & \frac{1}{3} \end{pmatrix}. \end{aligned} \tag{9.7}$$

Here, $D_\nu = E_\nu - E - \mathrm{i}\Gamma_\nu$ was introduced with the exciton resonance energy E_ν and width Γ_ν. The index $\nu = \mathrm{lh}, \mathrm{hh}, (\mathrm{lh}, \pm), (\mathrm{hh}, \pm)$ labels the zero-field and Zeeman-split excitonic transition energies, as shown also in Figure 4.3b where + corresponds to the energetically higher and − to the lower resonance respectively. Finally the effective longitudinal-transverse splitting is given by ω_{LT} and the parameter $\mathcal{Z}$ is determined by the ratio $\mathcal{Z} = \Delta_{\mathrm{h,F}}/\Delta_{\mathrm{lh}}$ introduced in Eq. (4.5) and (4.6). In the experimentally relevant case of $B = 580\,\mathrm{mT}$ it is about $|\mathcal{Z}| \approx 0.3$.

As already in the case of a single resonance the off-diagonal elements of the susceptibilities (9.7) elicit the TMOKE. We can observe two properties of the TMOKE signal already from these off-diagonal elements: Firstly, the sign before the element for light and heavy holes is different. This is confirmed in experiment by the different signs observed from their TMOKE responses. Secondly, the term $\propto (E_{\mathrm{lh},-} - E_{\mathrm{lh},+})/D_{\mathrm{lh}}$ shows that TMOKE is observed for light holes even when the mixing with the heavy holes is neglected, i.e. $\mathcal{Z} \to 0$. As one might expect, for heavy holes this is not the case. Note that even though the energy splitting of the exciton resonances is governed by the Zeeman splitting of both valence and conduction band, the mixing term $\mathcal{Z}$ is determined solely by the energy structure of the valence band states.

With the help of the transfer matrix method the reflectance and TMOKE spectrum was calculated for the actual multilayer DMS structure by Borovkova et al. [Bor19] with the QW described by Eq. (9.7). Good agreement with the experimental data is achieved assuming $E_{\mathrm{lh}} = 1.7005\,\mathrm{eV}$ and $E_{\mathrm{hh}} = 1.6825\,\mathrm{eV}$, as shown by the dashed curves in Figure 9.5. The value of longitudinal-transverse splitting used is $\hbar\omega_{\mathrm{LT}} =$

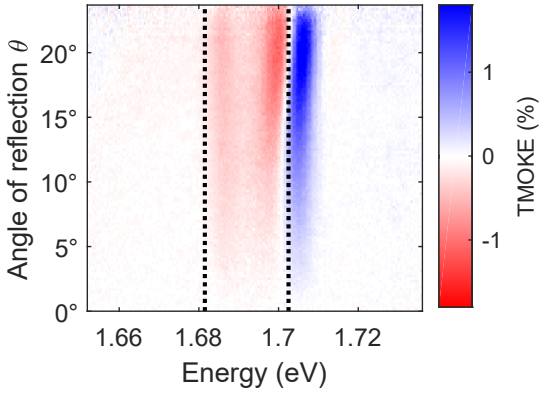

Figure 9.7: Angle resolved TMOKE spectrum in the exciton spectral range measured in the weak coupling regime at $B = 580\,\mathrm{mT}$ and $T = 10\,\mathrm{K}$ on Sample 3b. The dotted line marks the zero crossing of the TMOKE spectrum.

0.65 meV, the linewidth of both resonances is $\Gamma_{\mathrm{lh}} = \Gamma_{\mathrm{hh}} = 2.4\,\mathrm{meV}$ and the Zeeman splitting is $\Delta_{\mathrm{X,hh}} = 1.2\,\mathrm{meV}$ and $\Delta_{\mathrm{X,lh}} = 4.3\,\mathrm{meV}$. Thus, in the case of 580 mT external magnetic field, Δ and Γ are on the same order of magnitude and consequently the measurements shown in Figure 9.5b and 9.6 can be described within the weak coupling regime (see also Subsection 9.1.3).

9.2.2 Influence of the Cap Layer Thickness

Usually TMOKE is considered as a surface sensitive effect, which allows to analyse the upper layer of a magnetic material. Interestingly, confined quantum states can be formed not only near the sample surface, but also at some region in the bulk. In our case for example the states originate from the magnetic QW that is located inside a semiconductor structure covered by a cap layer. We now want to discuss also the influence of this cap layer thickness on the resulting TMOKE spectrum, which is why we study here another similar structure (Sample 3b) which differs from Sample 1b solely by the thickness of the cap layer. As a reminder, the cap layer thickness is only $h_{\mathrm{d}} = 30\,\mathrm{nm}$ in Sample 3b whereas it is 250 nm in Sample 1b. This structure is Sample 3b, which differs mostly in the more narrow cap layer thickness $h_{\mathrm{d}} = 30\,\mathrm{nm}$ as compared to Sample 1b with 250 nm. The resulting angle resolved TMOKE spectrum is shown in Figure 9.7. Please note that the TMOKE resonances appear not only at virtually the same position as compared to Figure 9.6, but also the sign of the resonances is the same. More precisely, the two S-shaped TMOKE resonances enclose the energy range showing negative TMOKE signal (i.e. the red domain around 1.69 eV). This indeed is to be expected as the composition and

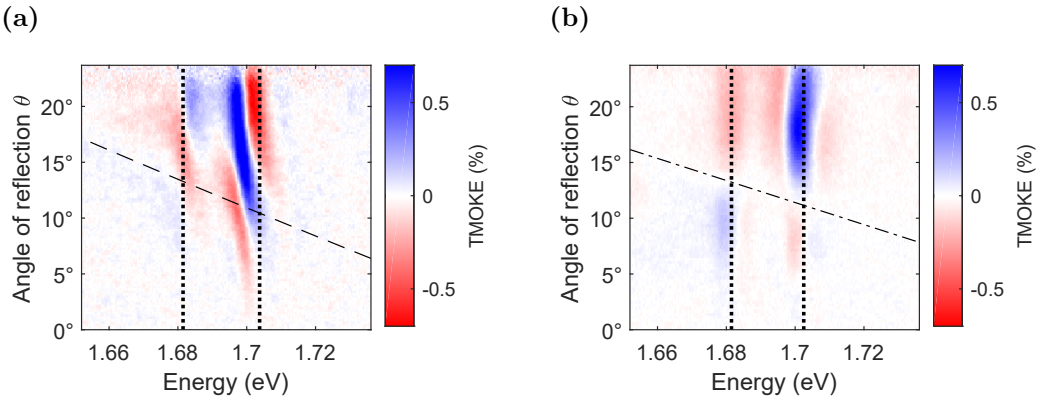

Figure 9.8: Angle resolved TMOKE spectrum in the exciton spectral range measured in the weak coupling regime at $B = 580\,\mathrm{mT}$ and $T = 10\,\mathrm{K}$ on **(a)** Sample 1 and **(b)** Sample 3 with plasmonic gratings of period 250 nm and 560 nm, respectively. The dotted lines represent the zero crossing of TMOKE $\delta = 0$ on the bare semiconductor structure (Sample 1b, 3b) for better orientation. The dashed line in (a) follows the Wood's anomaly (see also Figure 8.10), while the dash-dotted line in (b) is meant to guide the eye along the Au / air SPP resonance.

thickness of the (Cd,Mn)Te quantum well is approximately the same and thus also the light-heavy hole splitting remains unchanged. Interestingly, the variation of the cap layer thickness modifies the shape of the TMOKE resonance. While in the case of Sample 1b the positive TMOKE signal was clearly observed in the spectrum around 1.67 eV, this is not the case in this structure. Simulations reported by Borovkova et al. [Bor19] show how the TMOKE spectrum changes depending on the cap layer thickness, which may explain this surprising feature. Here it was shown that the shape of the TMOKE spectrum varies periodically with a period of half the light's wavelength in the cap layer (around 120 nm in this structure) and can even have a fully antisymmetric S-shape.

9.2.3 TMOKE and Evanescent Optical Fields

There is one more intriguing direction of our current research. In Chapter 8 we discussed how the exciton emission into the evanescent surface modes allows to control the direction of emission, due to their coupled transverse spin. For this reason it is interesting to study how these evanescent modes influence the TMOKE spectrum, when they cross the light and heavy-hole exciton spectral line. This is shown in Figure 9.8 for the two structures for which we already discussed the bare semiconductor TMOKE.

Let us begin with Sample 1 which is shown in Figure 9.8a, a structure patterned with a 250 nm plasmonic grating coupler. The additional dotted lines in the figure represent the TMOKE zero crossing $\delta = 0$ observed on Sample 1b (i.e. the same bare semiconductor) that was shown in Figure 9.6. If we recall the TMOKE pattern in the bare structure, we remember a TMOKE pattern which was nearly linearly increasing with the incidence angle without changing its shape and it showed a TMOKE pattern that was positive (blue) outside the dotted lines and negative (red) in between the TMOKE zero crossings. For low angles of reflection this is the case also on the patterned structure. For angles above 10°, the TMOKE drastically changes its shape. The dashed line in Figure 9.8a follows the Wood's anomaly that was already shown in the TMRLE measurements on the same sample in Figure 8.10. The experimental data seems to indicate that this Wood's anomaly is the origin of the altered TMOKE pattern. Note that above the Wood's anomaly around $\theta = 20°$ the TMOKE pattern is negative for higher (1.7 eV) and lower energies (red range around 1.66 eV) while it is positive for intermediate energies. Thus it appears that the TMOKE S-shape has changed its overall sign and also shifted to lower energies as seen from the right dotted line which is now located near the negative extremum of the TMOKE instead of its zero crossing. Also the overall TMOKE intensity decreased by roughly a factor of two.

A similarly rich behaviour is observed on Sample 3 with a 560 nm plasmonic grating as shown in Figure 9.8b. Again at lower angle of reflection, in between the TMOKE $\delta = 0$ zero crossing of light and heavy-hole resonances, the effect sign is the same as in the bare semiconductor Figure 9.7. In this case it is not the Wood's anomaly at which the TMOKE spectrum begins to change, but the Au / air SPP resonance shown as a guide to the eye by the dash-dotted line. In contrast to the case of the Wood's anomaly discussed above, immediately at the Au / air SPP resonance the TMOKE fully vanishes. For larger θ it seems to arise with the opposite sign, even though due to the resonances shift observed here as well, it is quite difficult to follow accurately. The TMOKE intensity in this case is also decreased by roughly a factor of two as observed on Sample 1. Gaining a deeper understanding of the processes which are involved near the crossing of evanescent optical fields and the excitonic resonances is one of the directions of our current experiments and calculations.

9.2.4 Strong Coupling Regime

Now we will proceed with the discussion of the strong coupling regime in Sample 1b, which is already reachable in magnetic fields of several Tesla, due to the quite narrow exciton resonances. For a sample temperature of $T < 2\,\mathrm{K}$ the ratio Δ/Γ exceeds 5 at around $B = 2\,\mathrm{T}$ and is about 10 at $B = 5\,\mathrm{T}$, thus granting the description within the

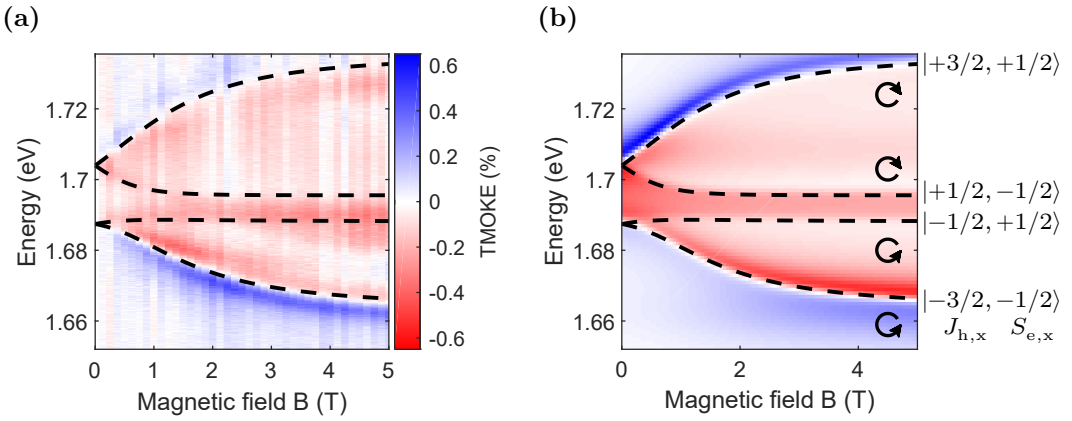

Figure 9.9: Exciton mediated TMOKE in the strong coupling regime $\Delta/\Gamma > 1$. Here **(a)** shows the measured and **(b)** the calculated TMOKE spectrum at fixed $\theta = 5°$ angle of reflection. The TMOKE is shown spectrally and magnetic field resolved at $T = 1.6\,\mathrm{K}$ on Sample 1b.

strong coupling regime. This is shown in Figure 9.9, where the dependence of the TMOKE spectrum on the external magnetic field is shown for field strength of up to 5 T at a fixed $\theta = 5°$ angle of reflection on Sample 1b. While at $B = 0$ two TMOKE resonances are present corresponding to heavy and light-hole excitons, for $\Delta/\Gamma \gg 1$ both resonant TMOKE features split into two resonances each. Remarkably, the TMOKE extrema are saturated already at $B = 1\,\mathrm{T}$ and remain constant afterwards in higher magnetic fields. Thus, in this regime the magnetic field influences only the shape of the TMOKE spectrum while the value of $\delta \approx 0.5\,\%$ is not further increased.

For the interpretation of the four branches in the TMOKE spectrum observed in higher magnetic fields, we should recall once again the details of giant Zeeman splitting in Voigt geometry (see especially Figure 4.3). Note that the weak and strong magnetic field cases are fundamentally different: At magnetic fields higher than 1 T the Zeeman splitting overcomes the light-heavy hole splitting ($\mathcal{Z} \gg 1$) and a simple qualitative picture can be considered which is realized also in a bulk (Cd,Mn)Te crystal. The Zeeman-split electron states in Voigt configuration ($\boldsymbol{B} \parallel \boldsymbol{x}$) are characterized by the spin projection $S_{\mathrm{e,x}} = \pm 1/2$, thus representing a doublet. The valence band states in contrast are split into a quartet with the Zeeman split energy governed by the total angular momentum projection on the magnetic field direction $J_{\mathrm{h,x}} = \pm 1/2, \pm 3/2$. In the weak magnetic field case on the other hand, the quantization axis is given by the QW confinement potential. Therefore, the energies of the valence band states are mainly determined by the normal projection of the angular momentum $J_{\mathrm{h,z}} = \pm 1/2, \pm 3/2$ for light and heavy holes, respectively.

Let us discuss the splittings of conduction and valence band states when neglecting confinement. In this case the splittings are given by $\Delta_\mathrm{e} = 2N_0\alpha x \left|S_{\mathrm{e,x}}\right| B_S$ and $\Delta_\mathrm{h} = -\frac{2}{3}N_0\beta x \left|J_{\mathrm{e,x}}\right| B_S$, respectively and we obtain four σ polarized exciton transitions. The largest energy splitting is achieved between the outer heavy-hole like components $\Delta_\mathrm{out} = \Delta_h + \Delta_e$, corresponding to the excitonic states $|\pm 3/2, \pm 1/2\rangle$ written in the $|J_{\mathrm{h,x}}, S_{\mathrm{e,x}}\rangle$ notation. For the inner components the splitting is smaller and can be described by $\Delta_\mathrm{in} = \Delta_\mathrm{h}/3 - \Delta_\mathrm{e}$ corresponding to the exciton resonances $|\pm 1/2, \mp 1/2\rangle$ which are light-hole like. More precisely, the outer splitting $\Delta_\mathrm{out} \approx 70\,\mathrm{meV}$ is about 8 times larger than Δ_in at $B = 5\,\mathrm{T}$, as follows from Figure 9.9.

Considering the $s-d$ and $p-d$ exchange constants in bulk (Cd,Mn)Te leads to the conclusion that the relation $\Delta_\mathrm{out} > \Delta_\mathrm{in} > 0$ holds [Gaj10]. In this case the two optical transitions with lower energy $|-3/2, -1/2\rangle$ and $|-1/2, +1/2\rangle$ are σ^+ polarized in the yz-plane, while the higher energy transitions $|+3/2, +1/2\rangle$ and $|+1/2, -1/2\rangle$ have opposite σ^- polarization (see also Figure 4.3). As the TMOKE is sensitive to the transverse spin component, we expect the TMOKE shape to change along with the transverse spin of the studied transition. This agrees well with the form of the S-shaped TMOKE spectrum at large magnetic field: For the low energy exciton transitions at 1.666 and 1.688 eV it has a rising slope with increasing energy and it changes to falling for the higher energy resonances at 1.696 and 1.733 eV. This does also explain the opposite sign of the light and heavy-hole TMOKE resonances, which are already observed in the weak coupling regime (Figure 9.6).

As shown by Borovkova et al. [Bor19, Supplement B], the susceptibilities in this $\Delta \gg \Gamma$ regime can be simplified to a compact antisymmetric form reading

$$\chi_{hh} = \frac{\hbar\omega_\mathrm{LT}}{6}\begin{pmatrix} U_\mathrm{hh} & -\mathrm{i}W_\mathrm{hh} \\ \mathrm{i}W_\mathrm{hh} & U_\mathrm{hh} \end{pmatrix} \quad \text{and} \quad \chi_{lh} = \frac{\hbar\omega_\mathrm{LT}}{2}\begin{pmatrix} U_\mathrm{lh} & \mathrm{i}W_\mathrm{lh} \\ -\mathrm{i}W_\mathrm{lh} & U_\mathrm{lh} \end{pmatrix}. \tag{9.8}$$

We introduced the diagonal term $U_\nu = \frac{1}{D_{\nu,+}} + \frac{1}{D_{\nu,-}}$ and the off diagonal term $W_\nu = \frac{1}{D_{\nu,+}} - \frac{1}{D_{\nu,-}}$ where $\nu = \mathrm{lh}, \mathrm{hh}$. This allows to calculate the resonance position of the four exciton states versus the magnetic field as shown by the dashed curves in Figure 9.9 and satisfactorily describes the experimental TMOKE spectra for large magnetic fields. Please note that the TMOKE also experiences saturation within this model at higher magnetic fields.

9.3 Summary of TMOKE in Weak and Strong Coupling Regime

In conclusion, in this chapter we have studied the TMOKE in the vicinity of narrow optical resonances. For the first time, two distinct regimes of the TMOKE were

introduced and demonstrated. The regimes are distinguished by the ratio of the Zeeman splitting with respect to the resonance linewidth. On the one hand, in the weak coupling regime ($\Delta < \Gamma$) we observe a linearly increasing TMOKE magnitude with respect to the Zeeman splitting and the S-shaped TMOKE spectrum does not change. In the strong coupling regime ($\Delta > \Gamma$) on the other hand the TMOKE magnitude experiences saturation and its spectrum is strongly modified due to the Zeeman splitting, which results in the appearance of two separate TMOKE peaks for both the light and the heavy-hole resonance. One can extract rich information on the energy structure and selection rules for optical transitions from the spectral dependence of the TMOKE peaks and the sign of δ. The second regime was accessible due to the narrow line width of the excitonic resonance in combination with the giant Zeeman splitting in diluted magnetic semiconductor nanostructures. Furthermore the change of the TMOKE spectrum in the vicinity of the surface plasmon polariton resonance and the Wood's anomaly was presented.

Chapter 10

Conclusions

In this thesis the transverse magnetic routing of light emission (TMRLE) was introduced and experimentally demonstrated as a fundamentally new magneto-optical effect. Also a so far unstudied regime of the transverse magneto-optical Kerr effect (TMOKE) was investigated at narrow optical resonances. Both presented magneto-optical effects result in a modification of the emitted / reflected intensity of light, which is controlled by the magnetic field. The studies were performed on excitons in 10 nm-thick diluted magnetic semiconductor quantum well structures as the model system, consisting of a (Cd,Mn)Te quantum well and a (Cd,Mg)Te barrier.

The TMRLE was introduced in Chapter 8 and describes the routing of exciton emission, controlled by a transverse magnetic field. Here, the magnetic field modifies the optical selection rules and induces an elliptical polarization of the exciton transitions perpendicular to the quantum well plane. With increasing magnetic field a transverse spin angular momentum of the emission arises and the emission becomes directional. We were able to observe three different mechanisms that give rise to this directionality, which are shown in Figure 10.1. All three mechanisms require a non-mirror symmetric sample structure in the growth direction. We distinguish between the near-field effect described in Section 8.2 and the far-field effects studied in Section 8.3. The first far-field effect (Figure 10.1a) occurs even in a bare quantum well, where the directional emission of $C \approx 0.1\,\%$ is attributable to the interference of directly emitted light and the light reflected at the substrate. In the second far field effect (Figure 10.1b) a structure covered with a plasmonic grating and relatively large quantum well to grating distance is studied. A directionality of $C \approx 1\,\%$ is induced by interference of the zeroth and first diffraction order. The strongest directionality is observed due to the near-field effect (Figure 10.1c), which takes place in similar structures with a smaller spacer thickness separating the quantum well (QW) and plasmonic grating. In this case the directionality of the emission is stronger with $C \approx 5\,\%$ and it takes place due to strong spin-momentum locking of the emission and the surface waves. We were able to further increase the directionality of emission in the near

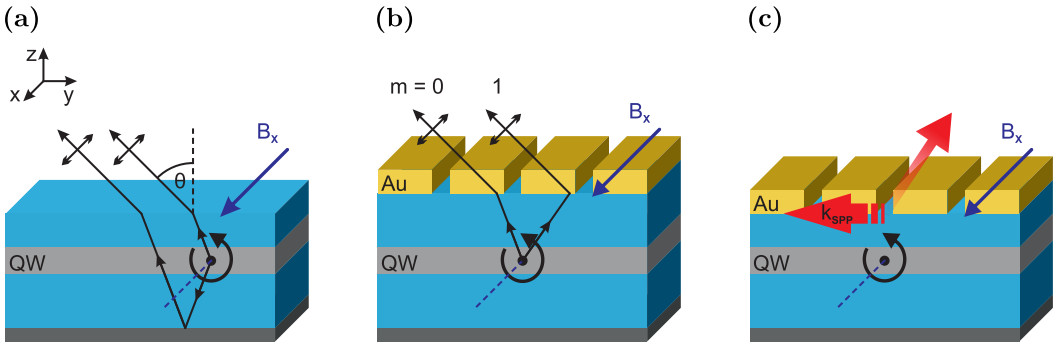

Figure 10.1: Main mechanisms of the transverse magnetic routing of light emission. **(a)** Interference of the directly emitted and the reflected electromagnetic waves. The reflection occurs at the substrate. **(b)** Interference of the zeroth and first diffraction order beams which are transmitted through the grating. The interfering beams propagate along the same direction in free space outside the sample as they originate from the same dipole. **(c)** Exciton emission into the evanescent (sub-wavelength) optical modes at the interface of semiconductor and metal. Figure adapted with permission from Reference [Spi18].

field by the following two approaches: First, an optimization of the grating period allows to match the surface plasmon polariton and excitonic resonances, resulting in about 50 % stronger directionality compared to the 250 nm period used in our prior experiments. Second, an increase of the Mn^{2+} polarization results in a higher transverse spin angular momentum of the exciton emission. This immediately leads to a stronger directionality and allowed to observe up to $C \approx 60\,\%$, a four-fold difference in the emitted intensity for the opposite directions of magnetic field – observable by bare eye.

The concept of TMRLE is quite novel as it was discovered within the scope of this thesis and thus further interesting studies of this effect are most likely to follow. The realization of magnetic field controlled routing at elevated temperatures would be an aspiring next step. Materials like InSb and (Hg,Cd)Te with an intrinsically large Zeeman splitting as well as novel two-dimensional ferromagnetic materials [Sey18] might enable such implementations.

The allowed optical transitions and their polarization are given by the optical selection rules, which apply already on the level of individual emitters. The TMRLE relies on the polarization of these transitions which remains unchanged also for an ensemble of emitters. For that reason the TMRLE is inherently robust to inhomogeneous broadening and thus interesting for elevated temperature applications [Spi18]. Another pioneering task could be the ultra-fast control of emission with up to terahertz rates by optical and radio-frequency fields that manipulate the magnetization of the magnetic Mn^{2+} ions. Also the magnetic environment of a single emitter might

be accurately probed, providing that it is properly positioned within the hybrid plasmonic semiconductor crystal. In a final step, magnetically-tunable chiral quantum networks might be realized which are required for applications in quantum optical devices [Lod17].

In Chapter 9 the TMOKE at narrow optical resonances was discussed, which describes the influence of a transverse magnetic field on the intensity of light reflected from a structure. The studied optical resonances originate from quantum well excitons and possess a relatively narrow linewidth Γ as compared to other optical resonances like the surface plasmon polariton for example. The quantum well structure consists of a diluted magnetic semiconductor and therefore allows to achieve large values of exciton Zeeman splitting Δ already in moderate magnetic fields. For the first time the combination of a narrow linewidth Γ and a large splitting Δ allowed to experimentally observe the TMOKE in two distinct regimes. The two regimes are distinguished by the ratio of the Zeeman splitting with respect to the resonance linewidth: First, the weak coupling regime where $\Delta < \Gamma$ is introduced in Subsection 9.2.1. In this regime the Zeeman splitting cannot be seen in the reflectivity spectrum, as it is smaller compared to the damping. The TMOKE spectrum shows two S-shaped resonances in this regime, corresponding to the light and heavy hole exciton. Due to the opposite transverse spin of these two resonances, also the TMOKE has opposite sign. In the weak coupling regime, the TMOKE intensity increases linearly with the Zeeman splitting Δ, while the distance of the extrema is given by the resonance linewidth Γ for each of the two resonances. Also, the influence of evanescent optical fields on the TMOKE spectrum was studied, which seems to invert the TMOKE sign and causes a spectral resonance shift. Second, the so far unstudied strong coupling regime was introduced in Subsection 9.2.4 where $\Delta > \Gamma$. Here, the spin precession in a magnetic field is faster than the exciton damping Γ and the Zeeman splitting overcomes the exciton resonance linewidth. Thus, the exciton Zeeman splitting may be observed in reflectivity within the strong coupling regime. The TMOKE intensity experiences saturation and thus no longer depends on the Zeeman splitting Δ in this regime. Instead it defines the TMOKE resonance position and thus the spectral dependence that comprises two separate TMOKE resonances each for the light and the heavy hole transition.

The presented results have several implications in fundamental and applied optics. First of all, the resonant TMOKE in the strong coupling regime may be utilized as a spectroscopic tool enabling the investigation of the energy structure of electronic states involved in optical transitions. We could also show that the TMOKE does not only depend on the surface properties of a structure, but can also be used to study confined resonances in a layer buried below the surface and in this context may even be tailored by varying the thickness of the cap layer. We experimentally demonstrated the phenomena in this thesis at the exciton resonances in a 10 nm-thick

(Cd,Mn)Te / (Cd,Mg)Te diluted magnetic semiconductor quantum well structure. However the observations are not restricted to this very system but can be transferred to different material systems. To take a single example, the optical resonances of rare-earth ions in dielectric materials are quite narrow as well so that $\Gamma \leq \Delta$ is achieved already in moderate magnetic fields. The rare-earth ions in orthoborates for instance provide lines with $\Delta/\Gamma \approx 1$ in $B \approx 1\,\mathrm{T}$ [Fuk01; Kan11; Yag16]. Further narrow lines in the visible and infrared spectra were also demonstrated in other magnetical and non-magnetical systems [Dig01; Vin03; Agr08; Pop09; Bor15]. Finally, the resonant TMOKE allows to read out the system's in-plane magnetization and thus may be used for possible applications in quantum information and sensing technologies[Web10; Dya17]. Usually the polarization rotation observed for the Faraday effect or polar magneto-optical Kerr effect (PMOKE) are used to assess the spin dynamics in semiconductors [Bud94]. These however allow to observe only the spin component which is oriented parallel to the direction of light propagation ($\boldsymbol{B} \parallel \boldsymbol{k}$). The TMOKE, on the other hand, grants access to the perpendicular component of the magnetization and thus the combination of TMOKE and PMOKE may provide the possibility for performing spin tomography.

All in all, the results presented in this thesis could pave the way for controllable directional emission both for classical and quantum emitters with temporal and spatial resolution, which is of fundamental significance for nanoscale optics.

Part V

Appendix

Acknowledgements

I would like to express my deep gratitude to everyone who encouraged and supported me during the creation of this work.
I would like to thank *Prof. Manfred Bayer* for his dedication to science that led among other things to the International Collaborative Research Center (TRR 160) and to my opportunity to work within this project. Owing to the positive working atmosphere between the various lab teams and the superb equipment it was a great fun to perform my research at his chair.
I am especially thankful to my supervisor *Dr. Ilya A. Akimov* who excellently routed me throughout the years of my master and PhD theses. Whenever I had questions, he had an open door for me and helped me with his great experience and knowledge about experimental physics. I was glad to have the chance to work under his supervision and would always take that decision again.
I want to thank *Prof. Dmitri R. Yakovlev* for his feedback concerning paper revision and for arranging the russian language class led by his wive *Luba A. Yakovleva*, which thanks to her was always enjoyable and enabled me to understand Cyrillic.
Due to the collaboration with the Ioffe institute, I had the opportunity to go to St. Petersburg for several months and work under the supervision of *Prof. Victor F. Sapega* in the group of *Prof. Yury G. Kusrayev*. I would like to thank all the colleagues I met there, who made this such a pleasant time for me. I want to mention also *Dr. Alexander N. Poddubny* who supported not only our work a lot by his theoretical input, but also helped me handle the numerous administrative affairs when travelling to Russia. Living there in *Ulitsa Butlerova 40a* together with *Dr. Matthias Salewski*, *Janina Rautert* and *Erik Kirstein* was undoubtedly a great time.
In Dortmund I learned a lot from *Dr. Lars E. Kreilkamp*, *Dr. Manuel Jäckl* and *Dr. Martin Pohl* who introduced me to the various experimental setups in our laboratory and instructed me during the time of my master thesis. The work in the laboratory would have been only half as much fun without them and my dear colleagues *Jonas Vondran*, *Lars Klompmaker*, *Alexander N. Kosarev*, *Dr. Sergey V. Poltavtsev* and *Markus Kuhnert*. In this context, I want to thank *all colleagues of E2* for the wonderful atmosphere during fruitful discussions and intermittent coffee breaks. I am grateful to *Michaela Wäscher*, *Nina Collette* and *Katharina Sparka* for their administrative support and patience especially when still not knowing the correct Warengruppe after five years at the chair and *Lars Wieschollek*, *Thomas Stöhr*, *Klaus Wiegers* and *Daniel Tüttmann* for the steady flow of liquid helium and technical support.
I am happy to have found *Sören Kreinberg*, *Stephan Melzer*, *Dr. Benedikt Nowak*, *Philipp Sicking*, *Arne Meyer auf der Heide*, *Dr. Andreas Gisen* and all members of the *Schwafelrunde* as good friends already in my early years in Dortmund.

A special thanks goes to my *proof readers* for screening one or more chapters of my thesis for spelling inconsistencies.

On a final note, I want to thank *Laura*, my parents *Gerda* and *Rüdiger*, my sister *Julia* with *Ida* and my brother *Daniel*, for their patience, love and support in every moment of my life.

List of Publications

[1] **F. Spitzer**, A. N. Poddubny, I. A. Akimov, V. F. Sapega, L. Klompmaker, L. E. Kreilkamp, L. V. Litvin, R. Jede, G. Karczewski, M. Wiater, T. Wojtowicz, D. R. Yakovlev, and M. Bayer. "Routing the emission of a near-surface light source by a magnetic field". In: *Nature Physics* 14.10 (2018), pp. 1043–1048. DOI: 10.1038/s41567-018-0232-7.

[2] O. V. Borovkova, **F. Spitzer**, V. I. Belotelov, I. A. Akimov, A. N. Poddubny, G. Karczewski, M. Wiater, T. Wojtowicz, A. K. Zvezdin, D. R. Yakovlev, and M. Bayer. "Transverse magneto-optical Kerr effect at narrow optical resonances". In: *Nanophotonics* 8.2 (2019), pp. 287–296. DOI: 10.1515/nanoph-2018-0187.

[3] **F. Spitzer**, B. A. Glavin, V. I. Belotelov, J. Vondran, I. A. Akimov, S. Kasture, V. G. Achanta, D. R. Yakovlev, and M. Bayer. "Enhancement of electron hot spot relaxation in photoexcited plasmonic structures by thermal diffusion". In: *Physical Review B* 94.20 (2016), p. 201118. DOI: 10.1103/PhysRevB.94.201118.

[4] S. A. Dyakov, **F. Spitzer**, I. A. Akimov, D. A. Yavsin, S. I. Pavlov, S. Y. Verbin, S. G. Tikhodeev, N. A. Gippius, A. B. Pevtsov, and M. Bayer. "Transverse Magneto-Optical Kerr Effect in Magnetite Covered by Array of Gold Nanostripes". In: *Semiconductors* 52.14 (2018), pp. 1857–1860. DOI: 10.1134/S1063782618140099.

Conference Contributions

1. DPG Spring Meeting, Berlin, Germany, 2015:
   Contributed talk about "Surface plasmon polariton induced shortening of the optical response in perforated gold films"

2. 2nd internal SFB / TRR 142 workshop, Bad Sassendorf, Germany, 2015:
   Contributed poster about "Optical properties of guided CdZnTe structures"

3. 3rd internal SFB / TRR 142 workshop, Dortmund, Germany, 2015:
   Contributed talk about "Exciton polaritons in CdMgTe / CdZnTe waveguides"

4. PLMCN, Nara, Japan, 2016:
   Contributed poster about "Exciton polaritons in CdMgTe / CdZnTe waveguides"

5. DPG Spring Meeting, Regensburg, Germany, 2016:
   Contributed talk about "Enhancement of electron hot spot relaxation in photoexcited plasmonic structures by thermal diffusion"

6. Semiconductor Seminar, St. Petersburg, Russia, 2016:
   Contributed talk about "Enhancement of electron hot spot relaxation in photoexcited plasmonic structures by thermal diffusion"

7. CMD26, Groningen, The Netherlands, 2016:
   Contributed talk about "Enhancement of electron hot spot relaxation in photoexcited plasmonic structures by thermal diffusion"

8. Low Dimensional Seminar, St. Petersburg, Russia, 2017:
   Contributed talk about "Magnetic field control of photonic wheels for directional emission"

9. Jaszowiev, Szczyrk, Poland, 2017:
   Contributed poster about "Exciton-assisted TMOKE in CdMnTe / CdMgTe quantum well structures"

10. PLMCN, Würzburg, Germany, 2017:
    Contributed poster about "Exciton-assisted TMOKE in CdMnTe / CdMgTe quantum well structures"

11. DPG Spring Meeting, Berlin, Germany, 2018:
    Contributed talk about "Exciton interaction with surface plasmon polaritons in hybrid metal-semiconductor nanostructures"

12. ICRC TRR 160 workshop, Dortmund, Germany, 2018:
    Contributed poster about: "Magneto-optical effects in emission and reflection in CdMnTe / CdMgTe quantum well structures"
13. HBSM 2018, Moskau, Russia, 2018:
    Contributed talk about: "Magnetic field control of directional emission in a CdMnTe / CdMgTe quantum well"

Acronyms

BIG	bismuth iron garnet
CCD	charge-coupled device
(Cd,Mg)Te	cadmium magnesium telluride
(Cd,Mn)Te	cadmium manganese telluride
DMS	diluted magnetic semiconductor
EuS	europium sulphide
FEM	free electron model
(Hg,Cd)Te	mercury cadmium telluride
hh	heavy-hole
InSb	indium antimony
lh	light-hole
LMOKE	longitudinal magneto-optical Kerr effect
LSP	localized surface plasmon
NP	nano-particle
NSOM	near-field scanning optical microscopy
MBE	molecular beam epitaxy
MO	microscope objective
PC	plasmonic crystal
PID	proportional-integral-derivative
PL	photoluminescence
PMOKE	polar magneto-optical Kerr effect
QW	quantum well
SAM	spin angular momentum
SEM	scanning electron microscopy

SERS	surface-enhanced Raman scattering
SHG	second harmonic generation
SiO_2	silicon dioxide
S-matrix	scattering matrix
SPP	surface plasmon polariton
TE	transverse electric polarization
TM	transverse magnetic polarization
TMOKE	transverse magneto-optical Kerr effect
TMRLE	transverse magnetic routing of light emission
WL	white light

Bibliography

[Agr08] G. P. Agrawal. *Applications of nonlinear fiber optics*. 2. ed. Burlington, MA: Academic Press, 2008. ISBN: 978-0123743022.

[Aie15] A. Aiello, P. Banzer, M. Neugebauer, and G. Leuchs. "From transverse angular momentum to photonic wheels". In: *Nature Photonics* 9.12 (2015), pp. 789–795. DOI: 10.1038/nphoton.2015.203.

[Aki12] I. A. Akimov, V. I. Belotelov, A. V. Scherbakov, M. Pohl, A. N. Kalish, A. S. Salasyuk, M. Bombeck, C. Brüggemann, A. V. Akimov, R. I. Dzhioev, V. L. Korenev, Y. G. Kusrayev, V. F. Sapega, V. A. Kotov, D. R. Yakovlev, A. K. Zvezdin, and M. Bayer. "Hybrid structures of magnetic semiconductors and plasmonic crystals: a novel concept for magneto-optical devices [Invited]". In: *Journal of the Optical Society of America B* 29.2 (2012), A103. DOI: 10.1364/JOSAB.29.00A103.

[Ame17] V. Amendola, R. Pilot, M. Frasconi, O. M. Maragò, and M. A. Iatì. "Surface plasmon resonance in gold nanoparticles: a review". In: *Journal of physics. Condensed matter : an Institute of Physics journal* 29.20 (2017), p. 203002. DOI: 10.1088/1361-648X/aa60f3.

[And97] R. André and S. Le Dang. "Low-temperature refractive indices of Cd1−xMnxTe and Cd1−yMgyTe". In: *Journal of Applied Physics* 82.10 (1997), pp. 5086–5089. DOI: 10.1063/1.366383.

[Ank08] J. N. Anker, W. P. Hall, O. Lyandres, N. C. Shah, J. Zhao, and R. P. van Duyne. "Biosensing with plasmonic nanosensors". In: *Nature materials* 7.6 (2008), pp. 442–453. DOI: 10.1038/nmat2162.

[Arm13] G. Armelles, A. Cebollada, A. García-Martín, and M. U. González. "Magnetoplasmonics: Combining Magnetic and Plasmonic Functionalities". In: *Advanced Optical Materials* 1.1 (2013), pp. 10–35. DOI: 10.1002/adom.201200011.

[Ash13] N. W. Ashcroft and N. D. Mermin. *Festkörperphysik*. 4., verb. Aufl. München: Oldenbourg, 2013. ISBN: 978-3486713015.

[Asp86] D. E. Aspnes, S. M. Kelso, R. A. Logan, and R. Bhat. "Optical properties of Al x Ga 1− x As". In: *Journal of Applied Physics* 60.2 (1986), pp. 754–767. DOI: 10.1063/1.337426.

[Ban13] P. Banzer, M. Neugebauer, A. Aiello, C. Marquardt, N. Lindlein, T. Bauer, and G. Leuchs. "The photonic wheel - demonstration of a state of light with purely transverse angular momentum". In: *Journal of the European Optical Society: Rapid Publications* 8 (2013). DOI: 10.2971/jeos.2013.13032.

[Bar03] W. L. Barnes, A. Dereux, and T. W. Ebbesen. "Surface plasmon subwavelength optics". In: *Nature* 424.6950 (2003), pp. 824–830. DOI: 10.1038/nature01937.

[Bau14] T. Bauer, S. Orlov, U. Peschel, P. Banzer, and G. Leuchs. "Nanointerferometric amplitude and phase reconstruction of tightly focused vector beams". In: *Nature Photonics* 8.1 (2014), pp. 23–27. DOI: 10.1038/nphoton.2013.289.

[Bek15] A. Y. Bekshaev, K. Y. Bliokh, and F. Nori. "Transverse Spin and Momentum in Two-Wave Interference". In: *Physical Review X* 5.1 (2015), p. 465. DOI: 10.1103/PhysRevX.5.011039.

[Bel11] V. I. Belotelov, I. A. Akimov, M. Pohl, V. A. Kotov, S. Kasture, A. S. Vengurlekar, A. V. Gopal, D. R. Yakovlev, A. K. Zvezdin, and M. Bayer. "Enhanced magneto-optical effects in magnetoplasmonic crystals". In: *Nature nanotechnology* 6.6 (2011), pp. 370–376. DOI: 10.1038/nnano.2011.54.

[Bel13] V. I. Belotelov, A. N. Kalish, and A. K. Zvezdin. "Magneto-Optics of Plasmonic Crystals". In: *Magnetophotonics*. Ed. by M. Inoue, M. Levy, and A. V. Baryshev. Vol. 178. Springer Series in Materials Science. Berlin, Heidelberg: Springer Berlin Heidelberg, 2013, pp. 51–106. DOI: 10.1007/978-3-642-35509-7_4.

[Ben11] O. Benson. "Assembly of hybrid photonic architectures from nanophotonic constituents". In: *Nature* 480.7376 (2011), pp. 193–199. DOI: 10.1038/nature10610.

[Ber05] S. Berciaud, L. Cognet, P. Tamarat, and B. Lounis. "Observation of intrinsic size effects in the optical response of individual gold nanoparticles". In: *Nano letters* 5.3 (2005), pp. 515–518. DOI: 10.1021/nl050062t.

[Bli12] K. Y. Bliokh and F. Nori. "Transverse spin of a surface polariton". In: *Physical Review A* 85.6 (2012). DOI: 10.1103/PhysRevA.85.061801.

[Bli15a] K. Y. Bliokh, F. J. Rodríguez-Fortuño, F. Nori, and A. V. Zayats. "Spin–orbit interactions of light". In: *Nature Photonics* 9.12 (2015), pp. 796–808. DOI: 10.1038/nphoton.2015.201.

[Bli15b] K. Y. Bliokh, D. Smirnova, and F. Nori. "Quantum spin Hall effect of light". In: *Science (New York, N.Y.)* 348.6242 (2015), pp. 1448–1451. DOI: 10.1126/science.aaa9519.

[Bon04] N. Bonod, R. Reinisch, E. Popov, and M. Nevière. "Optimization of surface-plasmon-enhanced magneto-optical effects". In: *Journal of the Optical Society of America B* 21.4 (2004), p. 791. DOI: 10.1364/JOSAB.21.000791.

[Bor15] E. Y. Borovikova, K. N. Boldyrev, S. M. Aksenov, E. A. Dobretsova, V. S. Kurazhkovskaya, N. I. Leonyuk, A. E. Savon, D. V. Deyneko, and D. A. Ksenofontov. "Crystal growth, structure, infrared spectroscopy, and luminescent properties of rare-earth gallium borates RGa3(BO3)4, R=Nd, Sm–Er, Y". In: *Optical Materials* 49 (2015), pp. 304–311. DOI: 10.1016/j.optmat.2015.09.021.

[Bor16] O. Borovkova, A. Kalish, and V. Belotelov. "Transverse magneto-optical Kerr effect in active magneto-plasmonic structures". In: *Optics letters* 41.19 (2016), pp. 4593–4596. DOI: 10.1364/OL.41.004593.

[Bor18] O. V. Borovkova, H. Hashim, M. A. Kozhaev, S. A. Dagesyan, A. Chakravarty, M. Levy, and V. I. Belotelov. "TMOKE as efficient tool for the magneto-optic analysis of ultra-thin magnetic films". In: *Applied Physics Letters* 112.6 (2018), p. 063101. DOI: 10.1063/1.5012873.

[Bor19] O. V. Borovkova, F. Spitzer, V. I. Belotelov, I. A. Akimov, A. N. Poddubny, G. Karczewski, M. Wiater, T. Wojtowicz, A. K. Zvezdin, D. R. Yakovlev, and M. Bayer. "Transverse magneto-optical Kerr effect at narrow optical resonances". In: *Nanophotonics* 8.2 (2019), pp. 287–296. DOI: 10.1515/nanoph-2018-0187.

[Bos16] D. Bossini, V. I. Belotelov, A. K. Zvezdin, A. N. Kalish, and A. V. Kimel. "Magnetoplasmonics and Femtosecond Optomagnetism at the Nanoscale". In: *ACS Photonics* 3.8 (2016), pp. 1385–1400. DOI: 10.1021/acsphotonics.6b00107.

[Bud94] B. Buda, M. Dahl, N. von Truchsess, and A. Waag. "Polar magneto-optic Kerr effect in (Cd,Mn)Te/CdTe superlattices". In: *Journal of Crystal Growth* 138.1-4 (1994), pp. 652–655. DOI: 10.1016/0022-0248(94)90886-9.

[Bur86] J. J. Burke, G. I. Stegeman, and T. Tamir. "Surface-polariton-like waves guided by thin, lossy metal films". In: *Physical Review B* 33.8 (1986), pp. 5186–5201. DOI: 10.1103/PhysRevB.33.5186.

[Che14] A. L. Chekhov, V. L. Krutyanskiy, A. N. Shaimanov, A. I. Stognij, and T. V. Murzina. "Wide tunability of magnetoplasmonic crystals due to excitation of multiple waveguide and plasmon modes". In: *Optics express* 22.15 (2014), pp. 17762–17768. DOI: 10.1364/OE.22.017762.

[Chi13] J. Y. Chin, T. Steinle, T. Wehlus, D. Dregely, T. Weiss, V. I. Belotelov, B. Stritzker, and H. Giessen. "Nonreciprocal plasmonics enables giant enhancement of thin-film Faraday rotation". In: *Nature communications* 4 (2013), p. 1599. DOI: 10.1038/ncomms2609.

[Col16] R. J. Coles, D. M. Price, J. E. Dixon, B. Royall, E. Clarke, P. Kok, M. S. Skolnick, A. M. Fox, and M. N. Makhonin. "Chirality of nanophotonic waveguide with embedded quantum emitter for unidirectional spin transfer". In: *Nature communications* 7 (2016), p. 11183. DOI: 10.1038/ncomms11183.

[Cou17] R. Courtland. "Intel Now Packs 100 Million Transistors in Each Square Millimeter". In: *IEEE Spectrum* (30 Mar 2017). URL: https://spectrum.ieee.org/nanoclast/semiconductors/processors/intel-now-packs-100-million-transistors-in-each-square-millimeter.

[Dig01] M. J. F. Digonnet, ed. *Rare-earth-doped fiber lasers and amplifiers*. 2. ed., rev. and expanded. Vol. 71. Optical engineering. New York, NY: Marcel Dekker, 2001. ISBN: 0824704584.

[Dya17] M. I. Dyakonov. *Spin Physics in Semiconductors*. Vol. 157. Cham: Springer International Publishing, 2017. DOI: 10.1007/978-3-319-65436-2.

[Dzh97] R. I. Dzhioev, H. M. Gibbs, E. L. Ivchenko, G. Khitrova, V. L. Korenev, M. N. Tkachuk, and B. P. Zakharchenya. "Determination of interface preference by observation of linear-to-circular polarization conversion under optical orientation of excitons in type-II GaAs/AlAs superlattices". In: *Physical Review B* 56.20 (1997), pp. 13405–13413. DOI: 10.1103/PhysRevB.56.13405.

[Fab16] E. Di Fabrizio, S. Schlücker, J. Wenger, R. Regmi, H. Rigneault, G. Calafiore, M. West, S. Cabrini, M. Fleischer, N. F. van Hulst, M. F. Garcia-Parajo, A. Pucci, D. Cojoc, C. A. E. Hauser, and M. Ni. "Roadmap on biosensing and photonics with advanced nano-optical methods". In: *Journal of Optics* 18.6 (2016), p. 063003. DOI: 10.1088/2040-8978/18/6/063003.

[Fan41] U. Fano. "The Theory of Anomalous Diffraction Gratings and of Quasi-Stationary Waves on Metallic Surfaces (Sommerfeld's Waves)". In: *Journal of the Optical Society of America* 31.3 (1941), p. 213. DOI: 10.1364/JOSA.31.000213.

[Far46] M. Faraday. "Experimental Researches in Electricity. Nineteenth Series". In: *Philosophical Transactions of the Royal Society of London* 136.0 (1846), pp. 1–20. DOI: 10.1098/rstl.1846.0001.

[Far99] M. Faraday and P. Day. *The philosopher's tree: A selection of Michael Faraday's writings*. Bristol u.a: Inst. of Physics, 1999. ISBN: 0-7503-0570-3.

[Fer11] E. Ferreiro-Vila, M. Iglesias, E. Paz, F. J. Palomares, F. Cebollada, J. M. González, G. Armelles, J. M. García-Martín, and A. Cebollada. "Magneto-optical and magnetoplasmonic properties of epitaxial and polycrystalline Au/Fe/Au trilayers". In: *Physical Review B* 83.20 (2011), p. 2135. DOI: 10.1103/PhysRevB.83.205120.

[Fey57] R. P. Feynman, F. L. Vernon, and R. W. Hellwarth. "Geometrical Representation of the Schrödinger Equation for Solving Maser Problems". In: *Journal of Applied Physics* 28.1 (1957), pp. 49–52. DOI: 10.1063/1.1722572.

[Flo17] D. Floess, M. Hentschel, T. Weiss, H.-U. Habermeier, J. Jiao, S. G. Tikhodeev, and H. Giessen. "Plasmonic Analog of Electromagnetically Induced Absorption Leads to Giant Thin Film Faraday Rotation of 14°". In: *Physical Review X* 7.2 (2017). DOI: 10.1103/PhysRevX.7.021048.

[Fuk01] K. Fukui, H. Ogasawara, I. Harada, and A. Kotani. "Magnetic circular dichroism of resonant X-ray emission spectra at L edges of rare-earth compounds". In: *Journal of Synchrotron Radiation* 8.2 (2001), pp. 407–409. DOI: 10.1107/S0909049500015569.

[Fur88] J. K. Furdyna. "Diluted magnetic semiconductors". In: *Physical Review B* 64.4 (1988), R29–R64. DOI: 10.1063/1.341700.

[Gaj10] J. A. Gaj and J. Kossut. *Introduction to the Physics of Diluted Magnetic Semiconductors*. Vol. 144. Berlin, Heidelberg: Springer Berlin Heidelberg, 2010. DOI: 10.1007/978-3-642-15856-8.

[Gaj78] J. A. Gaj, R. R. Gałazka, and M. Nawrocki. "Giant exciton Faraday rotation in Cd1−xMnxTe mixed crystals". In: *Solid State Communications* 25.3 (1978), pp. 193–195. DOI: 10.1016/0038-1098(78)91477-1.

[Gaj79] J. A. Gaj, R. Planel, and G. Fishman. "Relation of magneto-optical properties of free excitons to spin alignment of Mn2+ ions in Cd1−xMnxTe". In: *Solid State Communications* 29.5 (1979), pp. 435–438. DOI: 10.1016/0038-1098(79)91211-0.

[Gan09] J. K. Gansel, M. Thiel, M. S. Rill, M. Decker, K. Bade, V. Saile, G. von Freymann, S. Linden, and M. Wegener. "Gold helix photonic metamaterial as broadband circular polarizer". In: *Science (New York, N.Y.)* 325.5947 (2009), pp. 1513–1515. DOI: 10.1126/science.1177031.

[Gie09] H. Giessen and R. Vogelgesang. "Glimpsing the weak magnetic field of light". In: *Science (New York, N.Y.)* 326.5952 (2009), pp. 529–530. DOI: 10.1126/science.1181552.

[Gon07] J. B. González-Díaz, A. García-Martín, G. Armelles, J. M. García-Martín, C. Clavero, A. Cebollada, R. A. Lukaszew, J. R. Skuza, D. P. Kumah, and R. Clarke. "Surface-magnetoplasmon nonreciprocity effects in noble-metal/ferromagnetic heterostructures". In: *Physical Review B* 76.15 (2007), p. 153402. DOI: 10.1103/PhysRevB.76.153402.

[Gra10] D. K. Gramotnev and S. I. Bozhevolnyi. "Plasmonics beyond the diffraction limit". In: *Nature Photonics* 4.2 (2010), pp. 83–91. DOI: 10.1038/nphoton.2009.282.

[Gri14] D. J. Griffiths. *Introduction to electrodynamics*. 4. ed., new internat. ed. Always learning. Harlow: Pearson, 2014. ISBN: 9781292021423.

[Gru06] M. Grundmann. *The physics of semiconductors: An introduction including devices and nanophysics*. Berlin and New York: Springer, 2006. ISBN: 354025370X.

[Hen13] M. Henini, ed. *Molecular Beam Epitaxy: From research to mass production*. Amsterdam: Elsevier, 2013. DOI: 10.1016/C2010-0-68986-3.

[Hen16] M. Hentschel, B. Metzger, B. Knabe, K. Buse, and H. Giessen. "Linear and nonlinear optical properties of hybrid metallic-dielectric plasmonic nanoantennas". In: *Beilstein journal of nanotechnology* 7 (2016), pp. 111–120. DOI: 10.3762/bjnano.7.13.

[Hen17] M. Hentschel, M. Schäferling, X. Duan, H. Giessen, and N. Liu. "Chiral plasmonics". In: *Science advances* 3.5 (2017), e1602735. DOI: 10.1126/sciadv.1602735.

[Hic87] R. K. Hickernell and D. Sarid. "Long-range surface magnetoplasmons in thin nickel films". In: *Optics letters* 12.8 (1987), p. 570. DOI: 10.1364/OL.12.000570.

[Hon16] G. Honorio. "Winkel- und wellenlängenaufgelöste Spektroskopie einer Quantentopf-Probe (CdMnTe) aus II-VI Halbleitern". Bachelorarbeit. TU Dortmund, 2016.

[Hub98] A. Hubert and R. Schäfer. *Magnetic domains: The analysis of magnetic microstructures*. Berlin: Springer, 1998. ISBN: 978-3-540-64108-7.

[Ign16] D. O. Ignatyeva, G. A. Knyazev, P. O. Kapralov, G. Dietler, S. K. Sekatskii, and V. I. Belotelov. "Magneto-optical plasmonic heterostructure with ultranarrow resonance for sensing applications". In: *Scientific reports* 6 (2016), p. 28077. DOI: 10.1038/srep28077.

[Ino13] M. Inoue, M. Levy, and A. V. Baryshev, eds. *Magnetophotonics*. Springer Series in Materials Science. Berlin, Heidelberg: Springer Berlin Heidelberg, 2013. DOI: 10.1007/978-3-642-35509-7.

[Ivc05] E. L. Ivchenko. *Optical spectroscopy of semiconductor nanostructures*. Harrow: Alpha Science Internat, 2005. ISBN: 1-84265-150-1.

[Jah16] M. Jahn, S. Patze, I. J. Hidi, R. Knipper, A. I. Radu, A. Mühlig, S. Yüksel, V. Peksa, K. Weber, T. Mayerhöfer, D. Cialla-May, and J. Popp. "Plasmonic nanostructures for surface enhanced spectroscopic methods". In: *The Analyst* 141.3 (2016), pp. 756–793. DOI: 10.1039/C5AN02057C.

[Joh72] P. B. Johnson and R. W. Christy. "Optical Constants of the Noble Metals". In: *Physical Review B* 6.12 (1972), p. 4370. DOI: 10.1103/PhysRevB.6.4370.

[Jun13] C. Junge, D. O'Shea, J. Volz, and A. Rauschenbeutel. "Strong coupling between single atoms and nontransversal photons". In: *Physical review letters* 110.21 (2013), p. 213604. DOI: 10.1103/PhysRevLett.110.213604.

[Kal16] A. N. Kalish and V. I. Belotelov. "Magneto-optical effects for detection of in-plane magnetization in plasmonic crystals". In: *Physics of the Solid State* 58.8 (2016), pp. 1563–1572. DOI: 10.1134/S1063783416080163.

[Kan11] Z. Kang, Y. Zhang, H. Menkara, B. K. Wagner, C. J. Summers, W. Lawrence, and V. Nagarkar. "CdTe quantum dots and polymer nanocomposites for x-ray scintillation and imaging". In: *Applied Physics Letters* 98.18 (2011), p. 181914. DOI: 10.1063/1.3589366.

[Kap14] P. V. Kapitanova, P. Ginzburg, F. J. Rodríguez-Fortuño, D. S. Filonov, P. M. Voroshilov, P. A. Belov, A. N. Poddubny, Y. S. Kivshar, G. A. Wurtz, and A. V. Zayats. "Photonic spin Hall effect in hyperbolic metamaterials for polarization-controlled routing of subwavelength modes". In: *Nature communications* 5 (2014), p. 3226. DOI: 10.1038/ncomms4226.

[Kau12] M. Kauranen and A. V. Zayats. "Nonlinear plasmonics". In: *Nature Photonics* 6.11 (2012), pp. 737–748. DOI: 10.1038/NPHOTON.2012.244.

[Ker77] J. Kerr. "XLIII. On rotation of the plane of polarization by reflection from the pole of a magnet". In: *The London, Edinburgh, and Dublin Philosophical Magazine and Journal of Science* 3.19 (1877), pp. 321–343. DOI: 10.1080/14786447708639245.

[Khu15] J. B. Khurgin. "How to deal with the loss in plasmonics and metamaterials". In: *Nature nanotechnology* 10.1 (2015), pp. 2–6. DOI: 10.1038/nnano.2014.310.

[Klo17] L. Klompmaker. "Magnetische Kontrolle der Emissionsrichtung photolumineszenter Strahlung einer plasmonischen Halbleiterprobe". Masterarbeit. TU Dortmund, 2017.

[Kot18] L. V. Kotova, V. N. Kats, A. V. Platonov, V. P. Kochereshko, R. André, and L. E. Golub. "Magnetospatial dispersion of semiconductor quantum wells". In: *Physical Review B* 97.12 (2018), p. 593. DOI: 10.1103/PhysRevB.97.125302.

[Kre13] L. E. Kreilkamp, V. I. Belotelov, J. Y. Chin, S. Neutzner, D. Dregely, T. Wehlus, I. A. Akimov, M. Bayer, B. Stritzker, and H. Giessen. "Waveguide-Plasmon Polaritons Enhance Transverse Magneto-Optical Kerr Effect". In: *Physical Review X* 3.4 (2013). DOI: 10.1103/PhysRevX.3.041019.

[Kre68] E. Kretschmann and H. Raether. "Notizen: Radiative Decay of Non Radiative Surface Plasmons Excited by Light". In: *Zeitschrift für Naturforschung A* 23.12 (1968). DOI: 10.1515/zna-1968-1247.

[Kri67] G. S. Krinchik and V. A. Artem'ev. "Magneto-Optical Properties of Ni, Co and Fe in the UV, Visible, and Infrared Parts of the Spectrum". In: *Zh. Eksp. Teor. Fiz.* 53 (1967), pp. 1901–1912.

[Kuc15] W. Kuch, R. Schäfer, P. Fischer, and F. U. Hillebrecht. *Magnetic Microscopy of Layered Structures*. Vol. 57. Berlin, Heidelberg: Springer Berlin Heidelberg, 2015. DOI: 10.1007/978-3-662-44532-7.

[Kuh94] B. Kuhn-Heinrich, W. Ossau, E. Bangert, A. Waag, and G. Landwehr. "Zeeman pattern of semimagnetic (CdMn)Te/(CdMg)Te quantum wells in inplane magnetic fields". In: *Solid State Communications* 91.6 (1994), pp. 413–418. DOI: 10.1016/0038-1098(94)90776-5.

[Lef15] Y. Lefier and T. Grosjean. "Unidirectional sub-diffraction waveguiding based on optical spin-orbit coupling in subwavelength plasmonic waveguides". In: *Optics letters* 40.12 (2015), pp. 2890–2893. DOI: 10.1364/OL.40.002890.

[Ley07] C. Leyder, M. Romanelli, J. P. Karr, E. Giacobino, T. C. H. Liew, M. M. Glazov, A. V. Kavokin, G. Malpuech, and A. Bramati. "Observation of the optical spin Hall effect". In: *Nature Physics* 3.9 (2007), pp. 628–631. DOI: 10.1038/nphys676.

[Lin13] J. Lin, J. P. B. Mueller, Q. Wang, G. Yuan, N. Antoniou, X.-C. Yuan, and F. Capasso. "Polarization-controlled tunable directional coupling of surface plasmon polaritons". In: *Science (New York, N.Y.)* 340.6130 (2013), pp. 331–334. DOI: 10.1126/science.1233746.

[Lip69] S. G. Lipson and H. S. Lipson. *Optical physics*. Cambridge: Univ. Press, 1969. ISBN: 0-521-06926-2.

[Lod17] P. Lodahl, S. Mahmoodian, S. Stobbe, A. Rauschenbeutel, P. Schneeweiss, J. Volz, H. Pichler, and P. Zoller. "Chiral quantum optics". In: *Nature* 541.7638 (2017), pp. 473–480. DOI: 10.1038/nature21037.

[Lux13] I. J. Luxmoore, N. A. Wasley, A. J. Ramsay, A. C. T. Thijssen, R. Oulton, M. Hugues, S. Kasture, V. G. Achanta, A. M. Fox, and M. S. Skolnick. "Interfacing spins in an InGaAs quantum dot to a semiconductor waveguide circuit using emitted photons". In: *Physical review letters* 110.3 (2013), p. 037402. DOI: 10.1103/PhysRevLett.110.037402.

[Mai07] S. A. Maier. *Plasmonics: Fundamentals and Applications*. New York, NY: Springer US, 2007. DOI: 10.1007/0-387-37825-1.

[Mar10] M. P. Marder. *Condensed Matter Physics*. 2nd ed. Hoboken: John Wiley & Sons, 2010. DOI: 10.1002/9780470949955.

[Mar15] L. Marrucci. "Spin gives direction". In: *Nature Physics* 11.1 (2015), pp. 9–10. DOI: 10.1038/nphys3198.

[May12] D. Maystre. "Theory of Wood's Anomalies". In: *Plasmonics*. Ed. by S. Enoch and N. Bonod. Vol. 167. Springer Series in Optical Sciences. Berlin, Heidelberg: Springer Berlin Heidelberg, 2012, pp. 39–83. DOI: 10.1007/978-3-642-28079-5_2.

[Nov12] L. Novotny and B. Hecht. *Principles of nano-optics*. Second edition. Cambridge: Cambridge University Press, 2012. ISBN: 978-1-107-00546-4.

[OCo14] D. O'Connor, P. Ginzburg, F. J. Rodríguez-Fortuño, G. A. Wurtz, and A. V. Zayats. "Spin-orbit coupling in surface plasmon scattering by nanostructures". In: *Nature communications* 5 (2014), p. 5327. DOI: 10.1038/ncomms6327.

[Ott68] A. Otto. "Excitation of nonradiative surface plasma waves in silver by the method of frustrated total reflection". In: *Zeitschrift für Physik A Hadrons and nuclei* 216.4 (1968), pp. 398–410. DOI: 10.1007/BF01391532.

[Ozb06] E. Ozbay. "Plasmonics: merging photonics and electronics at nanoscale dimensions". In: *Science (New York, N.Y.)* 311.5758 (2006), pp. 189–193. DOI: 10.1126/science.1114849.

[Pet14] J. Petersen, J. Volz, and A. Rauschenbeutel. "Nanophotonics. Chiral nanophotonic waveguide interface based on spin-orbit interaction of light". In: *Science (New York, N.Y.)* 346.6205 (2014), pp. 67–71. DOI: 10.1126/science.1257671.

[Poh13] M. Pohl, L. E. Kreilkamp, V. I. Belotelov, I. A. Akimov, A. N. Kalish, N. E. Khokhlov, V. J. Yallapragada, A. V. Gopal, M. Nur-E-Alam, M. Vasiliev, D. R. Yakovlev, K. Alameh, A. K. Zvezdin, and M. Bayer. "Tuning of the transverse magneto-optical Kerr effect in magneto-plasmonic crystals". In: *New Journal of Physics* 15.7 (2013), p. 075024. DOI: 10.1088/1367-2630/15/7/075024.

[Pop09] M. N. Popova. "Spectroscopy of compounds from the family of rare-earth orthoborates". In: *Journal of Rare Earths* 27.4 (2009), pp. 607–611. DOI: 10.1016/S1002-0721(08)60298-7.

[Ray07] Rayleigh. "III. Note on the remarkable case of diffraction spectra described by Prof. Wood". In: *The London, Edinburgh, and Dublin Philosophical Magazine and Journal of Science* 14.79 (1907), pp. 60–65. DOI: 10.1080/14786440709463661.

[Rik97] G. L. J. A. Rikken and E. Raupach. "Observation of magneto-chiral dichroism". In: *Nature* 390.6659 (1997), pp. 493–494. DOI: 10.1038/37323.

[Rod13] F. J. Rodríguez-Fortuño, G. Marino, P. Ginzburg, D. O'Connor, A. Martínez, G. A. Wurtz, and A. V. Zayats. "Near-field interference for the unidirectional excitation of electromagnetic guided modes". In: *Science (New York, N.Y.)* 340.6130 (2013), pp. 328–330. DOI: 10.1126/science.1233739.

[Rod14] F. J. Rodríguez-Fortuño, I. Barber-Sanz, D. Puerto, A. Griol, and A. Martínez. "Resolving Light Handedness with an on-Chip Silicon Microdisk". In: *ACS Photonics* 1.9 (2014), pp. 762–767. DOI: 10.1021/ph500084b.

[Rod15] F. J. Rodríguez-Fortuño, N. Engheta, A. Martínez, and A. V. Zayats. "Lateral forces on circularly polarizable particles near a surface". In: *Nature communications* 6 (2015), p. 8799. DOI: 10.1038/ncomms9799.

[Sah12] K. Saha, S. S. Agasti, C. Kim, X. Li, and V. M. Rotello. "Gold nanoparticles in chemical and biological sensing". In: *Chemical reviews* 112.5 (2012), pp. 2739–2779. DOI: 10.1021/cr2001178.

[Sch10] J. A. Schuller, E. S. Barnard, W. Cai, Y. C. Jun, J. S. White, and M. L. Brongersma. "Plasmonics for extreme light concentration and manipulation". In: *Nature materials* 9.3 (2010), pp. 193–204. DOI: 10.1038/nmat2630.

[Sch14] S. Schlücker. "Surface-enhanced Raman spectroscopy: concepts and chemical applications". In: *Angewandte Chemie (International ed. in English)* 53.19 (2014), pp. 4756–4795. DOI: 10.1002/anie.201205748.

[Scu97] M. O. Scully and M. S. Zubairy. *Quantum optics*. Cambridge: Cambridge University Press, 1997. DOI: 10.1017/CBO9780511813993.

[Sey18] K. L. Seyler, D. Zhong, D. R. Klein, S. Gao, X. Zhang, B. Huang, E. Navarro-Moratalla, L. Yang, D. H. Cobden, M. A. McGuire, W. Yao, Di Xiao, P. Jarillo-Herrero, and X. Xu. "Ligand-field helical luminescence in a 2D ferromagnetic insulator". In: *Nature Physics* 14.3 (2018), p. 277. DOI: 10.1038/s41567-017-0006-7.

[Sho14] I. Shomroni, S. Rosenblum, Y. Lovsky, O. Bechler, G. Guendelman, and B. Dayan. "Quantum optics. All-optical routing of single photons by a one-atom switch controlled by a single photon". In: *Science (New York, N.Y.)* 345.6199 (2014), pp. 903–906. DOI: 10.1126/science.1254699.

[Sin17] I. S. Sinev, A. A. Bogdanov, F. E. Komissarenko, K. S. Frizyuk, M. I. Petrov, I. S. Mukhin, S. V. Makarov, A. K. Samusev, A. V. Lavrinenko, and I. V. Iorsh. "Chirality Driven by Magnetic Dipole Response for Demultiplexing of Surface Waves". In: *Laser & Photonics Reviews* 11.5 (2017), p. 1700168. DOI: 10.1002/lpor.201700168.

[Söl15] I. Söllner, S. Mahmoodian, S. L. Hansen, L. Midolo, A. Javadi, G. Kiršanskė, T. Pregnolato, H. El-Ella, E. H. Lee, J. D. Song, S. Stobbe, and P. Lodahl. "Deterministic photon-emitter coupling in chiral photonic circuits". In: *Nature nanotechnology* 10.9 (2015), pp. 775–778. DOI: 10.1038/nnano.2015.159.

[Sol17] I. V. Soldatov and R. Schäfer. "Selective sensitivity in Kerr microscopy". In: *The Review of scientific instruments* 88.7 (2017), p. 073701. DOI: 10.1063/1.4991820.

[Spi16] F. Spitzer, B. A. Glavin, V. I. Belotelov, J. Vondran, I. A. Akimov, S. Kasture, V. G. Achanta, D. R. Yakovlev, and M. Bayer. "Enhancement of electron hot spot relaxation in photoexcited plasmonic structures by thermal diffusion". In: *Physical Review B* 94.20 (2016), p. 201118. DOI: 10.1103/PhysRevB.94.201118.

[Spi18] F. Spitzer, A. N. Poddubny, I. A. Akimov, V. F. Sapega, L. Klompmaker, L. E. Kreilkamp, L. V. Litvin, R. Jede, G. Karczewski, M. Wiater, T. Wojtowicz, D. R. Yakovlev, and M. Bayer. "Routing the emission of a near-surface light source by a magnetic field". In: *Nature Physics* 14.10 (2018), pp. 1043–1048. DOI: 10.1038/s41567-018-0232-7.

[Str36] J. Strong. "Effect of Evaporated Films on Energy Distribution in Grating Spectra". In: *Physical Review* 49.4 (1936), pp. 291–296. DOI: 10.1103/PhysRev.49.291.

[Sun94] C.-K. Sun, F. Vallée, L. H. Acioli, E. P. Ippen, and J. G. Fujimoto. "Femtosecond-tunable measurement of electron thermalization in gold". In: *Physical Review B* 50.20 (1994), pp. 15337–15348. DOI: 10.1103/PhysRevB.50.15337.

[Syl16] D. Sylgacheva, N. Khokhlov, A. Kalish, S. Dagesyan, A. Prokopov, A. Shaposhnikov, V. Berzhansky, M. Nur-E-Alam, M. Vasiliev, K. Alameh, and V. Belotelov. "Transverse magnetic field impact on waveguide modes

of photonic crystals". In: *Optics letters* 41.16 (2016), pp. 3813–3816. DOI: 10.1364/OL.41.003813.

[Tem10] V. V. Temnov, G. Armelles, U. Woggon, D. Guzatov, A. Cebollada, A. Garcia-Martin, J.-M. Garcia-Martin, T. Thomay, A. Leitenstorfer, and R. Bratschitsch. "Active magneto-plasmonics in hybrid metal–ferromagnet structures". In: *Nature Photonics* 4.2 (2010), pp. 107–111. DOI: 10.1038/nphoton.2009.265.

[Tom95] M. S. Tomaš. "Green function for multilayers: Light scattering in planar cavities". In: *Physical Review A* 51.3 (1995), pp. 2545–2559. DOI: 10.1103/PhysRevA.51.2545.

[Vin03] N. Q. Vinh, H. Przybylińska, Z. F. Krasil'nik, and T. Gregorkiewicz. "Microscopic structure of Er-related optically active centers in crystalline silicon". In: *Physical review letters* 90.6 (2003), p. 066401. DOI: 10.1103/PhysRevLett.90.066401.

[Vin10] A. P. Vinogradov, A. V. Dorofeenko, A. M. Merzlikin, and A. A. Lisyansky. "Surface states in photonic crystals". In: *Physics-Uspekhi* 53.3 (2010), pp. 243–256. DOI: 10.3367/UFNe.0180.201003b.0249.

[Wag00] F. E. Wagner, S. Haslbeck, L. Stievano, S. Calogero, Q. A. Pankhurst, and K. P. Martinek. "Before striking gold in gold-ruby glass". In: *Nature* 407.6805 (2000), pp. 691–692. DOI: 10.1038/35037661.

[Web10] J. R. Weber, W. F. Koehl, J. B. Varley, A. Janotti, B. B. Buckley, C. G. van de Walle, and D. D. Awschalom. "Quantum computing with defects". In: *Proceedings of the National Academy of Sciences of the United States of America* 107.19 (2010), pp. 8513–8518. DOI: 10.1073/pnas.1003052107.

[Whi99] D. M. Whittaker and I. S. Culshaw. "Scattering-matrix treatment of patterned multilayer photonic structures". In: *Physical Review B* 60.4 (1999), p. 2610. DOI: 10.1103/PhysRevB.60.2610.

[Woo02] R. W. Wood. "On a Remarkable Case of Uneven Distribution of Light in a Diffraction Grating Spectrum". In: *Proceedings of the Physical Society of London* 18.1 (1902), pp. 269–275. DOI: 10.1088/1478-7814/18/1/325.

[Yag16] S. Yagupov, M. Strugatsky, K. Seleznyova, Y. Mogilenec, E. Milyukova, E. Maksimova, I. Nauhatsky, A. Drovosekov, N. Kreines, and J. Kliava. "Iron borate films: Synthesis and characterization". In: *Journal of Magnetism and Magnetic Materials* 417 (2016), pp. 338–343. DOI: 10.1016/j.jmmm.2016.05.098.

[Zee96] P. Zeeman. "Measurements concerning the influence of a magnetization, perpendicular to the plane of incidence on the light reflected from an iron mirror." In: *Leiden Commun.* 29.3 (1896), pp. 3–13.

[Zve97] A. K. Zvezdin and V. A. Kotov. *Modern magnetooptics and magnetooptical materials*. Studies in condensed matter physics. Bristol: Inst. of Physics Publ, 1997. ISBN: 0-7503-0362-X.